Phase-contrast x-ray tomography for soft and hard condensed matter

PROEFSCHRIFT

ter verkrijging van de graad van doctor

aan de Technische Universiteit Delft,

op gezag van de Rector Magnificus prof. ir. K.Ch.A.M. Luyben,

voorzitter van het College voor Promoties,

in het openbaar te verdedigen op 17 september 2013, 15:00 uur

door

Alexander Kostenko

MSc in de natuurkunde

geboren te Moscouw

Dit proefschrift is goedgekeurd door de promotor:
Prof.dr.ir. L. J. van Vliet

Samenstelling promotiecommissie:

Rector Magnificus,	voorzitter
Prof.dr.ir. L.J. van Vliet,	Technische Universiteit Delft (promotor)
Dr.ir. S.E. Offerman,	Technische Universiteit Delft (co-promotor)
Prof.dr.ir. K.J. Batenburg,	Centrum Wiskunde en Informatica
Prof.dr.ir. J. Sietsma	Technische Universiteit Delft
Prof.dr.ir. P.M. van den Berg	Technische Universiteit Delft
Dr. W. Ludwig	Institut national des sciences appliquées de Lyon
Prof.dr. H.F. Poulsen	Technische Universiteit van Denmark

Alike for those who for To-day prepare,
And those that after some To-morrow stare,
A Muezzin from the Tower of Darkness cries
"Fools! your Reward is neither Here nor There."
© Omar Khayyam

Contents

Contents

1 Introduction

The idea of Phase-Contrast Imaging (PCI) appeared first in light microscopy in the 1930s. Frits Zernike received the Nobel prize in physics for his invention of the phase contrast microscope in 1953. The method was designed to greatly amplify the contrast of a conventional microscope to visualize otherwise undetectable structures within living cells. Later on, with the development of electron microscopy and advanced x-ray sources, the same principle was introduced into the field of transmission electron microscopy (TEM-PCI) [1] and x-ray imaging (x-ray PCI) [2]. From that point on, x-ray PCI has found an ever increasing number of applications: it was used to study various carbon-based composites [3, 4], evolution of microstructures in metals and semiconductors [5, 6], small animal imaging [7, 8, 10], soft tissue imaging [11, 12, 13, 14, 15] and studies dedicated to bio-materials [16, 17].

In this chapter you will find a brief introduction to some of the major challenges that are encountered in the field of x-ray PCI. This overview will include the description of the typical problems which rise in both the experimental area and the development of the image reconstruction algorithms. Finding a solution to some of these problems together with the exploration for new applications of x-ray PCI represents the main motivation of this project.

1.1 Basic principles of x-ray Phase-Contrast Imaging

Before the basic mechanism of x-ray PCI can be described, we need to introduce some fundamental principles of the photon-matter interaction. When x-rays with energies in the range 10 – 100 keV propagate through matter, several types of interactions (mainly photoelectric effect and Compton scattering) contribute to the attenuation of the intensity of electromagnetic field [18]. In addition to it, depending on the phase velocity of x-rays in the given material, the phase of the electromagnetic wave

will change as it propagates through the specimen. Both effects are described using the complex refractive index of the material:

$$n = 1 - \delta + i\beta, \tag{1.1}$$

where δ, decrement of the refractive index, is related to the change in the phase of the electromagnetic field and β, the attenuation index, describes the attenuation of the field. The scalar wave function that describes the electromagnetic field after interaction with the specimen has the following form [19]:

$$\psi = E_0 \cdot exp(\frac{i2\pi nd}{\lambda}) = E_0 \cdot exp(\frac{i2\pi(1-\delta)d}{\lambda}) \cdot exp(-\frac{2\pi\beta d}{\lambda}), \tag{1.2}$$

here E_0 stands for the amplitude of the incoming field, d denotes the thickness of the specimen with a complex refractive index n and λ denotes the wavelength of the electromagnetic field. The specimen thickness d is assumed to be small enough to neglect the diffraction of the field inside the object. It is easy to see that according to this formula β defines the exponential decay of the amplitude of the field and δ the phase shift. When the x-ray energy is greater than the K-shell binding energy of the element, the refractive index depends of the atomic number Z and the energy E in the following way:

$$\delta \propto \frac{\rho_a Z}{E^2},$$
$$\beta \propto \frac{\rho_a Z^4}{E^4}, \tag{1.3}$$

where ρ_a is the *atomic number density* of a material (i.e. number of atoms per unit volume)[20, 21]. For high energy x-rays (i.e. 10-100 keV), the ratio δ/β is in the range of $10^2 - 10^3$ for the majority of chemical elements. Thus, phase changes introduced by small variations in the specimen's density or composition will usually be much higher than changes in attenuation. Since the decrement of the complex refractive index is inversely proportional to the second power of the x-ray energy whereas the attenuation coefficient to the fourth power, the phase-attenuation ratio δ/β is generally higher at higher energies. To describe the refractive properties of a three-dimensional object, it is useful to introduce the projected attenuation image

$\mu(x, y)$ and the projected phase shift $\phi(x, y)$:

$$\mu(x, y) = \frac{2\pi}{\lambda} \cdot \int \beta(x, y, z) dz$$
$$\phi(x, y) = -\frac{2\pi}{\lambda} \cdot \int \delta(x, y, z) dz. \qquad (1.4)$$

Here $\{x, y\}$ are the coordinates in the image plane and z denotes the coordinate in the direction of propagating x-ray beam. The intensity of the electromagnetic field after interaction with the specimen is described by the well-known Beer-Lambert law:

$$I(x, y) = |\psi(x, y)|^2 = I_0 \cdot e^{-2\mu(x,y)}, \qquad (1.5)$$

where I_0 is the intensity of the initial uniform illumination. It is obvious that only the attenuation image of the specimen and not the phase image can be determined by measuring the intensity of the exit wave, i.e. the field directly after the object. In fact, determination of the projected phase of the specimen $\phi(x, y)$ is not trivial due to the extremely high frequencies of electromagnetic waves in the x-ray region and the small refraction angles that are associated with phase shifts typical for x-ray radiation. In order to determine the projected phase, various interference effects are used in several different methods that are collectively referred to as x-ray PCI. These acquisition techniques can be categorized into the following types: crystal interferometry [2, 22], diffraction enhanced imaging (DEI) [23], gratings-based PCI [24], aperture-based PCI [25] and propagation-based PCI [26] (see Figure 1.1).

1.2 X-ray Phase-Contrast Imaging techniques

Crystal interferometry Crystal interferometry is the oldest of all techniques developed for x-ray PCI [2]. In this approach, a splitter crystal splits an incoming parallel x-ray beam into a reference beam and a beam that illuminates the specimen. The two beams are subsequently merged using two additional crystals as depicted in Figure 1.1(a). The resulting image is formed due to interference between the reference beam and the diffracted beam and depends on the optical path difference between two beams [22]. This method allows to measure the phase image of the object directly, which makes it the most sensitive method of all PCI techniques.
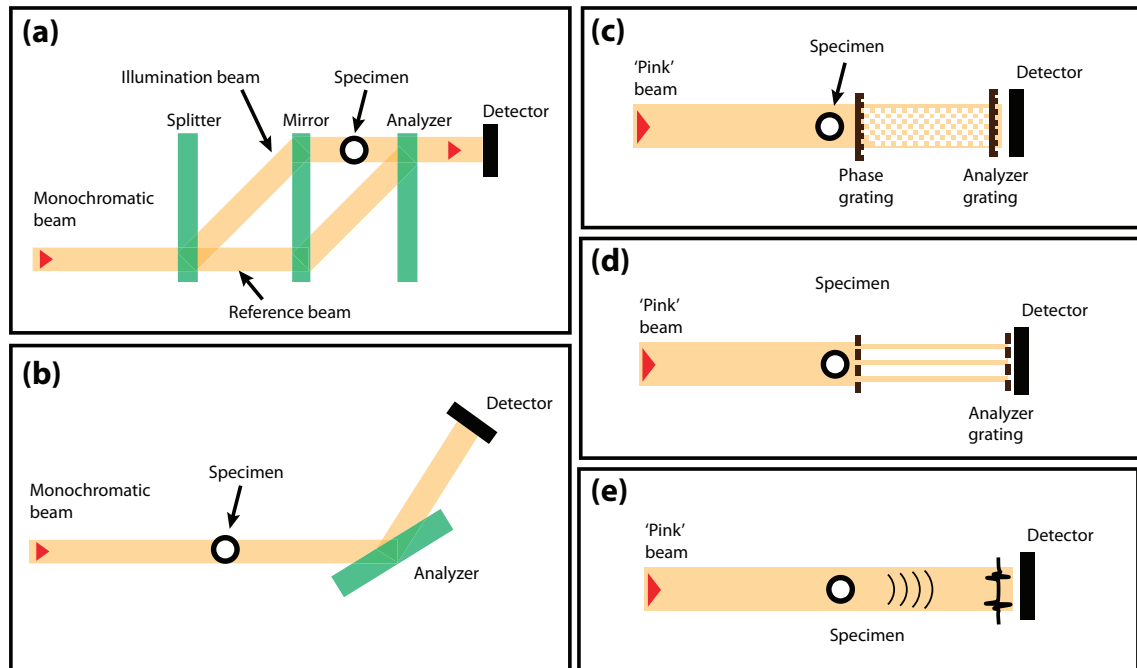
Figure 1.1: Schematic representation of different x-ray PCI acquisition techniques. (a) – crystal interferometry, (b) – diffraction enhanced PCI, (c) – Talbot interferometry, (d) – coded-apertures based PCI, (e) – propagation based PCI.

However, in comparison to other techniques, this method is also associated with the largest number of technical limitations [27]. Among them is the requirement for mechanical stability of the setup on a sub-wavelength scale, which limits its maximum size and the size of the specimen to several centimeters. Another technical restriction is the very high monochromaticity of the system that greatly reduces the flux and confines this technique to extremely bright x-ray sources based on synchrotron radiation.

Diffraction Enhanced Imaging   Diffraction Enhanced Imaging (DEI) or analyzer-based PCI (ABP) is another technique that is usually confined to synchrotron facilities due to a high monochromaticity. In this method, a parallel monochromatic x-ray beam passes through the specimen and is subsequently refracted by the analyzer crystal as shown in Figure 1.1(b). A phase-contrast image can be recorded when the analyzer crystal is slightly misaligned with respect to the Bragg diffraction angle that is associated with the incoming monochromatic beam [23]. If a number of phase-contrast images are recorded at different nonalignment angles, phase retrieval algorithms can be used to retrieve images that correspond to different contrast
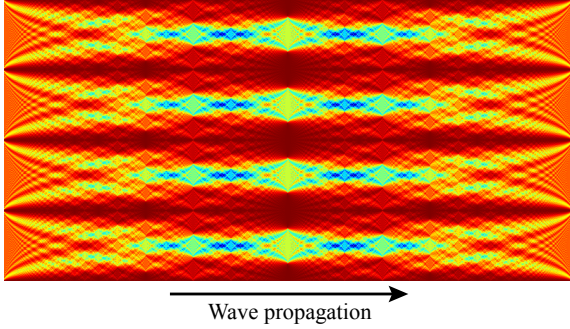
Figure 1.2: Illustration of the Talbot effect. A pure phase grating with a period of g and phase shift π (left) creates an interference pattern that results in an array of bright and dark lines at a fractional Talbot distance $g^2/8\lambda$ (right) and restores to a uniform illumination at $g^2/4\lambda$.

Wave propagation

mechanisms: attenuation, refraction and scattering [28, 29].

DEI is sensitive to the gradient of the phase image and allows to measure it only in the direction perpendicular to the rotation axis of the analyzer crystal:

$$\alpha \sim \frac{\lambda}{2\pi} \cdot \frac{\partial \phi(x)}{\partial x}, \tag{1.6}$$

here α is the measured x-rays refraction angle and the coordinate x corresponds the direction of the gradient. This technique also requires a bright monochromatic x-ray beam and is very sensitive to the alignment of the analyzer crystal.

Talbot interferometry   Talbot interferometry (or grating-based PCI) allows, similarly to DEI, to measure the refraction of x-rays proportional to the gradient in the specimen's projected phase [24, 30]. This technique makes use of the Talbot effect - a Fresnel diffraction phenomenon that produces a repetitive periodic interference pattern as the wave-front propagates through space (see Figure 1.2). The Talbot effect allows to create a periodic intensity pattern illuminating the x-ray detector. When the specimen is placed into the x-ray beam, the pattern is distorted due to refraction. Sub-pixel spatial distortions of the periodic illumination pattern introduced by the object, can be translated into intensity variations using an analyzer absorption grating with a suitable period (see Figure 1.1(c)). In this technique, the gradient of the projected phase of the specimen can be reconstructed from a number of images that are acquired after the analyzer grating is shifted relatively to the periodic illumination pattern. Similarly to DEI, images that correspond to different contrast modes can be retrieved from the experimental data [31]. The method has a major advantage of providing significant contrast enhancements in medium resolution regimes (permitting pixel sizes on the order of 100 μm) and remains efficient in a relatively wide spectral bandwidth ($\triangle E/E \sim 10\%$) [32]. The field of view

for this technique is limited by the size of the grating. These factors make Talbot interferometry very suitable for table-top implementations.

Coded-apertures based PCI   Coded-apertures based PCI is to some extend similar to grating-based PCI but does not rely on the Talbot interferometric effect. Two identical absorbing apertures have to be aligned in the x-ray beam – the first aperture is placed right before the specimen, whereas the analyzer aperture is placed on top of the detector surface (see Figure 1.1(d)). The period of the apertures should correspond to the resolution of the detector, e.g. 100 μm [25]. Like in grating-based PCI, the intensity measured by the detector changes when the wave-front of the x-ray beam is distorted due to phase shifts introduced by the specimen. A phase-contrast image can be obtained using this method, by combining several images which are recorded after shifting the analyzer aperture relative to the illumination pattern. The simplicity of this approach makes it highly suitable for a table-top implementation [33]. This technique might become preferable for applications that involve x-ray with energies close to or higher than 100 keV, where it is difficult to manufacture attenuation gratings [34].

Propagation-based PCI   Propagation-based (or in-line) x-ray PCI is often preferred to the other techniques because of its simplicity. This technique relies on a simple idea of recording an intensity image (or multiple images) of a near-field diffraction pattern that occurs due to phase changes introduced by the object (see Figure 1.1(e)). It does not require any x-ray optical components, gratings or masks. Only an x-ray source and a detector are needed. However, it poses very stringent requirements on the spatial coherence of the x-ray source and the resolution of the detector. High spatial coherence can be achieved using x-ray sources with a small focal spot size, or by allowing a large source-to-object distance, which is usually limited by the brightness of the x-ray source. According to the Transport of Intensity Equation (TIE) approach for weakly absorbing objects [35], variations of intensity image recorded in propagation-based PCI are proportional to the Laplacian of the specimen's phase image:

$$\frac{I_R(x,y)}{I_{R=0}(x,y)} - 1 = -\frac{\lambda R}{2\pi} \cdot \nabla^2 \phi(x,y), \tag{1.7}$$

here $I_R(x, y)$ is the intensity image measured at the propagation distance R, $I_{R=0}(x, y)$ is the contact intensity image measured at $R = 0$ and ∇^2 is the two-dimensional Laplacian operator. Since in propagation-based PCI, the phase-contrast effect is proportional to the second derivative of the phase image, this imaging technique is most sensitive to high spatial frequencies. To provide good sensitivity, a spatial resolution in the order of microns is typically required. That makes the propagation-based PCI an ideal technique for x-ray microscopy but a less likely candidate for soft-tissue imaging in humans.

Until recently, the use of the propagation-based PCI and most of the other techniques listed above, was limited to the synchrotron radiation facilities that are capable of providing a very bright, monochromatic and spatially coherent source of x-rays.

1.3 X-ray sources suitable for x-ray PCI

Despite the diversity of experimental approaches that can be used for x-ray PCI, up to now none of them became widely utilized in laboratories outside of the large synchrotron radiation facilities. A firm progress in that direction is made by researchers working on the prototypes of Talbot interferometers suitable for laboratory and medical use [32, 36]. Grating-based and coded-apertures based PCI are both compatible with medium resolution imaging (pixels size $\sim 100~\mu m$). So they can be implemented in a laboratory, using conventional x-ray tubes and the available x-ray detectors [37]. However, dissemination of the gratings-based PCI technique is largely inhibited by the lack of bright table-top x-ray sources. All of the x-ray PCI techniques described above rely on availability of the x-ray sources capable of producing bright quasi-monochromatic radiation with a large degree of spatial coherency. The high spatial coherency can be achieved by reducing the effective size of the x-ray source. Taking these facts into account, a PCI-compatible x-ray source must be capable of radiating a high photon flux from a small area, in a relatively narrow spectral range. The term brilliance is usually used to characterize the photon flux that is irradiated per unit area of the source in 0.1% of the spectral bandwidth ($[\mathrm{photons}/\mathrm{sec\cdot mm^2\cdot mrad^2\cdot 0.1\% BW}]$). This characteristic is essential for x-ray sources required in any of the PCI applications.

Synchrotron radiation   Since the invetion of x-ray PCI to nowadays, most of the x-ray PCI experiments were carried out using synchrotron light sources. In this type of x-ray source, the radiation is produced when high-energy electrons (typically $\gtrsim 1$ GeV) interact with rapidly changing electromagnetic field generated by superconducting magnets. Accelerating electrons to such high energies requires construction of a large synchrotron rings with a circumference of hundreds of meters. The typical brightness of a 3rd generation synchrotron reaches $10^{18} - 10^{22}$photons/sec·mm²·mrad²·0.1%BW, surpassing any other technology of x-rays generation by several orders of magnitude. Extremely high brightness and other unique properties of the synchrotron light sources make them perfectly suitable for implementation of the x-ray PCI techniques. However, for a large number of applications, x-ray PCI has to be implemented in the laboratory or the hospital enviroment. Taking that into account, advances in the field of novel x-ray sources play a key role in the development of x-ray PCI.

Alternative x-ray sources   Conventional x-ray tube technology exploits the combination of bremsstrahlung and x-ray fluorescence in converting the energy of electrons accelerated by the electromagnetic field into x-rays. The maximum heat that can be dissipated by the anode of the tube sets an upper limit to the brilliance of this type of the x-ray source to around 10^{10}photons/sec·mm²·mrad²·0.1%BW [38]. Currently, there are three major alternative tabletop technologies that can significantly outperform the rotating anode x-ray tube.

A *liquid metal jet* exploits the same basic principles as the conventional x-ray tube – bremsstrahlung radiation and x-ray fluorescence [39], but uses a thin jet of liquid metal for x-ray generation instead of a solid metal anode. This technology is reported to be capable of delivering a brilliance of up to $1.5 \cdot 10^{11}$photons/sec·mm²·mrad²·0.1%BW and has a potential to gain another order of magnitude in brightness [39].

X-ray sources based on Inverse Compton Scattering (ICS) [40] offer another possibility for enhanced brightness. In these sources, x-ray radiation is generated when electrons accelerated by a linac or a tabletop synchrotron to relativistic speeds are brought into interaction with an alternating electromagnetic field which is delivered by a high power laser. Unlike bremsstrahlung, radiation produced by ICS sources is nearly monochromatic ($\Delta E/E < 10\%$), which translates into a naturally high brilliance. An ISC source produced by Lyncean Technologies, Inc. is reported to have an average brilliance of 10^{12}photons/sec·mm²·mrad²·0.1%BW.

MIRRORCLE-6X   Another technology that might be used in the implementation of the tabletop x-ray PCI systems is also based on miniature synchrotron technology, but relies on the bremsstrahlung phenomenon to produce x-rays. The so called MIRRORCLE x-ray source [41] makes use of a 1 to 20 MeV storage ring with a metallic target positioned in the orbit of the electron beam to produce bremsstrahlung radiation. Most of the relativistic electrons that circulate in the storage ring are not stopped by the target, and the fraction of the energy dissipated in the form of heat is much lower than in an x-ray tube. According to [42], MIRRORCLE-6X should have a brilliance on the order of 10^{11}photons/sec·mm²·mrad²·0.1%BW. Chapter 2 of this thesis presents our investigation to characterize the MIRRORCLE-6X miniature synchrotron. The main goal of this study was to determine whether this x-ray source is suitable for the implementation of propagation-based PCI. During this project we measured the contrast enhancement achievable with a PCI system based on the MIRRORCLE-6X. Experimental measurements obtained for various settings of this system were compared with simulations that were performed using an extensive digital model. This comparison led us to important insights concerning the design of the MIRROCLE-6X and its potential development.

1.4 Materials science applications

Despite all recent developments of bright compact x-ray sources, a large variety of experimental investigations now and in the near feature will still require the use of large synchrotron sources. Extremely high brilliance, unachievable outside of the 3rd generation synchrotrons, is needed to reach micron and sub-micron spatial resolutions and is also required for *in-situ* investigations of fast dynamic processes. Synchrotron based x-ray PCI offers a possibility to revolutionize materials science research. The ability to study the microscopic nature of processes that take place during both the formation and the degradation of various materials is extremely important for our understanding of their macroscopic properties. As it was mentioned above, a number of studies was carried out using x-ray PCI in order to investigate various materials [3, 4] including a number of in-situ investigations of dynamical processes [5, 6]. However, in some domains of materials science, x-ray PCI was not yet introduced. For instance, the experimental methods that are traditionally used to study solid-state phase transformations in metals include destructive techniques such as serial sectioning [43], and techniques that are capable of surface observa-

tions such as Electron Backscatter Diffraction (EBSD) [44]. These techniques do not allow to make in-situ observations of the processes that occur in the bulk of the material. Synchrotron based x-ray diffraction techniques, such as 3D X-ray Diffraction (3DXRD) microscopy, and x-ray Diffraction-Contrast Tomography DCT [45], were successfully used to study solid-state phase transformations and the structures that result from them in metals [46]. However, these techniques typically have limited spatial and temporal resolution and can hardly deliver information on dynamic processes that happen on micron or sub-micron scale. Experimental observation of such dynamic processes play a crucial role in our understanding of the macroscopic properties of materials.

Cementite morphology   Chapter 3 is dedicated to the description of an experiment carried out at the European Synchrotron Radiation Facility (ESRF), in which propagation-based PCI is combined with x-ray DCT in order to investigate the morphology of cementite grains in steel. Cementite is a iron carbide (Fe_3C) that can form in the bulk of carbon steel during various heat treatments that are applied to it during production. Depending on the composition of steel and the type of the heat treatment, cementite forms micron- and sub-micron scale structures with various morphologies ranging from carbides ($\ll 1\mu m$ in size) to pearlite lamellae and large spherodized cementite particles ($\gg 1\mu m$ in size). Formation of either of these forms of cementite defines, to a large extend, the mechanical properties of the material at the macroscopic scale and plays an important role in various industrial processes.

The main goal of this investigation is to develop a non-destructive imaging technique with sufficient spatial resolution and contrast to detect micron-sized cementite structures within the bulk of the material. Cementite forms in the bulk of ferrite and is less dense than the surrounding material by approximately 2-3%. This difference is sufficient to detect a cementite structure several microns in size using propagation-based PCI. Complimentary information about the crystallographic orientations of the ferrite grains that surround cementite can be obtained using DCT or 3DXRD techniques. The combinations of the techniques can be used in the future to carry out an in-situ investigation of the formation of cementite and evolution of its morphology in relation to the crystallographic orientation relations between the cementite grain and the surrounding ferrite grains during a particular heat treatment. The resulting experimental data can be subsequently used to refine theoretical models that are employed to design the production processes for novel types of steel.

Austenite growth The continuation of the work that is described in Chapter 3, is presented in the last chapter of this Thesis. In Chapter 6 we will present further developments of an experimental imaging approach suitable for in-situ, time-resolved observations of microscopic processes that take place during the solid-state phase transformations in steels. As it was mentioned above, the experimental techniques that were used for in-situ investigations so far, provided only limited information on the processes that occur during the phase transformations at the microscopic scale. During solid-state phase transformations, grains of the product phase (the new phase) nucleate within the parent phase. After nucleation, which typically takes place at the nanometer scale, the product grains start to grow, gradually replacing the parent phase. Evolution of the three-dimensional morphology of individual product grains was traditionally studied using computational models, but was never directly observed in experiment. Chapter 6 reports on the experimental approach in which propagation-based PCI was used to obtain a three-dimensional, time-resolved reconstruction of the product grain growth during the ferrite-to-austenite phase transformation in steel. In order to perform the experiment we developed a miniature furnace that allowed us to carry out a full 360° tomographic acquisition while the temperature of the specimen was changed in the range from 800°C to 900°C. By performing continuous tomographic scanning while the temperature of the specimen was increased at a very slow rate, we could obtain a three-dimensional time-resolved reconstruction of the growing grains of the product phase during the phase transformation. This work leads to important insights into the kinetics of the ferrite-to-austenite phase transformation and the methodology that can be used to study phase transformations *in-situ.*

1.5 Development of phase retrieval algorithms

The experimental work that was carried out at ESRF, inspired us to investigate the possibility of improvement of the image reconstruction techniques that are used in propagation-based PCI. Two aims we pursued at this stage of the research project: improving the accuracy of the existing reconstruction methods and reducing the amount of data needed for the accurate reconstruction. Accomplishing the first objective allows to improve the spatial resolution of the reconstructed data while achieving the second objective has a potential to increase the temporal resolution of time-resolved experiments similar to the one described in Chapter 6 of this thesis.

The following section gives an outlook on typical challenges that are encountered in two interrelated fields: the field of phase retrieval methods applied to PCI data that are used to recover the projected phase image of the object from the observed phase-contrast images and the field of tomographic reconstructions based on phase-contrast tomography data.
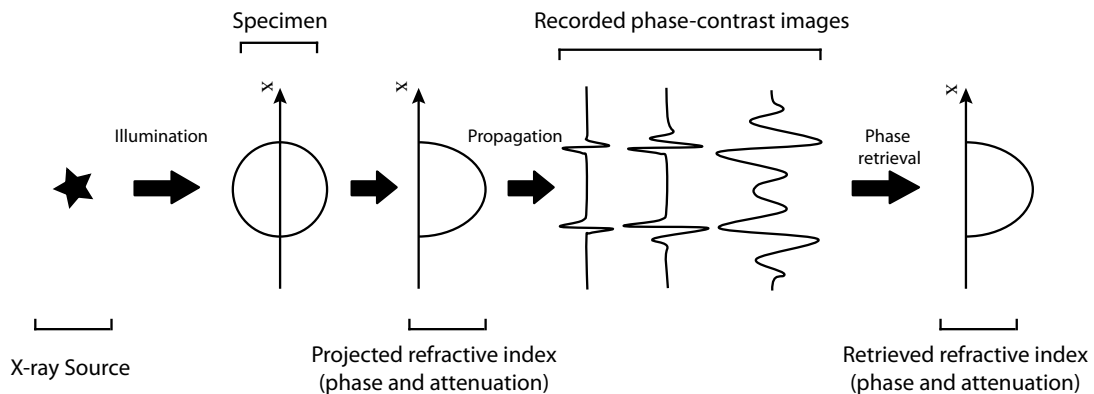
Figure 1.3: Acquisition geometry for propagation-base Phase-Contrast Imaging. Multiple phase-contrast images must be acquired in the classical approach to retrieve a high resolution phase image.

Direct phase retrieval techniques   As it was mentioned in the beginning of this chapter, propagation-based PCI does not yield a direct measurement of the specimen's phase or attenuation image. Instead, a near field diffraction pattern, that results from the combination of the attenuation and phase-contrast effects, is recorded by the detector at a suitable distance from the specimen. The recorded diffraction pattern depends on the wavelength of the x-ray radiation and the propagation distance (i.e. distance between the specimen and the detector). By acquiring multiple phase-contrast images at different propagation distances, it is possible to compute the projected attenuation and phase images of the specimen (see Figure 1.3). Different approaches that are used in x-ray PCI for image reconstruction, are usually called phase retrieval methods, as they allow to recover the projected phase image of the specimen. The conventional direct phase retrieval methods used in propagation-based PCI can be classified into three main groups: the Contrast Transfer Function (CTF) models [47], the Transport of Intensity Equation (TIE) models [48] and the Mixed TIE-CTF models [49, 50]. Each of these models is based on a particular linearization of the Fresnel diffraction integral that uses certain assumptions about the nature of the reconstructed image. For that reason, in order to improve the accuracy

Number of recorded images:	TIE	CTF	MIXED	Duality TIE	Duality CTF	Duality MIXED
1	-	artifacts in low and high frequency bands	-	blur	artifacts in high frequency bands only	artifacts in high frequency bands only
2	artifacts in low frequency band +blur	artifacts in low and high frequency bands	artifacts in low and high frequency bands	-	almost no artifacts	almost no artifacts
> 2	-	artifacts in low frequency band	artifacts in low frequency band	-	almost no artifacts	almost no artifacts

Table 1.1: Typical artifacts produced by the direct phase retrieval methods depending on the number of phase-contrast images recorded for different propagation distances. It is assumed that the experimental conditions comply with the assumptions underlying the particular model.

of phase retrieval in each x-ray PCI experiment, the most appropriate model should be chosen depending on the conditions of the experiment and the properties of the investigated object. For instance, different CTF approaches can recover a phase image with high spatial frequencies but fail when the object yields significant attenuation. A TIE model allows to calculate a more accurate phase image for strongly attenuating objects but limits the resolution of the reconstructed image to spatial frequencies $\omega < 1/\sqrt{\pi \lambda R}$, where R is the propagation distance. Both CTF and TIE models have versions that are designed for objects with negligible attenuation [51]. The so-called Mixed approaches remain valid for objects with strong attenuation and are not limited to low spatial frequencies as TIE models are. However, they fail when the reconstructed phase image contains steep gradients such as the ones caused by air-metal interfaces. Phase retrieval based on the phase-attenuation duality principle was introduced for the TIE model by Paganin [52]. In this approach the phase is assumed to be proportional to the attenuation with $\delta/\beta \approx$ const. This approach allows to compute a phase retrieved image from a single recorded phase-contrast image but can only be applied to homogeneous objects or to objects that

are composed from light elements in a limited range of x-ray energies. The phase-attenuation duality variations of the CTF and Mixed models [53, 54] were developed shortly after.

Phase retrieval based on any of the models listed above constitutes a linear inverse problem. Two unknown images, the projected attenuation and phase, can be calculated from a set of observed images - phase contrast images recorded at different propagation distances. Depending on the number of observations and the particular type of the phase retrieval model, the inverse problem associated with it will, in general, be ill-posed. This typically means that particular spatial frequencies of the reconstructed image will either be completely undetermined by the observations or will be heavily corrupted by noise. Table 1 gives a rough indication of the types of artifacts which are usually encountered due to the ill-posedness of the different phase retrieval models. The table does not discriminate between some variations of the phase retrieval models, e.g. the CTF model for objects with negligible attenuation and the CTF model for objects with weak attenuation. It is also assumed that the models are applied to experimental data that comply with the underlying approximations.

We believe that the number of conclusions can be drawn from Table 1. Firstly, high-resolution, artifact-free phase retrieval (up to some critical frequency), typically requires several phase-contrast images acquired at suitable propagation distances. Even when several phase-contrast images can be acquired, phase retrieval will be prone to low-frequency artifacts. Using phase-attenuation duality methods, it is possible, in some cases, to compute an artifact-free, resolution-limited phase retrieval from a single phase-contrast image. However, duality-based methods are valid only for objects with constant δ/β factor and will produce artifacts when this condition does not hold.

In order to overcome these complications, various regularization approaches were proposed over the years [55, 56]. Depending on the regularization approach, a specific type of *prior* knowledge about the solution can be incorporated into the inverse problem. If the prior knowledge corresponds well with the genuine properties of the reconstructed image, a correct solution may be found for an initially ill-posed or underdetermined inverse problem. However, given various developments in the field of regularization approaches, none of them provides a universal solution to all phase retrieval problems.

14

Algebraic Phase Retrieval In an attempt to find a solution for the problem of phase retrieval based on fundamentally incomplete observations, we investigated the possibility of using algebraic reconstruction algorithms. For the last decade algebraic reconstruction became widely used in solving various underdetermined and ill-posed linear problems. Various gradient-descent based techniques are used in the field of tomographic reconstructions [57], image deblurring and denoising algorithms [58, 59]. Chapter 4 presents the progress that was made concerning the development of the *algebraic algorithms* suitable for phase retrieval (i.e. algorithms based on iterative minimization of some objective function). In this chapter we propose a novel approach to phase retrieval based on Total Variation (TV) minimization. This minimization approach is based on an assumption that the reconstructed image has a sparse gradient magnitude (i.e. the image is piece-wise constant). It was shown to be capable of finding an accurate solution for severely underdetermined inverse problems for which the sparsity assumption is valid. In our investigation we have shown that most of the direct phase retrieval models can be incorporated in a TV minimization algorithm. The resulting algebraic phase retrieval techniques are tested using the simulated phase-contrast images and the experimentally acquired ones.

As it was mentioned before, the field of phase retrieval methods is closely related to the field of tomographic reconstructions. In most experiments, the phase-contrast images are not acquired to retrieve a single phase image of the specimen, as it is done in attenuation-contrast x-ray radiography. Instead, phase-contrast images are recorded in a large number of directions in order to permit a three-dimensional tomographic reconstruction of the specimen. This approach is called x-ray Phase-Contrast Tomography (PCT). The number of directions in which the phase-contrast images must be recorded in PCT is usually determined by the required spatial resolution and is typically in the range from several hundreds to a few thousands. Taking into account that some of the phase retrieval methods require several phase-contrast images to be recorded at different distances from the specimen in order to reconstruct its projected phase image, an extremely large number of images may be required for a complete x-ray PCT acquisition. This problem is partially solved, when the specimen is assumed to be relatively homogeneous, so only one phase-contrast image has to be acquired for each tomographic direction. However, the problem of reducing the number of images that is sufficient for tomographic reconstruction of the specimen plays a crucial role in many experiments.

Algebraic Phase Contrast Tomography   Another problem that is often encountered in the field of PCT is related to the intrinsic ill-posedness of most of the phase retrieval methods. As it was mentioned before, most of the phase retrieval methods do not allow to reconstruct an accurate solution for the projected phase image of the specimen (see Table 1.1). The artifacts that are produced during the phase retrieval are propagated into the tomographic reconstruction and can significantly reduce the quality of the resulting image. In Chapter 5 we present novel reconstruction algorithms that solve the combined problem of phase retrieval and tomographic reconstruction. The idea underlying this method is based on the assumption that the tomographic projections of the object are in general not independent from one another. In order to produce a consistent tomographic reconstruction of an object that falls completely within the field of view, individual projections of this object must be interrelated [60]. The resulting redundancy of tomographic data should allow to correct to certain extent for the errors that are made during the phase retrieval step. So called *algebraic reconstruction algorithms* allow to take such redundancy into account and are known in conventional tomography for a long time [61, 62, 63, 64]. However, until recent time, *algebraic reconstruction* was not used for tomographic reconstruction based on phase-contrast data. The reconstruction algorithm presented in Chapter 5 is based on TV minimization. This allows not only to find a solution to a well defined tomographic problem but, under certain conditions, allows to find an accurate reconstruction of the specimen based on significantly incomplete data [65]. This can be achieved for specimens that have a piece-wise constant composition. In other words, the tomographic data of the specimen in which the density and composition remains constant within significantly large regions with well defined boundaries, may yield a very high degree of redundancy. An accurate reconstruction of the image of such specimen can be often obtained from only few tomographic projections. This property of tomographic reconstruction algorithms can be successfully exploited in x-ray PCT. Chapter 5 compares the results obtained with the simulated and experimental x-ray PCT data using conventional tomographic reconstruction and the algebraic algorithms based on TV minimization. The algebraic approach shown in that chapter is also used in Chapter 6 to reconstruct the morphology of the austenite during the solid-state phase transformation in steel.

2 Miniature synchrotron MIRRORCLE-6X

Abstract[1]

Purpose: The implementation of in-line x-ray phase contrast imaging (PCI) for soft-tissue patient imaging is hampered by the lack of a bright and spatially coherent x-ray source that fits into the hospital environment. This article provides a quantitative characterization of the phase-contrast enhancement of a PCI system based on the miniature synchrotron technology MIRRORCLE-6X. Methods: The phase-contrast effect was measured using an edge response of a plexiglass plate as a function of the incident angle of radiation. We have developed a comprehensive x-ray propagation model based on the system's components, properties, and geometry in order to interpret the measurement data. Monte-Carlo simulations are used to estimate the system's spectral properties and resolution.

Results: The measured ratio of the detected phase-contrast to the absorption contrast is currently in the range 100% to 200%. Experiments show that with the current implementation of the MIRRORCLE-6X, a target smaller than 30–40 lm does not lead to a larger phase-contrast. The reason for this is that the fraction of x-rays produced by the material (carbon filament and glue) that is used for mounting the target in the electron beam is more than 25% of the total amount of x-rays produced. This increases the apparent source size. The measured phase-contrast is at maximum two times larger than the absorption contrast with the current set-up.

Conclusions: Calculations based on our model of the present imaging system predict that the phase-contrast can be up to an order of magnitude larger than the

---

absorption contrast in case the materials used for mounting the target in the electron beam do not (or hardly) produce x-rays. The methods described in this paper provide vital feedback for guiding future modifications to the design of the x-ray target of MIRRORCLE-type system and configuration of the in-line PCI systems in general.

2.1 Introduction

Phase Contrast Imaging (PCI) has first been introduced in optical microscopy [67] and later in transmission electron microscopy (TEM-PCI) [1] and X-ray imaging (X-PCI) [26, 68]. Medical application of X-PCI could provide a number of possibilities for label-free soft-tissue imaging, e.g. for contrast-agent-free angiography (cardiovascular), mammography (oncology) [69, 70], white matter lesions detection (neuroimaging), cartilage analysis (orthopedics) etc [71, 72, 73]. There are a number of different methods to measure X-PCI [74, 23, 22, 30]. *In-line* X-PCI is the most simple and straightforward method, as it requires only small modifications to the standard (transmission) imaging geometry. It does however, require a coherent X-ray field of sufficient brilliance for which a (bench-top) synchrotron is needed. Competing methods are *crystal-based* X-PCI [68], which is usually limited to the use of synchrotron radiation, *gratings-based* X-PCI [32] and *aperture-based* X-PCI [25], which can operate with conventional X-ray sources, but require modifications to the imaging geometry.

The requirements with respect to the size and brilliance of the X-ray source that are imposed by *in-line* X-PCI for medical imaging are incompatible with off-the-shelf X-ray sources. Large-scale synchrotron radiation facilities offer high brilliance but are far too large and far too expensive to comply with hospital infrastructure requirements. Microfocus X-ray tubes, on the other hand, are small, but lack sufficient brilliance. The development of bench-top sized high-brilliance X-ray sources is thus of great importance for advancing *in-line* X-PCI for medical applications. Miniature synchrotron X-ray sources [42, 40] are among the emerging technologies [75, 76] that might provide the right combination of size, brilliance and X-ray energy that is required for an effective implementation of *in-line* X-PCI.

We carried out a series of measurements using a prototype miniature synchrotron X-ray source, the MIRRORCLE-6X [77]. The maximum contrast levels achievable

with the current system in the X-PCI regime were compared to the corresponding contrast levels of the absorption image. Here we report on these measurements and on a model of the imaging system that includes the X-ray source characteristics, the imaging geometry and the detector characteristics. In particular, the design of the electron target in the present types of sources appears to be crucial in obtaining high contrast levels, and several design improvements are deduced from the analysis we present here.

2.2 Materials and methods

2.2.1 MIRRORCLE-6X

The imaging system investigated here is based on the compact synchrotron X-ray radiation source called MIRRORCLE-6X. The synchrotron ring of the MIRRORCLE-6X contains an electron beam accelerated to a total energy of $6MeV$. A small metallic target can be suspended on a beryllium or carbon filament inside the electron orbit to produce white spectrum *Bremsstrahlung* radiation ranging from 0.001 to $6MeV$ [78]. A cone beam of hard X-rays leaves the synchrotron ring through a beryllium exit-window.

For the experiments presented in this paper, the MIRRORCLE-6X was operated with an electron injection current of $75mA$ and an injection frequency of $400Hz$. Spherical targets composed of tungsten with a diameter of $10\mu m$, $20\mu m$ and $40\mu m$ were used for X-ray generation. Each target was suspended inside an epoxy droplet attached to a carbon filament of $7.6\mu m$ in diameter. Analysis of the acquired data, supported by simulations, show that a significant part of the radiation is generated by the epoxy surrounding the target and the part of the target mounting wire that is exposed to the electron beam (roughly $\sim 1mm$ in diameter). This, so-called compound source model, has a profound influence on the effective source size and its spectral characteristics, and will be investigated in the subsection 2.3.3.

The absorbed radiation dose was measured at $1m$ distance away from the source during each acquisition. Typical values for the measured dose are in the range of 2 to $3.5mGy/min$. Using the conversion factor proposed by Yamada [79] we can estimate that the brightness of the MIRRORCLE-6X was on the order $10^{10}-10^{11} photons/(s \cdot mrad^2 \cdot 0.1\%band)$. It has to be noted, however, that the conversion between the
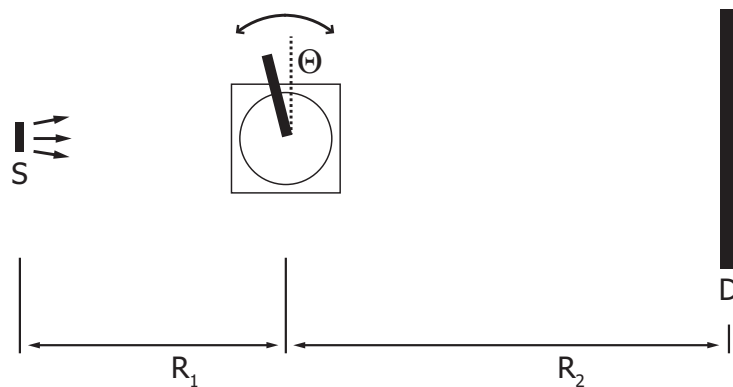
Figure 2.1: Top-view of the imaging setup. The sample is positioned between the X-ray source (S) and the detector (D) allowing for magnified imaging. Object-source distance is R_1, object-detector distance is R_2. The sample is mounted on a rotation stage in order to record phase-contrast images of the rotated edge at an angle Θ.

measured dose in mGy/min and the brightness is uncertain and relies heavily on the accuracy with which the spectral characteristics of the system are known.

2.2.2 X-ray detector

A $BaFBr : Eu^{2+}$ photo-stimulable phosphor imaging plate (IP) was used as X-ray detector in combination with a FCR XL-1 image plate reader (Fujifilm, Tokyo, Japan). It was shown [80] that the properties of the imaging plate are highly uniform over its surface and that the response is linear relative to the radiation dose up to $4 \cdot 10^4$photons/$100\mu m^2$ providing a wide dynamic range.

The Full Width at Half Maximum (FWHM) of the detector's point-spread-function (PSF) is in the range of $170 \sim 200\mu m$ [80, 81]. The quantum efficiency (QE) of the IP is given to be almost 100% for energies below 20 keV and drops to about 50% or less for energies above 35 KeV [82, 83].

As the properties of IPs may vary between the different models, the PSF and its spectral characteristics were estimated by us independently. The PSF of the IP used in our experiment was estimated from the acquired reference beam-images using the "noise method" [84, 85]. The PSF was found to be approximately Gaussian shaped with a FWHM of $260\mu m$. The images were sampled by the reader with a pixel pitch of $150\mu m$. Further discussion of the detector's spectral characteristics is given in subsection 2.3.2.
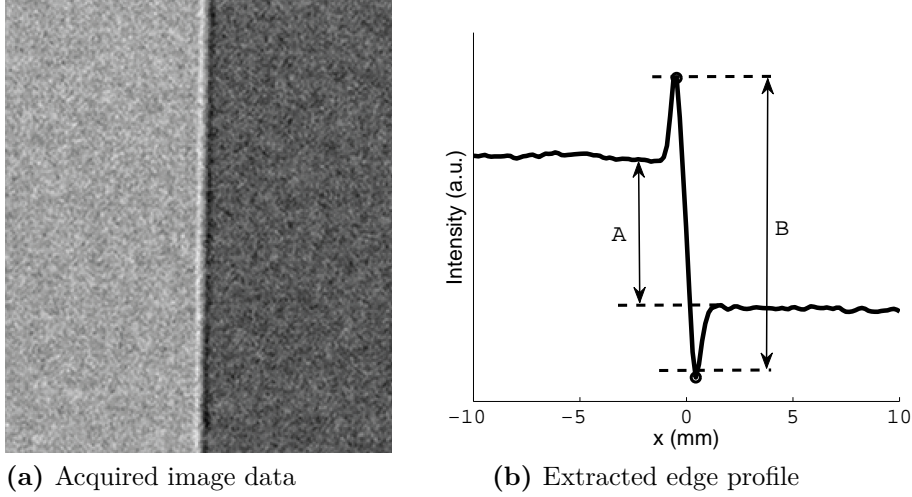
(a) Acquired image data   **(b)** Extracted edge profile

Figure 2.2: An image of a 1.95 mm plexiglass plate is acquired in the X-PCI regime (a). An intensity fringe due to phase-contrast is clearly visible on the image, slightly rotated relatively to the vertical axis. Image (b) shows a projected profile, calculated using the Radon transform of the image, accounting for a small tilt of the edge. The transmission contrast is indicated on the profile image as A, phase-contrast enhancement is measured as the fringe amplitude $(B - A)/A$.

2.2.3 Geometry of the setup

For *in-line X-PCI*, the standard transmission imaging geometry with a divergent beam is used (Figure 2.1). The specimen is mounted between the X-ray source and the detector with source-object distance R_1 and object-detector distance R_2, providing a magnification $M = (R_1 + R_2)/R_1$.

The phase-contrast image of the specimen has an interferometric nature and is observed as an intensity fringe located around the inhomogeneities in the projected refractive index of the object. Given certain propagation distances R_1 and R_2, the magnitude of the recorded phase-contrast image depends on the wavelength of the X-ray radiation and the contrast transfer function (CTF) of the imaging system. Therefore the major instrumental factors that define the contrast of the *X-PCI* system of a given total length are its spectral characteristics and the spatial resolution as dictated by the source size, the detector PSF and magnification.

The experiments were carried out in the high magnification regime with M in the range from 12 to 14.5 in order to reach the highest possible resolution in the object plane considering the limited resolution PSF_{det} of the $BaFBr : Eu^{2+}$ detector. In such a regime the effective resolution of the imaging system is primarily limited by

the source PSF_{src}.

2.2.4 Measurements

A thin plexiglass plate blocking part of the X-ray beam is often used as a standard specimen in the investigations of the performance of *X-PCI* systems [86, 87]. The observed image in this case is a transmission image of the plate combined with the intensity fringe of the phase-contrast image that stretches along the plexiglass-air transition (Figure 2.2). The image of such a specimen can be easily modeled, simplifying the analysis of the system performance.

The magnitude of the phase-contrast image fringe of the plexiglass plate is highly sensitive to the orientation of its edge with respect to the direction of the beam, as the projection of the edge feature changes. In our experiment the plexiglass plate (thickness $1.95mm$) is mounted on a rotation stage. Series of images can be easily recorded for a range of angles of incidence for every system setting (Figure 2.1).

2.2.5 Image processing and analysis

Since the plexiglass plate is homogeneous, it can be presented as a one-dimensional object simplifying the analysis. Several steps have to be taken before the raw measurements can be compared to the results of the model. First, a simple flat-field correction is carried out by dividing each acquired image by a reference beam image. Next, using the Radon transform, the image is integrated in the direction of the edge, resulting in a one-dimensional edge profile (Figure 2.2b). The orientation of the edge can be found as the angle for which the Radon transform of the image yields the highest maximum derivative.

The ratio between the phase contrast and transmission contrast of the edge (Figure 2.2b) can be estimated for each image by measuring the fraction of the amplitude of the phase fringe $B - A$ to the intensity drop due to absorption of the plexiglass plate A. The ratio $(B - A)/A$ was used as an estimate of the sensitivity of the phase imaging system and is referred to in the text as the *phase-contrast enhancement* (*PCE*).

2.2.6 Calibration of the angle of incidence

The phase and transmission image of the plexiglass plate both depend on the angle with which the radiation is incident on it. This results in a high sensitivity of the *phase-contrast enhancement* to the angle of incidence. For that reason, each experiment consists of a series of images taken for a range of object orientations of approximately ±3° around zero rotation angle (Figure 2.1). A variable angular step size in the range from 0.1° to 1° was used to provide denser sampling around 0° orientation. Considering the fact that the projected phase map of a thin plate must be symmetrical relative to the rotation angle 0°, the correction for a small misalignment in the object orientation could be done after the data acquisition.

2.3 Model

The MIRRORCLE-6X is a highly polychromatic X-ray source (spectrum $0.001 - 6 MeV$)[42] which requires an accurate account for polychromaticity during the analysis of the imaging process. The corresponding numerical model, outlined below, represents the three main stages of the image formation, namely: interaction of the polychromatic X-ray field with the object, propagation of the electromagnetic field to the X-ray detector, and the model of the detection process based on the estimated spatial resolution and the spectral characteristics of the X-ray detector and the X-ray source.

2.3.1 Object interaction and field propagation

The interaction of the X-ray field with the specimen is straightforward in the current experiment. The plexiglass plate satisfies the condition of the thin-body approximation [88], therefore the field interaction is described by the transmission function (Equation 2.1):

$$T\left(x\right) = \exp\left(-\mu\left(x\right)/2\right) \cdot \exp\left(i\phi\left(x\right)\right), \tag{2.1}$$

where $\mu\left(x\right)$ is a linear attenuation map of the specimen and $\phi\left(x\right)$ is a phase map. The linear attenuation map $\mu\left(x\right)$ is calculated using the mass attenuation coefficients from the NIST database [18] and the known projected mass of the specimen. For

the X-ray energies above the absorption edges of the material ($\gg 1keV$) the phase map can be very well approximated by [68]:

$$\phi\left(x\right) = -\lambda r_e N_e d\left(x\right),\tag{2.2}$$

where λ is the wavelength of the electromagnetic field, r_e the classical electron density, N_e is the electron density of the material, and $d\left(x\right)$ the projected thickness map.

The propagation of each monochromatic component of the electromagnetic field from the object plane to the detector plane is described by Fresnel diffraction. A computationally efficient Fourier formulation of Fresnel diffraction can be written as [89]:

$$\psi_E\left(Mx, R_2\right) = \frac{1}{M}F^{-1}\exp\left(\frac{i\lambda R_2 \left|u\right|^2}{4\pi M}\right)FT\left(x\right),\tag{2.3}$$

where F and F^{-1} represent respectively the forward and inverse Fourier transforms and u denotes the spatial frequency. In this equation the geometric magnification M of the system is accounted for. The constant phase pre-factor [90] is dropped for the sake of readability as it is irrelevant for the calculation of the intensity image.

The total intensity of the field at the detector plane $I_d\left(x\right)$ will be calculated as a superposition of all propagated monochromatic components:

$$I_d\left(x\right) = \int \left|\psi_E\left(x, R_2\right)\right|^2 S\left(E\right)\text{E},\tag{2.4}$$

$S\left(E\right)$where is the effective intensity spectrum of the imaging system.

Due to the finite size of the incoherent X-ray source, the detected image is formed as a superposition of intensity fields $I_d\left(x\right)$ produced by each point of the X-ray source independently. Considering that the source size is negligible relatively to the propagation length of the field, the result of the superposition is described as a convolution of the point-source intensity field $I_d\left(x\right)$ with a point-spread-function $\text{PSF}_{\text{src}}\left(x\right)$ representing the source size and shape [88] :

$$I\left(x\right) = \text{PSF}_{\text{src}}\left(\frac{x}{M-1}\right) * \text{PSF}_{\text{det}}\left(x\right) * I_d\left(x\right),\tag{2.5}$$

where $\text{I}\left(x\right)$ is the image recorded at the detector plane, $\text{PSF}_{\text{det}}\left(x\right)$ is a point-spread-

function of the X-ray detector. The factor $M - 1$ is introduced to account for magnification of the projected source size at the detector plane.

Expression (Equation 2.5) completes the model described above, which allows us to simulate the *in-line X-PCI* image of a known "2-D specimen". The characteristics of the imaging system are included in the model as the effective spectrum $S(E)$, the imaging geometry as expressed by R_1 and R_2, and the source and detector point-spread-functions $\text{PSF}_{\text{src}}(x)$, $\text{PSF}_{\text{det}}(x)$. Accurate estimation of these functions is absolutely crucial for the modeling process and will be described in two following subsections.

2.3.2 System spectral characteristics. Detector efficiency.

The first step in modeling the imaging process is to estimate the effective spectrum of the system. The effective spectrum $S(E)$ is a product of the emission spectrum of the MIRRORCLE-6X $S_e(E)$, the energy dependent transmission of the imaging system $T_s(E)$ and the energy absorption efficiency $EAE(E)$ of the detector:

$$S(E) = S_e(E) T_s(E) EAE(E). \tag{2.6}$$

The emission spectrum $S_e(E)$ of the MIRRORCLE-6X was calculated using Monte-Carlo simulations based on the GEANT4 toolbox [91] (Figure 2.3). The energy dependent transmission of the system $T_s(E)$ is defined as the fraction of X-rays of a certain energy emitted by the source which reach the detector plane in the absence of an object. In the calculation of the system transmission $T_s(E)$, the absorption of X-rays by the beryllium exit window of the MIRRORCLE and the air between the exit window and the detector is accounted for.

The energy absorption efficiency $EAE(E)$ of the detector is defined as a fraction of X-ray intensity of a certain energy which is converted to a detector signal. It is given by [92]:

$$EAE(E) = \left(\frac{\mu_{en}(E)}{\mu(E)}\right)\left(1 - e^{-\mu(E)d}\right), \tag{2.7}$$

where $1 - e^{-\mu(E)d}$ is the quantum detection efficiency (QDE), i.e. the fraction of X-ray photons which interact with the scintillator, d the thickness of the scintillation

(a) Normalized X-ray spectra of spherical tungsten targets of various diameters.

(b) Effective spectrum of the X-ray imaging system based on a spherical tungsten target of 40μm in diameter
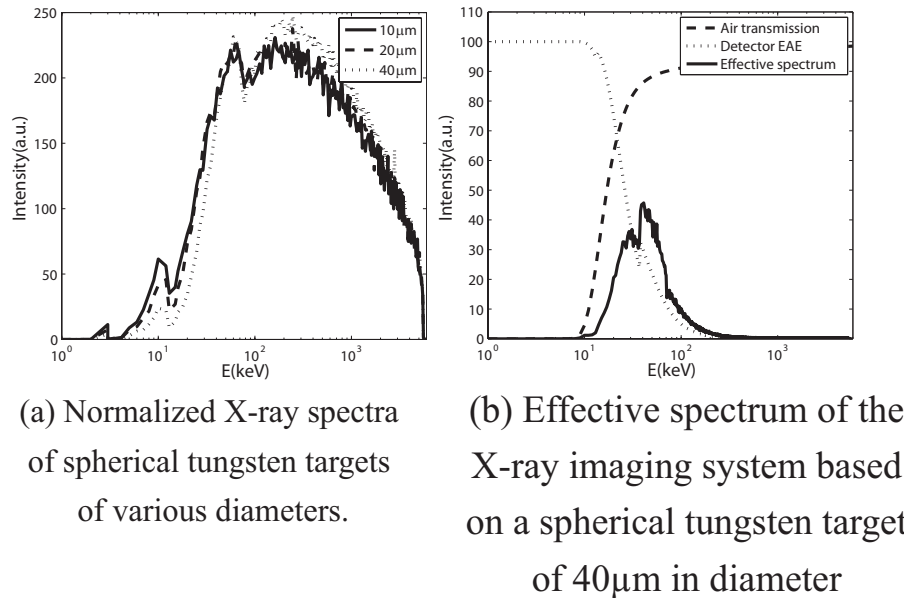
Figure 2.3: Spectra of tungsten spheres of $10\mu m$, $20\mu m$ and $40\mu m$ in diameter were computed using GEANT4 package. A monochromatic, spatially uniform electron beam with a total energy of 6MeV was assumed in the calculation. Estimation of the effective spectrum was done considering computed efficiency of the BaFBr:Eu detector and the transmission through five meters of air.

layer of the detector, and $\mu(E)$ the linear attenuation coefficient of BaFBr. The energy-absorption coefficient divided by the linear attenuation coefficient $\left(\frac{\mu_{en}(E)}{\mu(E)}\right)$ is the average fraction of energy transferred in each interaction with the scintillation layer. Both coefficients $\mu_{en}(E)$ and $\mu(E)$ are well documented [93]. The effective spectrum of the five meter long imaging system with the $40\mu m$ tungsten target and the BaFBr:Eu detector is depicted in Figure 2.3b.

Calculation shows that the total intensity of the target is not linearly dependent on the volume. The photon fluxes of the $40\mu m$ and $20\mu m$ tungsten spheres were found to be respectively 26.2 and 4.5 times higher than that of the $10\mu m$ target. This can be explained by self-absorption in the target. The same phenomenon contributes to beam hardening, taking place in the $20-40KeV$ regime, when the bigger target is used (Figure 2.3a). Such hardening of the emitted radiation lowers the sensitivity of the *PCI* system because the magnitude of the observed phase effect is proportional to λ^2 as can be seen from (Equation 2.3) and (Equation 2.4). On the other hand, high energy radiation might be more suitable because of the higher transmission through a particular object of interest.

It is apparent, therefore, that target size is an important characteristic of the *X-ray* source, which influences the sensitivity of the system to the phase effect, defines the source point-spread-function PSF_{src}, and determines the total brightness of the system [94]. The configuration of the target can be optimized using Monte-Carlo simulations considering the characteristics of the complete imaging system in each particular case.
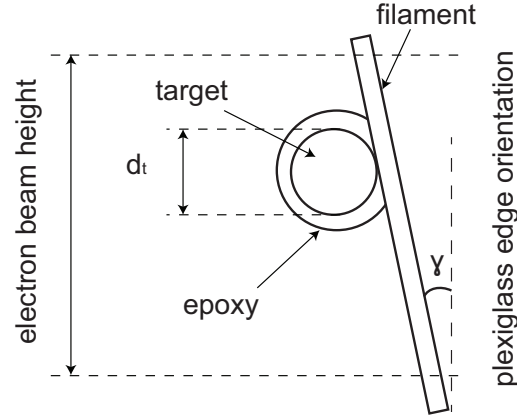

Figure 2.4: A schematic representation of the compound X-ray target (in the plane perpendicular to the optical axis). A small tungsten target is suspended in a droplet of epoxy on a thin carbon filament. There is a small misalignment angle γ between the filament and the direction of the plexiglass edge (vertical dashed line). A significant length of the filament is exposed to an electron beam.

2.3.3 Compound target model: spectrum

The results of the Monte-Carlo simulations for the spectrum of the X-ray source, based on tungsten spherical targets (Figure 2.3a), correspond well with the measurements of the MIRRORCLE-6X brightness [77]. However, we have found that the so called compound target model of the X-ray source leads to a consistent interpretation of the phase-contrast data that was obtained in our experiments.

It is known that in the MIRRORCLE-6X the tungsten target is suspended in a small droplet of epoxy attached to a thin carbon filament of $7.6\mu m$ in diameter. The whole construction is exposed to an electron beam of approximately $\sim 1mm$ in diameter (Figure 2.4).

It was assumed that the interaction between the spherical tungsten target, the epoxy droplet and the carbon filament is negligible during the X-ray production. Spectra

of the compound target model were calculated as a superposition of independently simulated spectra of the source components. Calculations were made considering spherical tungsten targets of $10\mu m$, $20\mu m$ and $40\mu m$, a $70\mu m$ sphere of epoxy, and a carbon cylinder of $7.6\mu m$ in diameter exposed to an electron beam with Gaussian profile and a FWHM of $1mm$.

Monte-Carlo simulations show that the epoxy droplet and the carbon filament contribute a comparable or even larger fraction to the emission spectrum as the small tungsten target (Figure 2.5a, Figure 2.5d, Figure 2.5g). The fraction of the effective spectrum that is produced by the tungsten sphere is 33% for a $10\mu m$ target, 62% and 89% for respectively a $20\mu m$ and a $40\mu m$ target. This indicates that there is a profound influence on the phase enhancement of the imaging system depending on the tungsten target size.

2.3.4 Compound target model: source point-spread-function

The point-spread-function of the compound target model PSF_{src} is determined as a sum of the relatively isotropic cross section of the tungsten target embedded in the epoxy droplet and the highly anisotropic profile of the carbon filament exposed to the electron beam. In each experiment the edge and the filament are both vertically oriented with a small unknown misalignment angle γ between them (Figure 2.4). The tungsten target is attached to the side of the filament and may also rotate around it due to the torsion of the filament. These factors are defining the projection of the X-ray source onto the image plane (and therefore the PSF_{src}) in each measurement. The design of the target forces us to introduce several fitting parameters into the compound target model to find a consistent interpretation of the measured data. To reduce the number of fitting parameters, it was decided to neglect the fraction of the PSF resulting from the epoxy droplet. Effectively we attributed its contribution to the emitted X-ray field to the small spherical target embedded in it. The first parameter is a fraction f of the X-rays that are not produced in the tungsten target, but in the carbon filament. As a result, the image observed with the detector is the weighted sum of the image produced by the radiation from the target I_t and the filament I_w:

$$I = (1 - f)\,I_t + (f)\,I_w.$$

(a) Calculated *emission spec-trum* of the compound target components.

(b) Effective spectrum of the system.

(c) Relative contributions of the compound target components to the total spectrum.

(d) Calculated *emission spec-trum* of the compound target components.

(e) Effective spectrum of the system.

(f) Relative contributions of the compound target components to the total spectrum.

(g) Calculated *emission spec-trum* of the compound target components.

(h) Effective spectrum of the system.

(i) Relative contributions of the compound target components to the total spectrum.
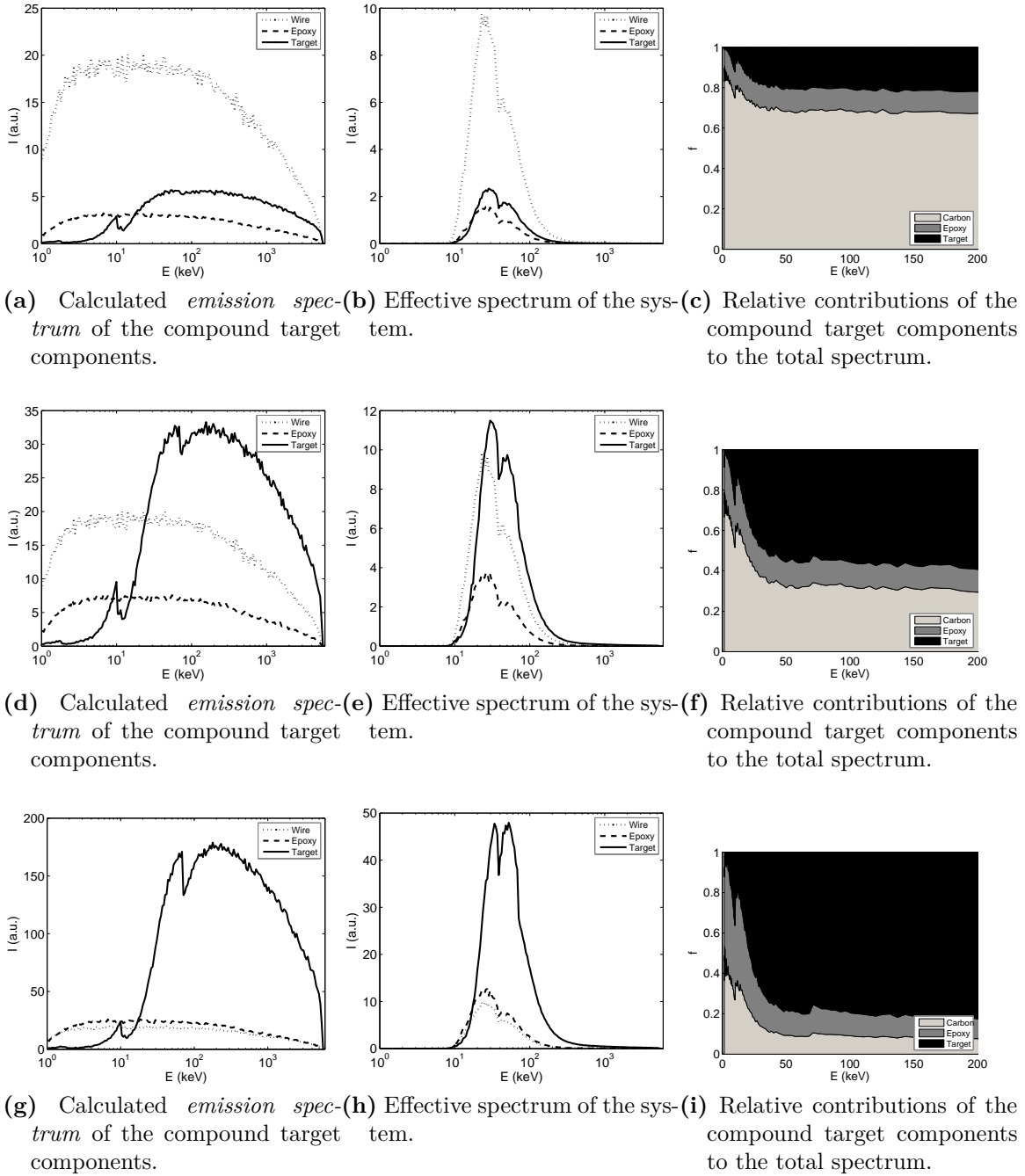
Figure 2.5: Normalized spectral characteristics (dose per solid angle unit) of the compound target components with $10\mu m$ (top), $20\mu m$ (middle) and $40\mu m$ (bottom) tungsten sphere.

Images I_t and I_w will be distinct due to two principal phenomena. Firstly, the carbon filament and the target are emitting different X-ray spectra (see Figure 2.5),

therefore the phase effects in images I_t and I_w are not exactly the same. Secondly, the point-spread-functions of the target $\mathrm{PSF_{src,t}}$ and the filament $\mathrm{PSF_{src,w}}$ are different due to the shape of the targets. If we assume that the X-ray production is homogeneous over the volume of the target and neglect absorption of X-rays inside the target, the shape of its $PSF_{src,t}$ is equivalent to the projection of its volume. Because the image of the homogeneous plexiglass plate can be considered as a one dimensional edge profile, the point-spread-function is projected onto a line perpendicular to the direction of the edge. We approximate the one-dimensional target $PSF_{src,t}$ as a normalized projection of a sphere with radius R_t:

$$\mathrm{PSF_{src,t}}\left(x\right) = \begin{cases} \frac{3}{4R_t^3}\left(R_t^2 - x^2\right) & x < R_t \\ 0 & x \geq R_t \end{cases}$$

The projected PSF of a cylindrical filament with radius R_f is likewise:

$$\mathrm{PSF_{cylinder}}\left(x\right) = \begin{cases} \frac{2}{\pi R_f^2}\sqrt{R_f^2 - x^2} & x < R_f \\ 0 & x \geq R_f \end{cases}$$

Generally, there is a small angle γ between the direction of the filament and the edge of the plexiglass plate (see Figure 2.4). This extends the $PSF_{src,w}$ by the projection of the profile of the *electron beam* along the filament onto a line perpendicular to the edge. If we assume that the *electron beam* has a Gaussian-shaped intensity distribution along the filament with a FWHM of h, the projection of the beam $\mathrm{PSF_{beam}}$ is also Gaussian-shaped with a FWHM of $h\sin\gamma$. Therefore, the full $PSF_{src,w}$ of the filament is:

$$\mathrm{PSF_{src,w}}\left(x\right) = \mathrm{PSF_{cylinder}}\left(x\right) * \mathrm{PSF_{beam}}\left(x, h\sin\gamma\right) \tag{2.8}$$

The mounting of the target on the side of the filament (see Figure 2.4) causes a potential misalignment of the centers of the filament and the sphere. This causes an arbitrary spatial shift Δx between the intensity images I_t and I_w.

The observed phase-contrast edge profile $I\left(x\right)$, taking all described effects into ac-

count, is given by:

$$
\begin{aligned}
I\left(x\right) \;=\; & \left(1-f\right)\text{PSF}_{\text{src,t}}\left(\frac{x}{M-1}\right) * \text{PSF}_{\text{det}}\left(x\right) * I_t\left(x + \left[M-1\right]\Delta x\right) + \\
+\;\; & \left(f\right)\text{PSF}_{\text{src,w}}\left(\frac{x}{M-1}, h\sin\gamma\right) * \text{PSF}_{\text{det}}\left(x\right) * I_w\left(x\right) \qquad\qquad (2.9)
\end{aligned}
$$

2.4 Results

In the current paper we present the phase-contrast enhancement in four series of 43 measurements of a $1.95mm$ thick plexiglass plate.
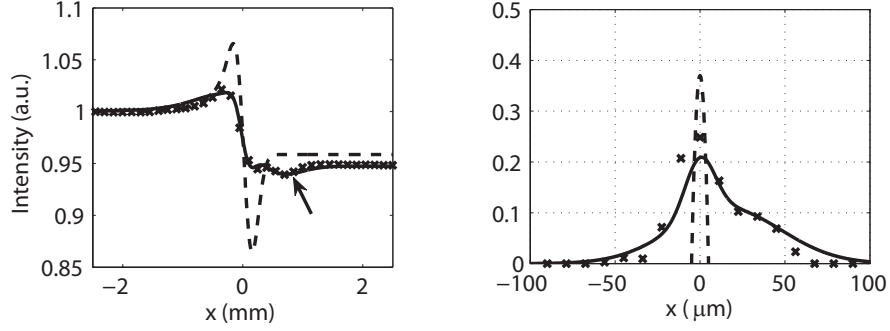
As described in the subsection 2.2.3, each series of images is taken for a range of edge orientations ($\sim\pm3°$) relative to the direction of the X-ray beam. Examples of the acquired profiles are depicted in the Figure 2.6(a,b and c). The figures show a large discrepancy between the measured edge profiles and the results of simulations based on a simple spherical target model.

Introduction of the compound target model, described in subsection 2.3.3, allows for a very accurate simulation of the measured data, but it requires fitting of the parameters f, $h\cdot\sin\left(\gamma\right)$, and Δx that represent the misalignment between the orientation of the plexiglass edge and the components of the X-ray source.

The source point-spread-function PSF_{src} was estimated using Wiener deconvolution [95] of the acquired images with the profile resulting from the model based on the fitted parameters. It is shown in Figure 2.6(a, ,b and c) that the estimated PSF_{src} corresponds to the PSF_{src} of a compound target model.

2.4.1 Stability of fitting

Results of fitting the compound model parameters to the data acquired in three experimental data collection sets are presented in Figure 2.7(a, b and c). The sets consist in total of 31 measurements taken in the orientations range $\pm3°$, with magnification $M = 14.3$, system length $R_1 + R_2 = 5.41m$, using a $10\mu m$ tungsten target. A typical integration time was $600sec$ per image.

(a) #137: $\Theta = 0.20°$ $f = 0.78$, $\Delta x = -16$ μm, $h \sin \gamma = 73$ μm
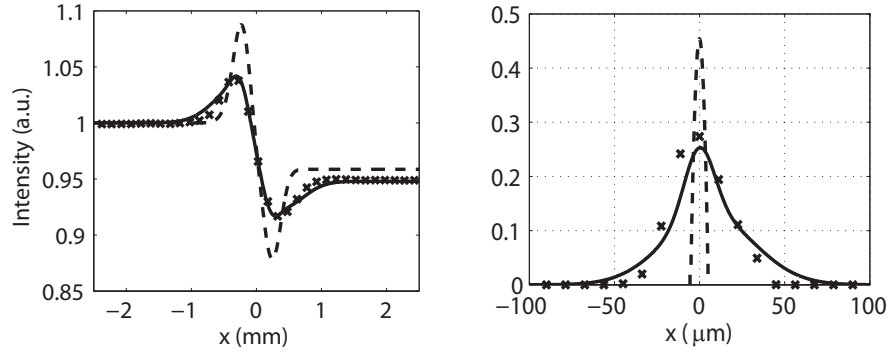
(b) #156: $\Theta = -0.90°$ $f = 0.75$, $\Delta x = -6$ μm, $h \sin \gamma = 59$ μm
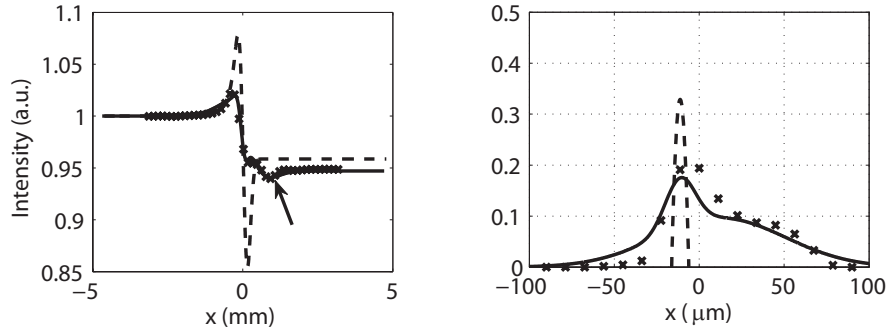
(c) #159: $\Theta = -0.20°$ $f = 0.81$, $\Delta x = -24$ μm, $h \sin \gamma = 87$ μm

Figure 2.6: On the left: three profiles (crosses) measured at different angles of incidence Θ with magnification $M = 14.3$, system length $R_1 + R_2 = 5.41$m, a $10\mu m$ tungsten spherical target. Note the extra wiggle depicted with a small arrow in (a) and (c). The dashed lines are the modeled results for an ideal spherical target ($f = 0$) and the solid lines are the results for the compound target model with the indicated parameters. Right: the total PSF of the imaging system (source and detector contributions) estimated with a Wiener filter (crosses). The dashed lines show the PSF_{src} of the spherical target alone and the solid lines represent the simulated total PSF of the imaging system using the fitted parameters for the compound target model (Equation 2.8).

A considerable variation of the parameters throughout the series is apparent, how-ever, linear trends in their variation can be found when the experimental data is divided into the three sessions in which the images were acquired (#131-141, 143-157 and 158-162) (see Figure 2.7(a, b and c)). This may be explained by the two resets of the setup that took place exactly after measurements #141 and #157 were taken. A linear change in the parameters, that are describing the compound target, may be explained by a drift of the suspended target during the measurement.

Such drift will of course not be relevant if the target PSF_{src} is isotropic, which can potentially be achieved by reduction of the carbon filament fraction that is exposed to the electron beam in the MIRRORCLE-6X or by increasing the volume of the spherical part of the target.

Figure 2.7(d) demonstrates that a reasonable match between the experimental val-ues of the *phase-contrast enhancement* and the modeled values can be achieved using only the average values of the fitted parameters. The compound target model shows that the *phase-contrast enhancement PCE* of the current system is decreased in the performed experiment by a factor of 2 to 5 compared to the system with the same geometry but using an ideal $10\mu m$ spherical tungsten target.

Another illustration of the results obtained with the compound target model is given in Figure 2.8. The experimental series are acquired with magnification $M = 12.8$, system length $R_1 + R_2 = 5.31m$, and a $10\mu m$, $20\mu m$ and $40\mu m$ tungsten target. The compound target model uses values for f obtained in Monte-Carlo simulations of the X-ray emission by the target components (subsection 2.3.3) and the other two parameters (Δx, $h \sin \gamma$) are found by least-squares fitting.

The predicted *PCE* based on an ideal spherical target is too large for the small targets by approximately a factor of 2 compared to the experimental data (see Figure 2.8). The results of the *compound target* model, on the other hand, are very close to the experimental data. They do not only reproduce a generally lower *PCE* in all three experiments, but also indicate that the *PCE* may be higher with a larger target depending on the angle of incidence.

Namely, the $40\mu m$ tungsten target dominates the other emitting components of the MIRRORCLE-6X (providing 89% of radiation according to the Monte-Carlo simu-lations). That is why it can produce a better performance compared to the smaller targets due to an effectively sharper point-spread-function. This also explains why the experiment that involves the bigger target is less influenced by the anisotropy

of the MIRRORCLE-6X source (see Figure 2.8).

(a) Filament radiation fraction f

(b) Relative position of the tungsten target Δx

(c) Length of radiating filament $h \cdot \sin{(\gamma)}$

(d) Comparison of the experimental data with the model data for an average set of the fitted parameters
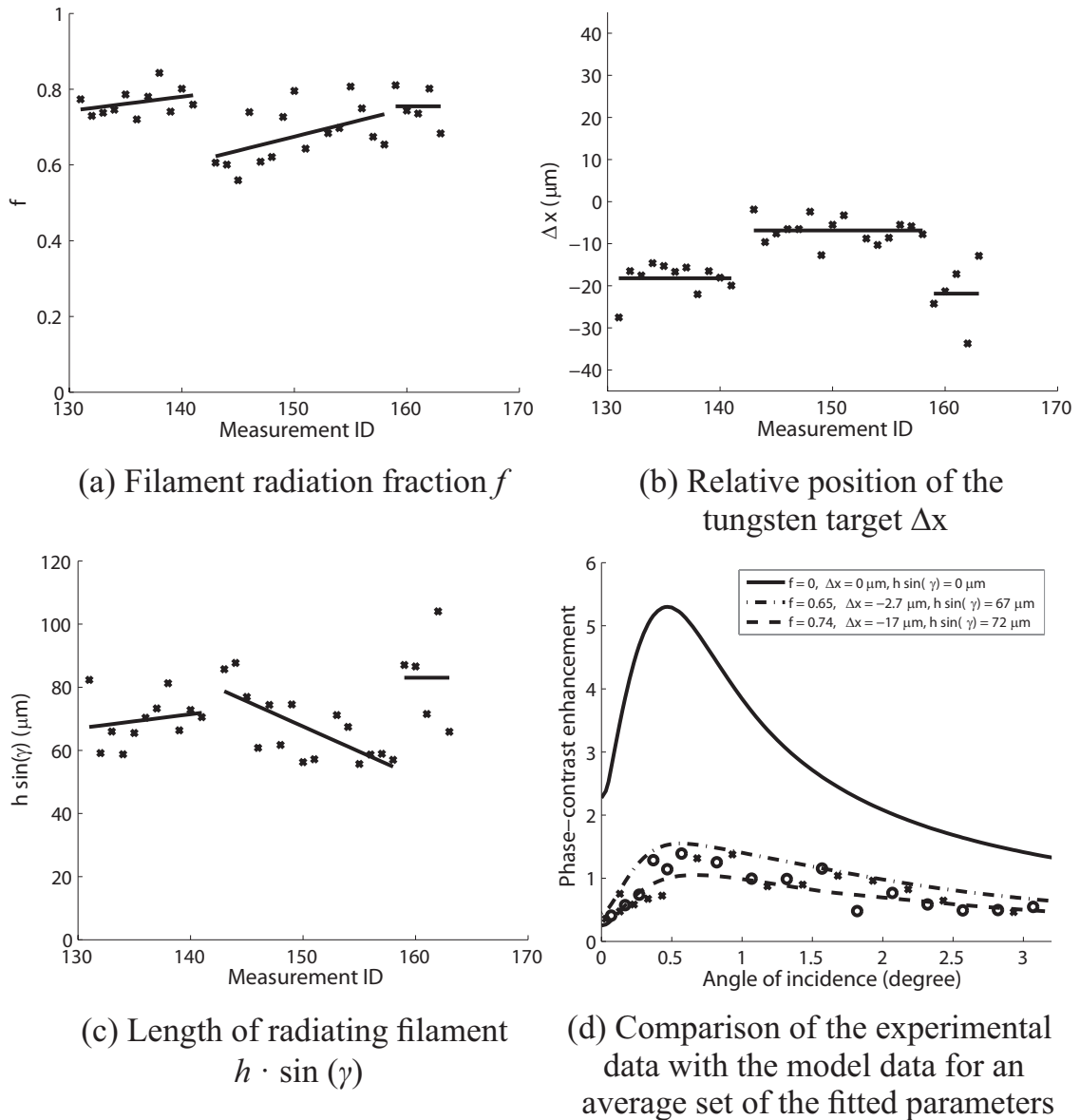
Figure 2.7: (a, b, c) The result from fitting the parameters of the compound target model to three sets of measurements. The solid lines indicate trends in the data over time per measurement series. **(d)** The measured (crosses and circles) and modeled (lines) phase-contrast enhancement as a function of angle of incidence. The crosses indicate measurements done at negative angles of incidence. The solid line is the result for $f = 0$ and the dashed lines are the results for two typical sets of values from (a), (b) and (c). Measurements done with $M = 14.3$, $R_1 + R_2 = 5.41$m, and a $10\mu m$ tungsten spherical target.

2.4.2 Phase-contrast enhancement of MIRRORCLE-6X

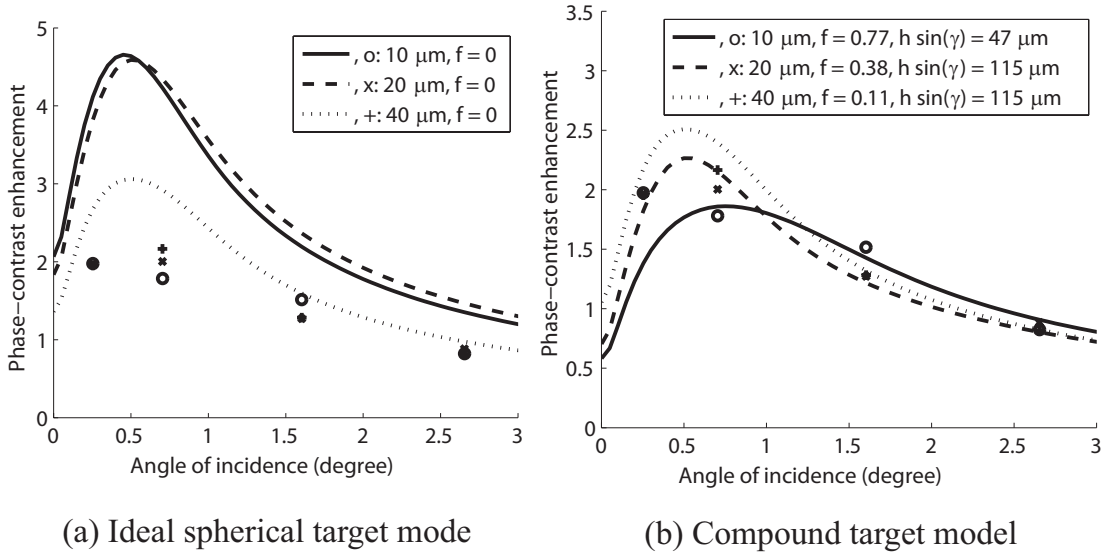(a) Ideal spherical target mode   (b) Compound target model

Figure 2.8: The phase-contrast enhancement for three series measured with spherical tungsten targets of 10, 20 and $40\mu m$ in diameter (denoted respectively by circles, crosses, and plus-signs). Measurements were done using the same setup geometry $M = 12.8$ and $R_1 + R_2 = 5.31$m. (a) demonstrates the discrepancy between the measured data and calculated values (solid, dash, point-line) using an *ideal spherical target* and (b) shows the correspondence of the measured data and calculated values using the *compound target model.*

The increase of contrast at a sharp plexiglass edge due to the *phase-contrast effect* of the MIRRORCLE-6X was observed to be between 100% and 200% in the current implementation. However, an accurate measurement of the *phase-contrast enhancement* was found to be particularly unstable. The instability can be attributed to the anisotropy in the resolution of the system caused by the radiation emitted from the various components comprising the X-Ray source.

According to calculations, if no (or almost no) radiation is produced by the components other than the target, the current system based on the MIRRORCLE-6X will yield a *PCE* of 400% to 500% (see Figure 2.7(d)). That could be potentially achieved using constructions made of carbon nanomaterials. Effective reduction of the X-Ray source size below $30 - 40\mu m$ can in principle be achieved without any modifications in the MIRRORCLE-6X design. A system of double bend Laue monochromators [96] would be required for patient imaging to select the appropriate X-ray spectrum and to limit the source size. A choice of X-ray detector with a higher resolution

($\lesssim 50\mu m$) will permit using a geometry with lower magnification which yields even higher levels of *PCE.*

Using the conversion factor by Yamada [79] to estimate the brightness from the measured radiation dose shows that the MIRRORCLE-6X should be capable of yielding the brightness on the order of $10^{10} - 10^{11} photons/(s \cdot mrad^2 \cdot 0.1\% band)$, which means that monochromatized beams with fluxes ranging from $10^8 photons/(s \cdot mrad^2)$ to $10^{11} photons/(s \cdot mrad^2)$ should be possible, depending on the bandwidth of the monochromator.

Other X-PCI techniques than in-line X-PCI can be potentially designed with the MIRRORCLE-type sources. For instance, gratings-based X-PCI or aperture-based X-PCI implementations seem to be promising since they can tolerate a significantly larger source size. A transition to a digital detector and addition of the monochromator is of course inevitable for these techniques.

2.5 Conclusions

The performance of an *X-PCI* prototype based on the MIRRORCLE-6X X-ray source was characterized using the edge response of the system. The *phase-contrast enhancement* factor was measured in a series of experiments as the ratio between the phase and absorption contrast produced by the plexiglass plate. It was found to be particularly sensitive to the edge orientation due to the anisotropy of the X-ray source point-spread-function. The observed *PCE* values were found to be between 100% and 200% in different configurations of the system.

The role of the X-ray source target size was investigated using Monte-Carlo simulations using the GEANT4 software package. Calculations show that the target size has a considerable influence on the low-energy part of the emission spectrum ($10 - 40 KeV$ of a total $0.001 \sim 5.5 MeV$). Even more important, the components used for mounting of the spherical target in the present design may emit up to 70% of the total radiation in case of a $10\mu m$ spherical tungsten target, down to 10% for the $40\mu m$ targets.

As a result, the same or higher performance in terms of *PCE* values was observed in experiments when a $40\mu m$ target was used instead of $10\mu m$ or $20\mu m$ targets. The emission produced by the components of the mounting cannot be fully avoided in

the current implementation of the system due to the limited focusing of the electron beam in the synchrotron ring. This factor determined a minimal diameter of the tungsten target that could be effectively used in the MIRROCLE-6X to $30 - 40 \mu m$.

Calculations demonstrate that after achieving a significant reduction of the radiation emitted by the target mounting, the *PCE* levels of the MIRRORCLE-6X can be improved by a factor of 2 to 5 by allowing to use smaller targets.

3 Non-destructive investigation of 3D microstructure of steel

Abstract[1]

This work presents the development of a non-destructive imaging technique for the investigation of the microstructure of cementite grains embedded in a ferrite matrix of medium-carbon steel. We show that non-destructive, in-line X-ray phase-contrast tomography (PCT) can be used to study the three-dimensional morphology of individual cementite particles in steel with a spatial resolution of approximately 1.5 μm in a sample volume of $600{\times}400{\times}250$ μm^3. The smallest detectable cementite grains are 5 μm in size. A second imaging technique, X-ray diffraction-contrast tomography (DCT), was employed to obtain information about the shapes and crystallographic orientations of the distinct ferrite grains surrounding the cementite structures. The results of PCT correspond very well to optical microscopy in combination with serial sectioning. We estimate the temporal resolution of PCT for in situ studies of cementite to be 30 min.

3.1 Introduction

The morphology of cementite in steel has a large effect on the mechanical properties of steel [98], which is the reason for world-wide studies into the three-dimensional morphology of cementite [99, 100, 101, 102, 103]. The morphology of cementite in steel can be divided into three main categories: 1) large (few to tens of micrometers)

---

[1]This work is published in: [97] A. Kostenko, H. Sharma, E. G. Dere, A. King, W. Ludwig, W. van Oel, S. Stallinga, L. J. van Vliet and S. E. Offerman, "Three-dimensional morphology of cementite in steel studied by X-ray phase-contrast tomography," Scripta Materialia, **67**, 261–264 (2012).

sphere-like particles of cementite in a matrix of ferrite or austenite, 2) lamella of cementite in pearlite, and 3) carbides (nanometer to submicron particles) of cementite in bainite and in tempered martensite. Spheroidization of cementite is an example of an important industrial process, e.g. in the production of rolling bearings, in which the lamella of cementite in pearlite are transformed to spheres of cementite with the aim to facilitate machining, and warm- and cold-forming operations of the steel.

Studying the evolution of the morphology of the cementite in 3D during spheroidization is challenging, because the current state-of-the-art techniques require destructive serial sectioning [99, 100, 101, 102, 103], which has the intrinsic limitation that the evolution of individual cementite particles cannot be studied. Only the average growth behaviour of the cementite particles can be studied by serial-sectioning. Moreover, the holes present in naturally grown cementite lamella also need to be investigated, because the work of Wang [99] has shown that the intrinsic holes play an important role in the initiation and development of pearlite spheroidization.

For conventional x-ray tomography techniques based on attenuation-contrast, the density difference of 3% between cementite and ferrite is too small to obtain contrast. The aim of this research is to determine the feasibility of studying the 3D morphology of cementite in steel by using x-ray phase-constrast tomography, which, in case successful, will open the door to the study of the evolution of the morphology of individual cementite particles in 3D during processing of steel.

3.2 Materials and Methods

3.2.1 Experimental setup

The specimens in our study were manufactured from steel with the following composition (in wt.%): 0.6 carbon, 0.6 manganese, and 2.8 copper. The steel sample was annealed in vacuum of 10^{-5} mbar at constant temperature of 700°C for times varying between 1 and 70 hours. Annealing was followed by cooling to room temperature at a rate of 2°C/min. Cementite structures corresponding to different annealing times were studied using light microscopy and serial sectioning with a step size of approximately 2.5 μm. Figure 3.1 shows that cementite grains vary in size between one and tens of micrometers depending on the duration of the treatment. The specimens for
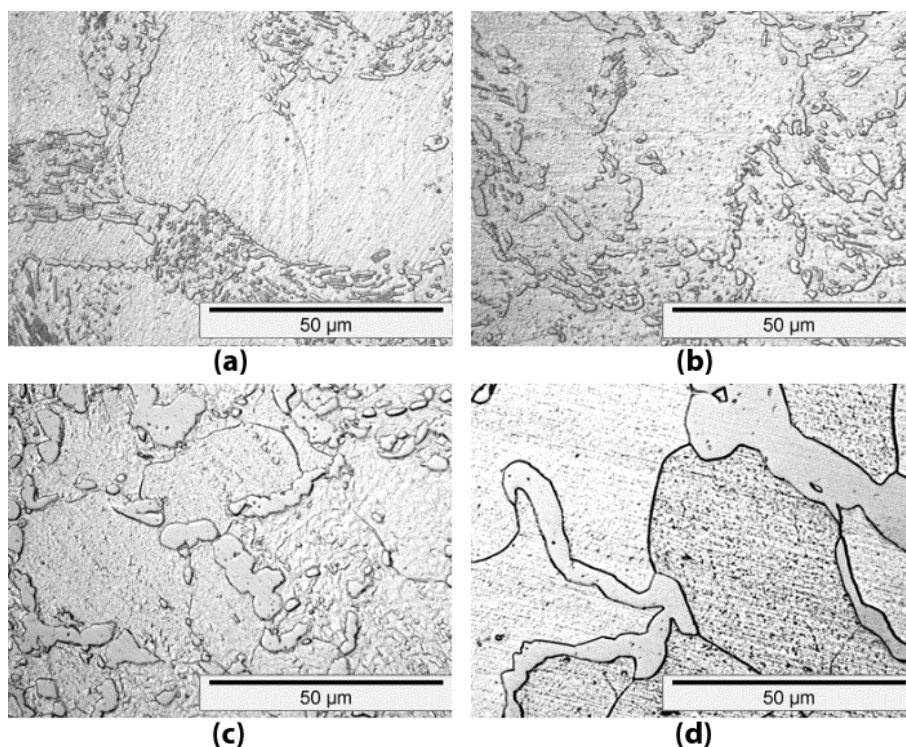
Figure 3.1: Light microscopy of the cementite-ferrite structure in steel specimens annealed at a temperature of 700ºC for a) 1, b) 10, c) 20, and d) 70 hours.

the PCT-measurements are 200 to 400 μm thick.

The phase-contrast imaging experiments were performed at the materials science beamline ID11 of the European Synchrotron Radiation Facility (ESRF) in Grenoble (France). Beamline ID11 is based on an undulator X-ray source that produces a quasi-parallel beam with a source size of FWHM = 57x10 μm^2 (HxV). The X-ray beam is monochromatized to an x-ray energy of 40 keV using a Laue-Laue crystal with an energy bandwidth $\triangle E/E = 10^{-4}$. We used the first experimental hutch that allows a source-to-detector distance of 48 m which corresponds to a spatial coherence length of approximately 9x50 μm^2 (HxV). A FReLoN 2K CCD detector was coupled to a 30 μm thick scintillator via a 20x magnification objective lens. The resulting spatial resolution was estimated from the acquired images by estimating its point spread function; it resembles a Gaussian with a FWHM of approximately 1.4 μm. For each tomographic acquisition series 1200 projections were recorded uniformly spaced over the full 360º angular range. The projections were acquired in the format of 1024x1024 with a pixel size of 0.75 μm at three different sample-to-detector distances: 3 mm, 68 mm, and 208 mm.

3.2.2 Pre-processing and image reconstruction

Phase-contrast imaging is based on Fresnel diffraction of light at the inhomogeneities of the electron density within the specimen [49]. Ferrite and cementite have different electron densities, mainly due to the high carbon content in the cementite. As a result X-rays are diffracted at the interfaces between the cementite and ferrite. If the specimen is illuminated with a monochromatic coherent beam, Fresnel diffraction rings can be observed around the boundaries of the cementite grains when a detector is placed at a sufficiently large distance behind the specimen. The recorded image that contains such diffraction signal can be used to identify cementite structures (see Figure 3.2). Furthermore, an electron-density map of the specimen can be calculated using so-called phase-retrieval techniques [52, 54, 55, 104] followed by tomographic reconstruction(see Figure 3.2).

All recorded images were pre-processed with a standard dark-field correction method using a dark-field reference image acquired once per tomographic dataset. Slow variations in the illumination of the specimen were corrected using reference flat-field images acquired after every 100 projections, while rapid variations were corrected in each projection using a flat-field that was estimated from the non-attenuated pixel values aside the object.

A recorded phase-contrast image of the cementite is often contaminated by so called extinction spots - areas on the image with low intensity due to diffraction of the incoming X-ray beam on the atomic lattice of a ferrite grain. Each extinction spot occurs only in those projections in which the orientation of the grain with respect to the incoming beam corresponds to the Bragg diffraction angle. That property allows us to significantly reduce the effect of extinction spots. The intensity variations caused by the Bragg diffraction can by estimated by applying a high-pass filter to the sinogram along the angular dimension and a low-pass filter along the spatial dimensions. The estimated intensity of the extinction spots can be then subtracted from the sinogram.
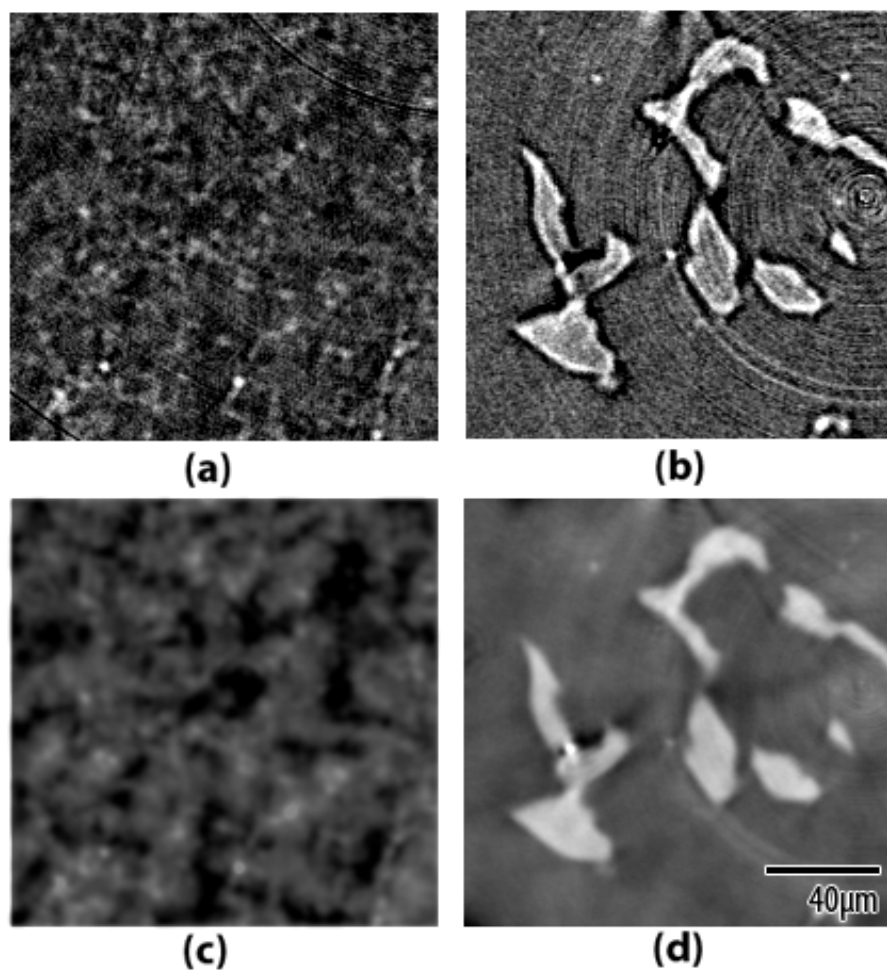
Figure 3.2: A single slice of the tomographic reconstruction of the steel specimens annealed for 20 hours (a, c) and 70 hours (b, d). The results (a) and (b) show reconstructions based on raw phase-contrast data (no phase retrieval), and (c) and (d) show electron density reconstructions based on phase retrieved images.

Misalignments between the projections in a sinogram reduce the quality of subsequent tomographic reconstruction. Such misalignments were estimated from the acquired data and did not exceed roughly one micrometer throughout the complete dataset. A procedure described in [105] was applied to the data in order to compensate for the misalignments between the projections.

A linear approximation to Fresnel diffraction [45] yields the so called Mixed TIE-CTF model (Transport of Intensity Equation - Contrast Transfer Function) for inline phase-contrast imaging. It is based on the assumption that the phase image of
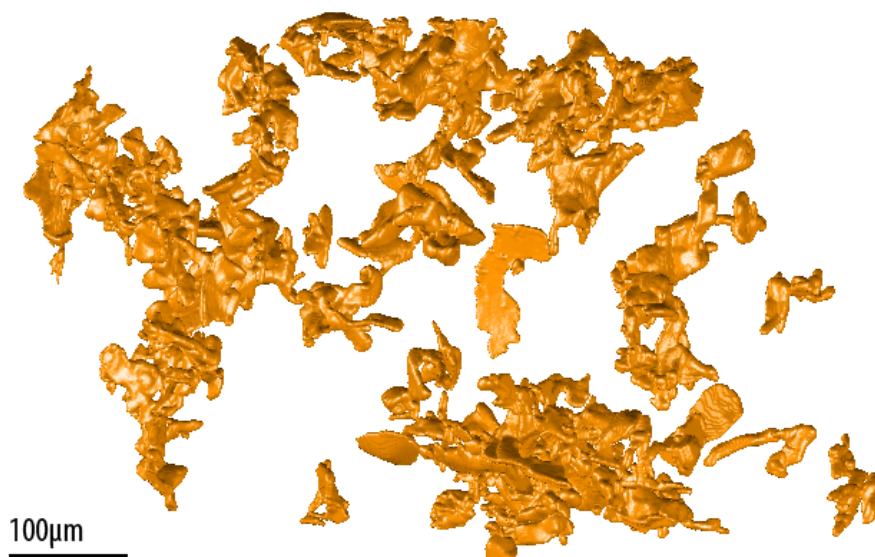
Figure 3.3: 3D rendering of the cementite structure in ferrite bulk. The total volume dimensions are 600x400x250 μm^3. Rendering shows a highly interconnected network of cementite particles.

the specimen $\varphi(x)$ is sufficiently smooth:

$$|\varphi(x) - \varphi(x + \lambda R u_{\max})| \ll 1, \tag{3.1}$$

where λ is a wavelength of the monochromatic x-ray beam, R is an object-to-detector distance and $u_{\max}$ corresponds to the maximal spatial frequency contained in the recorded phase image. This approximation breaks down around steel-to-air interfaces, including the outside boundaries and the pores of the specimen. It is, however, valid for the ferrite-cementite interfaces and should provide a correct image of the cementite grains away from the specimen boundaries. The observed image can be described in Fourier space as a combination of an attenuation term and a phase term:

$$F(I_R) = \cos(\lambda R u^2) \cdot F(I_0) + sin(\lambda R u^2) \cdot F(I_0 \varphi), \tag{3.2}$$

where $F(I_R)$ is the Fourier transform of the image observed at an object-to-detector distance R using monochromatic light of wavelength λ, u represents the spatial frequency, I_0 is the attenuation image of the object at $R = 0$, and φ is the projected phase image of the object at $R = 0$. At a distance R equal to zero, only the

attenuation image of the object will be observed: $F(I_R) = F(I_0)$. When the distance R is large, the second term, which corresponds to the phase-contrast contribution, will appear. Unfortunately, when the object-to-detector distance is increased, the second term in Equation 3.2 only produces high contrast in a limited range of spatial frequencies, namely when $0 < \lambda R u^2 < 1$. The second term will reduce to zero at a set of spatial frequencies $\lambda R u^2 = 0, 1, 2 \ldots$ and is attenuated by an envelope as result of the finite source size and a finite detector resolution. In practice, it is often infeasible to reconstruct the image at spatial frequencies $\lambda R u^2 > 1$. The later determines how much the phase-contrast can be enhanced by allowing a large object-to-detector distance before the resolution will be compromised. The standard solution to overcome the problems associated with the zero-crossings in the CTF is to acquire each projection angle of the specimen at multiple distances. Each image recorded at a certain distance R will contain an enhanced phase-contrast signal in a particular frequency range. Together these images will contain the information over a wide range of spatial frequencies. A complete tomographic acquisition in such case will be composed from several sinograms, each of them recorded at a different object-to-detector distance R. The phase image $\varphi(x)$ can be reconstructed from the recorded phase-contrast images using the following formula [51]:

$$F(\varphi) = \frac{C \sum_R F(I_R) \sin(\lambda R u^2) - A \sum_R F(I_R) \cos(\lambda R u^2)}{2BC - 2A^2 + \epsilon}, \tag{3.3}$$

where $A = \sum_R \sin(\lambda R u^2) \cos(\lambda R u^2)$, $B = \sum_R \sin(\lambda R u^2)^2$, $C = \sum_R \cos(\lambda R u^2)^2$ and ϵ is a small constant introduced to avoid division by zero. Such an approach requires a very large number of images per dataset which increases the total acquisition time and may introduce problems with inter-sinogram alignment. Another downside of a multiple distance approach is that the phase term in Equation 3.2 remains zero at spatial frequency $u = 0$ irrespective of the object-to-detector distance R. The latter means that the phase image can never be reconstructed at very low spatial frequencies.

An alternative approach to Mixed TIE-CTF phase retrieval was proposed for homogeneous specimens in [52] and modified in [54, 104]. We refer to it as the phase-attenuation duality approach. The underlying assumption of this approach is that the phase image φ is highly correlated with the attenuation image I_0. That allows replacing two unknown images φ and I_0 from the right hand side of (2) with a single
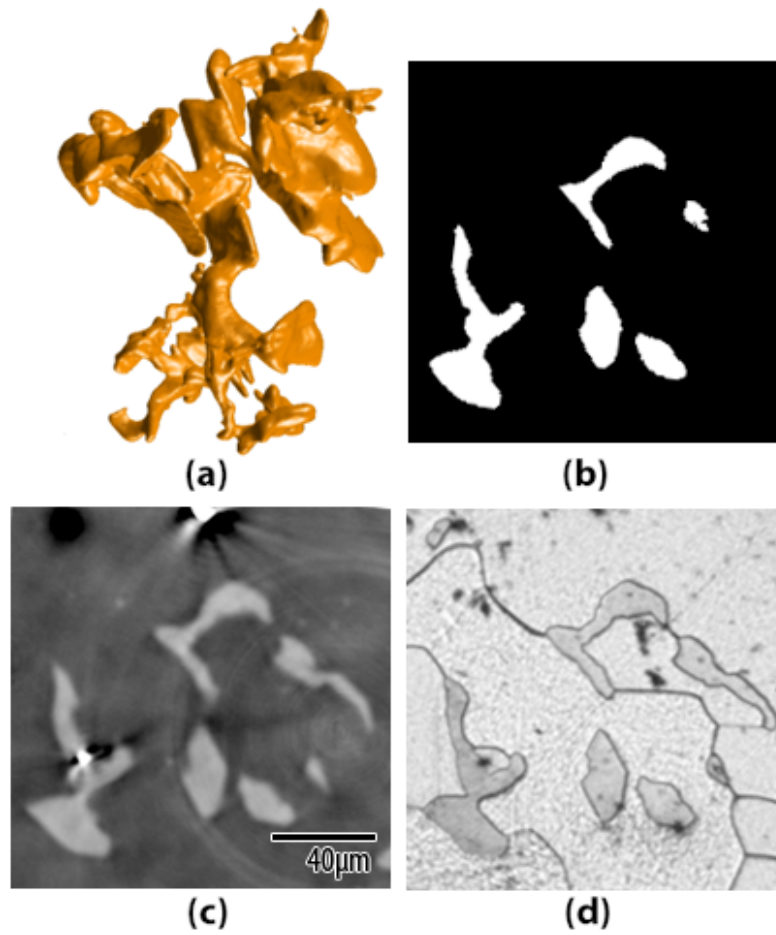
Figure 3.4: Rendering of a single interconnected cementite structure, where (b) is a cross-section made in X-Y plane in the middle of the grain, (c) shows the corresponding plane in the phase-contrast data and (d) is the corresponding optical image obtained from the serial sectioning of the specimen.

unknown image I_0 and rewrite the phase-contrast model in a following way:

$$F(I_R) = (\cos(\lambda R u^2) + 2\alpha \cdot sin(\lambda R u^2)) \cdot F(I_0), \tag{3.4}$$

where α is a constant that depends on the composition of the specimen. It quantifies the ratio between attenuation and phase effects. Reconstruction based on Equation 3.4 allows retrieving an image of the specimen from a single recorded image I_R. Unfortunately, similar to Equation 3.2, it is impossible to reconstruct the image for spatial frequencies at which the right hand side of the equation is zero. In order to overcome that, a solution similar to Equation 3.3 can be used. By combining Equation 3.3 and Equation 3.4 we can reconstruct the image of a homogeneous

specimen over a wide frequency range including the low frequencies. The resulting phase-attenuation formula can be written as:

$$F(I_0) = \frac{\sum_R A_R F(I_R)}{\sum_R A_R^2}, A_R = (\cos(\lambda R u^2) + 2\alpha \cdot sin(\lambda R u^2)). \tag{3.5}$$

Here the number of images that have to be recorded per projection angle can be selected depending on the desired frequency bandwidth of the reconstruction.

Results and conclusions

A standard tomographic reconstruction - Filtered Back Projection (FBP) - can be performed with or without applying phase retrieval to the recorded phase-contrast images as shown in Figure 3.2(a,b) and Figure 3.2(c,d) show the results of the tomographic reconstruction performed after the phase retrieval calculation based on Equation 3.5. It is interpreted as an electron density map of the specimen and can, for example, be used to render three-dimensional configuration of the cementite grains (Figure 3.4). It is also possible to apply tomographic reconstruction directly to the recorded phase-contrast data skipping the phase-retrieval step (Figure 3.2(a,c)). Such calculation results in an image that does not have a strict physical meaning but can also be suitable for analysis of the specimen's structure. Visually the FBP of the raw projections yields more contrast than the FBP of the retrieved phase images, which often may make it easier to observe small low-contrast structures.

Tomographic reconstructions from two different specimens are compared in Figure 3.2. The specimen that was annealed for 20 hours contains small 5-10 μm cementite grains that are barely detectable in our PCT data (Figure 3.2(a,b)) as a result of very weak phase-contrast. The specimen that was annealed for 70 hours contains large grains of cementite (~50 μm) that are easy to detect (Figure 3.2(b,d)). Both specimens contain large number of spherical pores with diameters in the range 1-4μm. Pores of this size are easily detectable in phase-contrast regime. In fact, they produce such a high contrast that it usually leads to so called streak artefacts in tomographic reconstruction.

Using a tomographic reconstruction of the electron density of the 70 hours specimen (Figure 3.2(d)) we could render a three-dimensional configuration of the cementite

grains (Figure 3.3). The average volume of interconnected cementite structures in the 70 hours sample is approximately $2 \cdot 10^4$ μm^3 which corresponds to a spherical cementite particle with the radius of 17 μm. The particles have very irregular geometries (Figure 3.4) which most likely correlate with the configuration of the grain boundaries of the surrounding ferrite grains, due to incomplete spheroidization. It is evident from the optical serial sectioning (Figure 3.1, Figure 3.4(d)) that the large cementite grains tend to form close to the ferrite grain boundaries. Unfortunately PCT does not provide information on the ferrite structure. In order to investigate how the configuration of the cementite grains is related to the surrounding ferrite, diffraction based technique similar to the Diffraction-Contrast Tomography (DCT) has to be employed along with the phase-contrast imaging. Currently, the diffraction data that was acquired by us for the sample used in PCT experiment yielded spatial resolution that was not sufficient for a conclusive analysis [105] (see the Appendix). We plan to combine higher resolution DCT acquisition with the improved contrast PCT data in a follow-up study.

Considering the experimental technique that was used in the current investigation, it is only possible to reliably detect large cementite grains that occur after very long annealing times. Information on the interface mobility and preferred growth orientation of the large cementite grains can be obtained in a time-dependent PCT experiment (with a resolution of 1.5 micrometers). It is, however, desirable to develop a technique suitable for observations of smaller cementite grains that form after shorter annealing times and ultimately cementite grains during the nucleation process. We believe that the parameters of the current PCT acquisition protocol can be relatively easy adjusted in order improve the sensitivity of the method by a large factor. The most important experimental parameters in PCT are the energy of the X-ray beam, the object-to-detector distance, the resolution of the detector, and the spatial coherency of the X-ray source. We expect that the resolution and the spatial coherency of the X-ray source can be improved by approximately a factor of 2 by adjusting parameters of the current experimental setup. If the projected thickness of the specimen is not exceeding 100 μm, the X-ray energy can be reduced from 40 KeV down to 30 KeV. Considering the properties of the propagation model (2) and the properties of materials, the magnitude of the observed phase-contrast effect is roughly inverse proportional to the third power of the X-rays energy. That means that the sensitivity of the method can be improved by a factor of 4 by decreasing the X-ray energy. Using the phase-attenuation duality approach it is possible

to perform tomographic reconstructions from the PCT data recorded at a single object-to-detector distance. That will most likely limit the acquisition time of a full tomographic dataset to less than 30 minutes at the ESRF or similar large-scale synchrotron radiation facility.

Based on the aforementioned analysis, we have shown that a state-of-the-art PCT approach is suitable for the detection of the cementite structures with sizes down to a few microns. We show that PCT can be used for the non-destructive study of the 3D-morphology of individual cementite particles in steel with a spatial resolution of approximately 1.5 μm in a sample volume of at least 600x400x250 μm^3. The PCT results correspond very well to optical microscopy in combination with serial sectioning. We demonstrate that PCT is suitable for the in-situ study of the evolution of the morphology of the cementite of individual cementite particles in 3D during processing of steel with an estimated temporal resolution of 30 minutes. This allows in-situ experiments aimed at investigating the cementite grain growth rates, the cementite morphology evolution, and the mobility of the ferrite-cementite interface in steel at elevated temperatures.

Appendix: Diffraction Contrast Tomography[2]

The combination of two complementary techniques: X-ray PCT and X-ray DCT, can be used to study the microstructure of cementite grains in a ferrite matrix. A single imaging beamline with sufficient spatial coherence and a suitable X-ray detector can be utilized for both PCT and DCT without significant changes to the beamline geometry or the components. When the beamline is switched from PCT to DCT mode only the detector has to be realigned to allow for the desired angular resolution and a sufficiently large field of view. A suitable scan series has to be recorded using a 360° scan protocol, which permits a reconstruction based on Friedel pair matching [45]. The structure of the ferrite grains cannot be reconstructed using phase-contrast imaging techniques since there is no variation of density or composition between the grains. Instead, the Bragg diffraction of X-rays on the ferrite lattice must be exploited. In order to perform a time-resolved study, the imaging techniques must

---

[2]A. Kostenko, H. Sharma, E. G. Dere, A. King, W. Ludwig, W. van Oel, S. E. Offerman, S. Stallinga and L. J. van Vliet , "In-line x-ray phase-contrast tomography and diffraction-contrast tomography study of the ferrite-cementite microstructure in steel," AIP Conference Proceedings **63**, 1437 (2012).
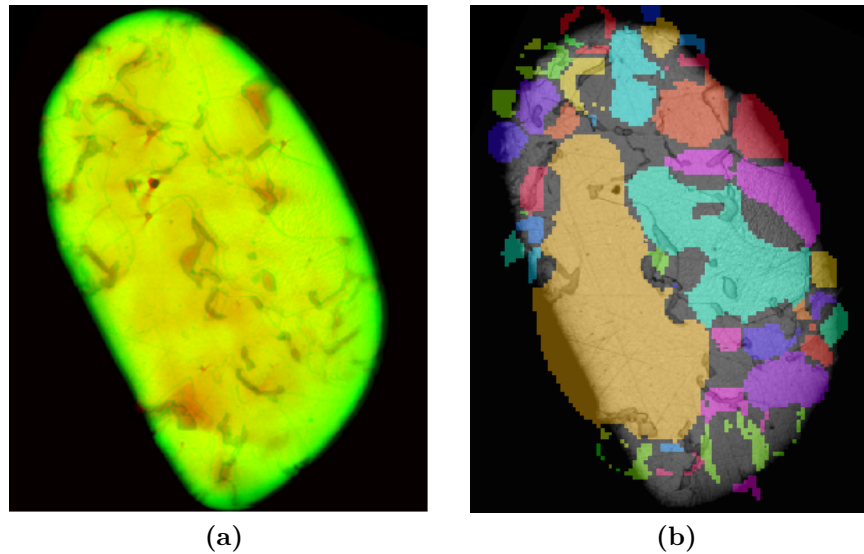
(a)   **(b)**

Figure 3.5: The results of the PCT and DCT reconstructions overlayed with the
optical images of the corresponding section of the specimen. (a) PCT reconstruc-
tion (red channel) overlayed with optical image (green channel). (b) The results
of the DCT grain tracking (color labels) overlayed with the optical image (gray).

allow for relatively short acquisition times (on the order of 1 hour or less) for a
complete 3D volume. That requirement can be satisfied using X-ray diffraction-
contrast tomography.

The diffraction-contrast images are recorded at 9.5 mm object-to-detector distance
using a full CCD (2048x2048) format with optical magnification corresponding to
a 3.75 μm sampling pitch. The DCT acquisition was done separately for five sub-
sections of the complete volume of the specimen in order to reduce the complexity
of the reconstruction. The data was processed using the grain tracking algorithm
proposed by Ludwig [45]. The algorithm is based on the assumption that the investi-
gated material is composed of crystalline grains that will diffract radiation according
to the Bragg law depending on their crystalline orientation. Each grain is assumed
to be an ideal single crystal that produces a diffraction spot that corresponds to the
geometrical projection of the grain in that direction. This method permits volumet-
ric reconstruction of the granular structure of the specimen based on the full field
images of the diffraction patterns acquired in 360º view range. Unfortunately, the
method is unable to reconstruct information about the local orientation gradients
inside single grains. As a result of deformations inside individual grains such gradi-
ents are present in the specimen under study causing the reconstruction approach to

become inaccurate. The result of DCT reconstruction based on the grain tracking approach is shown in Figure 3.5. Different grains reconstructed from DCT data are colour-coded and overlaid with the images obtained from optical microscopy. Comparison with the optical data clearly demonstrates that the current DCT approach fails inside the regions that most likely have a significant local gradient of crystalline orientation. These erroneous regions seem to occur around the grain boundaries and in those parts of the volume where many large cementite grains are found.

From Figure 3.5 it can be estimated that the reconstructed grain volumes cover approximately 80% of the actual ferrite grain volume. The grain boundaries are determined within 15-20 microns accuracy. A conventionally used morphological dilation algorithm can be applied to the reconstructed DCT data to 'fill-in' the gaps, does not improve the image quality significantly as the regions where the reconstruction fails are to large.

4 Algebraic phase retrieval

Abstract[1]

State-of-the-art techniques for phase retrieval in propagation based X-ray phase-contrast imaging are aiming to solve an underdetermined linear system of equations. They commonly employ Tikhonov regularization − an L2-norm regularized deconvolution scheme − despite some of its limitations. We present a novel approach to phase retrieval based on Total Variation (TV) minimization. We incorporated TV minimization for deconvolution in phase retrieval using a variety of the most common linear phase-contrast models. The results of our TV minimization was compared with Tikhonov regularized deconvolution on simulated as well as experimental data. The presented method was shown to deliver improved accuracy in reconstructions based on a single distance as well as multiple distance phase-contrast images corrupted by noise and hampered by errors due to nonlinear imaging effects.

4.1 Introduction

Recently, the field of X-ray phase-contrast imaging (PCI) has been growing rapidly. X-ray PCI found applications in materials science, ranging from investigating the microstructure of carbon-based materials [3, 4] to in-situ measurements of dynamic processes taking place in metal alloys and semiconductors [5, 6, 97]. X-ray PCI is also entering the field of pre-clinical bio-medical research, namely, small animal imaging and various ex-vivo/in-vitro studies [7, 13, 14, 15, 16, 17]. The increasing availability of the X-ray PCI techniques over the last years was stimulated by advances in instrumentation and phase retrieval algorithms.

---

[1]This work is published in: [106] A. Kostenko, K. J. Batenburg, H. Suhonen, S. E. Offerman and L. J. van Vliet, "Phase retrieval in in-line x-ray phase contrast imaging based on total variation minimization," Optics Express, **21**, 710–723 (2013).

The scope of our current investigation lays within phase retrieval for propagation-based X-ray PCI. For more than a decade various algorithms were developed to permit accurate reconstruction of the specimen's phase and attenuation images from phase-contrast data acquired using the propagation-based approach [47]. A major effort was aimed at the development of linear approximations to the image formation of PCI that would permit a stable solution of the resulting inverse problem [47, 49, 50, 51, 107]. Using these approximations, the phase and attenuation images of the specimen can be calculated from a series of phase-contrast images acquired at different propagation distances. To allow phase retrieval from a single phase-contrast image, methods based on prior information about the specimen's composition were developed [52, 53, 54]. They are referred to as the so called phase-attenuation duality models.

In all linear phase retrieval models the accuracy of the reconstruction is a function of spatial frequency. Depending on the acquisition conditions, the signal-to-noise ratio (SNR), and the fitness of the linear approximation, the phase image of the specimen will be irrecoverable within a particular set of spatial frequencies [55, 56]. In the case of multi-distance phase retrieval [51] this can lead to large errors at low spatial frequencies while in single-distance approaches [52, 53, 54] artifacts are produced at middle and high spatial frequencies. In order to avoid large errors in the reconstructed images, most of the phase retrieval approaches rely on a so called L2-norm based regularization also known as Tikhonov regularization. When L2 regularization is used, the solution that has the minimum L2-norm (i.e. Euclidean norm) is promoted. This leads to a suppression of spatial frequencies that are ill-determined by the phase retrieval model or heavily corrupted by noise. Such a solution may not be optimal, especially when it results in a strong suppression of a large band of low frequencies in multi-distance retrieval methods.

Another regularization approach that is currently used in an increasing number of image reconstruction applications is called Total Variation (TV) minimization. It was initially developed for image denoising [58] and recently been introduced in such fields as deblurring, super-resolution, inpainting and tomography [61, 62, 63, 64]. The idea underlying TV minimization is to promote a solution that has the sparsest gradient. It was theoretically proven [65] that under certain conditions TV minimization allows exact reconstruction of signals with a sparse gradient from highly incomplete sets of observations. In cases where the gradient of the reconstructed image is not exactly sparse, TV minimization is nevertheless preferred to L2 regu-

larization in many applications [108].

In this paper we introduce a TV minimization approach for solving the inverse problem of phase retrieval in propagation-based X-ray PCI based on various linear models. Any implementation of TV minimization can be chosen from a wide range of algorithms [63]. Here we will present only results acquired with an algorithm based on the so called Fast Iterative Shrinkage-Thresholding Algorithm (FISTA) [109]. The original implementation of the algorithm was modified to include frequency weighting into the minimization scheme. Frequency weighting permits to account for the frequency-dependent nature of the signal-to-noise ratio and is shown to have a significant influence on the accuracy of the phase retrieval.

4.2 Materials and methods

In the following subsections we will describe how the phase retrieval problem of phase retrieval can be solved using iterative least-squares minimization and TV-minimization. In order to do so, we will introduce a matrix formalism which is uncommon in the field of phase retrieval. To keep our description compact we will refer the reader to the paper of M. Langer [51] for details regarding the theoretical background of X-ray phase retrieval algorithms.

4.2.1 Matrix formalism for phase propagation model

It is essential for the purpose of this paper that the convolution integral can be expressed using matrix formalism. Let us, for instance, define the propagated X-ray wavefront as a matrix product. Let $\mathcal{A}$ denote the set of square integrable functions $\mathbb{R}^2 \to \mathbb{C}$ with bounded support. Within the paraxial approximation, the X-ray field $H_D \in \mathcal{A}$ propagated to a distance D from the object can be expressed as the convolution $(\star)$ of the unpropagated field $T \in \mathcal{A}$ with the Fresnel propagator $P_D \in \mathcal{A}$:

$$H_D = P_D \star T. \tag{4.1}$$

If we denote the Fourier domain representations of T, P_D, and H_D by $\tilde{T}$, $\tilde{P}_D$, and $\tilde{H}_D$, respectively, we find that

$$\tilde{H}_D(f) = \tilde{P}_D(f) \cdot \tilde{T}(f), \tag{4.2}$$

where f denotes the spatial frequency. We now discretize the Fourier domain, representing a spectrum by its values in a discrete set $\{f_1, \ldots, f_k\}$ of basis elements

$$\tilde{\mathbf{t}} = \begin{pmatrix} \tilde{T}(f_1) \\ \vdots \\ \tilde{T}(f_k) \end{pmatrix} \quad \text{and} \quad \tilde{\mathbf{P}}_D = \begin{pmatrix} \tilde{P}_D(f_1) & & & \emptyset \\ & \tilde{P}_D(f_2) & & \\ & & \ddots & \\ \emptyset & & & \tilde{P}_D(f_k) \end{pmatrix}. \tag{4.3}$$

where $\tilde{\mathbf{P}}_D$ is a diagonal matrix containing a discrete representation of the propagator $\tilde{P}_D(f_k)$ and $\tilde{\mathbf{t}}$ is a vector that contains a discrete representation of $\tilde{T}(f_k)$. Consequently, a discretized representation $\tilde{\mathbf{h}}_D$ of the propagated field $\tilde{H}_D$ can be defined in frequency domain:

$$\tilde{\mathbf{h}}_D = \tilde{\mathbf{P}}_D \cdot \tilde{\mathbf{t}}, \tag{4.4}$$

where the symbol $(\cdot)$ denotes the matrix-vector product. If we introduce a vector $\mathbf{t}$ corresponding to the discrete representation of the unpropagated field T, it is possible to construct a *Toeplitz* matrix $\mathbf{P}_D$ such that the discretized propagated field $\mathbf{h}_D$ can be expressed in the spatial domain:

$$\mathbf{h}_D = \mathbf{P}_D \cdot \mathbf{t}, \tag{4.5}$$

As matrix $\mathbf{P}_D$ is dense, it is hard to compute Equation 4.5 directly or solve the inverse problem for a large vector $\mathbf{t}$ in the spatial domain. However, the fact that matrix $\mathbf{P}_D$ has a complimentary frequency space representation $\tilde{\mathbf{P}}_D$, both play an important role in computing the explicit deconvolution and iterative least-squares inversion. Since $\tilde{\mathbf{P}}_D$ is a diagonal matrix, its eigenvalues correspond to the discrete representation of the propagator $P_D(f_k)$. That property allows us to construct the well-known explicit deconvolution Equation 4.8 in subsection 4.2.2 and to analyse the properties of iterative least-squares inversion in subsection 4.2.3.

4.2.2 Linear phase retrieval algorithms: L2-norm regularization

The standard approach to phase retrieval in in-line x-ray PCI relies on the fact that the observed phase-contrast image can be approximated by a linear transformation acting on some unknown image (or a combination of a phase and an attenuation image). This problem can be viewed as a system of linear equations:

$$\mathbf{b} = \mathbf{A} \cdot \mathbf{x}, \tag{4.6}$$

where $\mathbf{A}$ is a matrix that represents one of the linear phase models, $\mathbf{b}$ a vector containing the observed phase-contrast images, and $\mathbf{x}$ a vector containing the unknown images. Since the observed images are corrupted by noise and inversion of $\mathbf{A}$ is usually ill-posed, Equation 4.6 is often replaced by an L2-norm regularized least-squares problem (a.k.a. a Tikhonov regularization problem):

$$\underset{\mathbf{x}}{argmin} : \|\mathbf{A} \cdot \mathbf{x} - \mathbf{b}\|_2^2 + \varepsilon_{L2} \|\mathbf{x}\|_2^2 , \tag{4.7}$$

where $\|...\|_2^2$ denotes the L2-norm and ε the regularization weight. The minimization of the first term guarantees the best fit of the linear phase-contrast model to the observed images, while the second term promotes solutions with the smallest L2-norm thereby suppressing noise and outliers. Given that matrix $\mathbf{A}$ has a diagonal representation in frequency domain $\tilde{\mathbf{A}}$, Equation 4.7 has an analytical solution according to which each jth frequency component $\tilde{\mathbf{x}}_j$ can be calculated using the following expression:

$$\tilde{\mathbf{x}}_j = \frac{\tilde{\mathbf{A}}_{j,j}^* \tilde{\mathbf{b}}_j}{|\tilde{\mathbf{A}}_{j,j}|^2 + \varepsilon_{L2}}, \tag{4.8}$$

where $\tilde{\mathbf{A}}_{j,j}^*$ and $|\tilde{\mathbf{A}}_{j,j}|^2$ are respectively the conjugate and the squared magnitude of the diagonal matrix $\tilde{\mathbf{A}}$. When in underdetermined or ill-conditioned system $|\tilde{\mathbf{A}}_{j,j}| \to 0$, the corresponding frequency component of $\tilde{\mathbf{x}}$ will be suppressed by L2 regularization:

$$\tilde{\mathbf{x}}_j \approx \frac{\tilde{\mathbf{A}}_{j,j}^* \tilde{\mathbf{b}}_j}{\varepsilon_{L2}}. \tag{4.9}$$

4.2.3 Linear phase retrieval algorithms: TV minimization

Similar to the L2-regularized approach (see Equation 4.6), Equation 4.7 can be replaced by a TV-regularized version:

$$\underset{\mathbf{x}}{argmin} : \|\mathbf{A} \cdot \mathbf{x} - \mathbf{b}\|_2^2 + \varepsilon_{TV} \|\mathbf{x}\|_{TV} , \tag{4.10}$$

where the second term $\|\mathbf{x}\|_{TV}$ denotes the so called Total Variation norm of $\mathbf{x}$ which is defined by the gradient magnitude of the image $\mathbf{x}$

$$\|\mathbf{x}\|_{TV} = \sum \sqrt{(\nabla_h \mathbf{x})^2 + (\nabla_v \mathbf{x})^2}, \tag{4.11}$$

where ∇_h and ∇_v are the horizontal and vertical finite difference operators. It has to be noted that the TV norm defined by Equation 4.11 has the dimension of $1/length$ (assuming $\mathbf{x}$ dimensionless), so ε_{TV} has the dimension of $length$ unlike the dimensionless ε_{L2}. Therefore the ratio between the optimal ε_{TV} and ε_{L2} will in general depend on the choice of the pixel size. All values of ε_{TV} given in this article implicitly have the dimension of the *pixel size* that is used in the calculation.

In contrast with the L2-regularized Equation 4.7 the second term of Equation 4.10 promotes solutions with sparse gradient magnitude. Equation 4.10 represents a non-smooth convex minimization problem and can be calculated numerically using one of the iterative TV minimization algorithms [63]. During this study we used an implementation of TV minimization based on FISTA [109] which was introduced by Beck and Teboulle in [110].

The Beck and Teboulle algorithm can be viewed as an extension of dual gradient minimization [108]. Minimizing Equation 4.10 is achieved by splitting each iteration into two sub-problems (or steps), the so called *gradient step* and *denoising step*:

1. *Gradient step*: finding an image $\mathbf{x}_0$ by reducing the unregularized L2 residual term $\|\mathbf{A} \cdot \mathbf{x} - \mathbf{b}\|_2^2$ in the beginning of each iteration,

2. *Denoising step*: followed by regularizing this intermediate image $\mathbf{x}_0$ by minimizing:

$$\underset{\mathbf{x}}{argmin} : \|\mathbf{x}_0 - \mathbf{x}\|_2^2 + \varepsilon_{TV} \|\mathbf{x}\|_{TV} . \tag{4.12}$$

Alternating gradient and denoising steps has been shown previously to speed up the

convergence without sacrificing accuracy [111].

The *gradient step* is based on FISTA where, in order to reach a high rate of convergence, the current guess is updated using information from two previous iterations:

$$1: \quad \mathbf{y}^{n-1} = \mathbf{x}^{n-1} + \left(\frac{t_{n-1}-1}{t_n}\right)\left(\mathbf{x}^{n-1} - \mathbf{x}^{n-2}\right);$$

$$2: \quad \mathbf{y}^n = \mathbf{y}^{n-1} - \frac{2}{L}\mathbf{A}^T \cdot \left(\mathbf{A} \cdot \mathbf{y}^{n-1} - \mathbf{b}\right); \tag{4.13}$$

$$3: \quad \mathbf{x}^n = D_{L,\varepsilon}\left(\mathbf{y}^n\right).$$

Here an intermediate vector $\mathbf{y}$ is introduced to take into account solution updates from two previous iterations, t_n is a scalar that is determined at each iteration as $t_n = \frac{1+\sqrt{1+4t_{n-1}^2}}{2}$, $t_0 = 1$, and L denotes a so called Lipschitz constant that can be calculated as the maximum eigenvalue of the product $\mathbf{A}^* \cdot \mathbf{A}$ (see [109] for a detailed description). Operator $D_{L,\varepsilon}$ signifies the *denoising step* which can be implemented using Fast Gradient Projection (FGP) [61]. During the denoising step, the TV norm of the current guess is minimized depending on the regularization weight ε_{TV} and the Lipschitz constant L.

If matrix $\tilde{\mathbf{A}}$ is diagonal, all frequency components of the solution $\tilde{\mathbf{y}}_j^n$ can be updated during the gradient step (Equation 4.13) independently from each other:

$$\tilde{\mathbf{y}}_j^n = \tilde{\mathbf{y}}_j^{n-1} - \frac{2\omega_j}{L}\tilde{\mathbf{A}}_{j,j}^*\left(\tilde{\mathbf{A}}_{j,j}\tilde{\mathbf{y}}_j^{n-1} - \tilde{\mathbf{b}}_j\right). \tag{4.14}$$

A frequency weighting vector $\omega_j \leq 1$ is introduced to control the convergence of the algorithm.

In general, convergence properties might vary among different minimization algorithms. However, the following observation is likely to be correct for algorithms similar to the one described above: frequency components of the solution $\tilde{\mathbf{x}}_j$ that correspond to small matrix elements $|\tilde{\mathbf{A}}_{j,j}| \to 0$ will only be modified in the denoising step. Hence, its final value is determined solely by the TV-term of Equation 4.10. The latter ensures a significant difference between how TV minimization and L2 regularization (see subsection 4.2.4) are computing the frequency components of the solution that can not be retrieved from the observations.

4.2.4 Linear phase retrieval algorithms: models

As was explained in the previous section, TV minimization can be used for phase retrieval as long as the phase-contrast model can be expressed as a linear system Equation 4.6.

Let us introduce matrices $\mathbf{C}_D$ and $\mathbf{S}_D$ that represent the convolution with the real and imaginary parts of the Fresnel propagator P_D respectively. Their frequency domain representations have the following form:

$$\tilde{\mathbf{C}}_D = \begin{pmatrix} \cos(\alpha_1) & & \emptyset \\ & \ddots & \\ \emptyset & & \cos(\alpha_k) \end{pmatrix}, \tilde{\mathbf{S}}_D = \begin{pmatrix} \sin(\alpha_1) & & \emptyset \\ & \ddots & \\ \emptyset & & \sin(\alpha_k) \end{pmatrix} \quad (4.15)$$

where $\alpha_j = \pi\lambda D|f_j|^2$, λ stands for the X-ray wavelength and D is the effective propagation distance. Using matrices $\mathbf{C}_D$ and $\mathbf{S}_D$ we can construct matrix $\mathbf{A}$ and the corresponding update rule for the gradient step for the following linear phase retrieval models:

CTF model. The CTF model is widely used for phase retrieval in cases when the specimen yields negligible attenuation and slowly varying phase [47]. The Fourier transform of the phase-contrast image $\tilde{I}_D(f)$ is approximated by the Fourier transforms $\tilde{\mu}(f)$ and $\tilde{\varphi}(f)$ of the projected attenuation and projected phase images of the specimen:

$$\tilde{I}_D(f) = \delta(f) - 2\cos(\alpha)\tilde{\mu}(f) + 2\sin(\alpha)\tilde{\varphi}(f). \quad (4.16)$$

Linear systems that are formed by combining Equation 4.16 for a set of m phase-contrast images $\{I_{D(1)}, ..., I_{D(m)}\}$ can easily be represented in matrix form Equation 4.6 (in frequency domain for $|f_j| > 0$) by construction of $\tilde{\mathbf{A}}$, $\tilde{\mathbf{x}}$ and $\tilde{\mathbf{b}}$:

$$\tilde{\mathbf{A}} = \begin{pmatrix} -2\tilde{\mathbf{C}}_{D(1)} & 2\tilde{\mathbf{S}}_{D(1)} \\ & ... & \\ -2\tilde{\mathbf{C}}_{D(m)} & 2\tilde{\mathbf{S}}_{D(m)} \end{pmatrix}, \quad \tilde{\mathbf{x}} = \begin{pmatrix} \tilde{\mu} \\ \tilde{\varphi} \end{pmatrix}, \quad \tilde{\mathbf{b}} = \begin{pmatrix} \tilde{\mathbf{I}}_{D(1)} \\ ... \\ \tilde{\mathbf{I}}_{D(m)} \end{pmatrix}. \quad (4.17)$$

Here the unknown vectors $\tilde{\mu}$ and $\tilde{\varphi}$ are concatenated into a single vector $\tilde{\mathbf{x}}$, vector $\tilde{\mathbf{b}}$ contains all observed images $\tilde{\mathbf{I}}_{D(i)}$ and matrix $\tilde{\mathbf{A}}$ is obtained by concatenating pairs of

matrices $\tilde{\mathbf{C}}_{D(i)}$ and $\tilde{\mathbf{S}}_{D(i)}$, where each pair corresponds to a particular propagation distance $D(i)$. Using this representation we can find an update rule similar to Equation 4.14 for each jth frequency component of the unknown vector $\tilde{\mathbf{x}}$. We will separate it into the update rules for $\tilde{\mu}$ and $\tilde{\varphi}$ as follows:

$$\tilde{\mu}_j^n = \tilde{\mu}_j^{n-1} + \frac{4\omega_{\mathbf{j}}}{Lm} \sum_{i=1}^m \tilde{\mathbf{C}}_{D(i)}^{(j,j)} \left(-2\tilde{\mathbf{C}}_{D(i)}^{(j,j)} \tilde{\mu}_j^{n-1} + 2\tilde{\mathbf{S}}_{D(i)}^{(j,j)} \tilde{\varphi}_j^{n-1} - \tilde{\mathbf{I}}_{D(i)}^j \right),$$

$$\tilde{\varphi}_j^n = \tilde{\varphi}_j^{n-1} - \frac{4\omega_{\mathbf{j}}}{Lm} \sum_{i=1}^m \tilde{\mathbf{S}}_{D(i)}^{(j,j)} \left(-2\tilde{\mathbf{C}}_{D(i)}^{(j,j)} \tilde{\mu}_j^{n-1} + 2\tilde{\mathbf{S}}_{D(i)}^{(j,j)} \tilde{\varphi}_j^{n-1} - \tilde{\mathbf{I}}_{D(i)}^j \right).$$

$$(4.18)$$

Calculation of Equation 4.18 has to be carried out at each iteration of the gradient and denoising steps. Since the denoising step must be computed in the spatial domain, two inverse Fourier transforms (for $\tilde{\mu}$ and $\tilde{\varphi}$) must be calculated at each iteration before the denoising step and two Fourier transforms after the denoising step.

Mixed model. The Mixed model [49] is used for phase retrieval in cases with (significant) attenuation. In an approximated version of this model (assuming only the first two terms), the phase-contrast image $\tilde{I}_D(f)$ becomes:

$$\tilde{I}_D(f) = \cos(\alpha)\tilde{I}_0(f) + 2\sin(\alpha)(\tilde{I_0\varphi})(f). \tag{4.19}$$

Here $\tilde{I}_0(f)$ denotes the Fourier transform of the intensity image at zero distance. $\tilde{I}_0(f)$ is fully determined by the attenuation image of the specimen and can be expressed in the spatial domain as $I_0 = e^{-2\mu}$. The linear system that describes a set of phase-contrast images $\{\tilde{I}_{D(1)}, ..., \tilde{I}_{D(m)}\}$ based on Equation 4.19 can be expressed through the following $\tilde{\mathbf{A}}$, $\tilde{\mathbf{x}}$ and $\tilde{\mathbf{b}}$:

$$\mathbf{A} = \begin{pmatrix} \tilde{\mathbf{C}}_{D(1)} & 2\tilde{\mathbf{S}}_{D(1)} \\ & ... & \\ \tilde{\mathbf{C}}_{D(m)} & 2\tilde{\mathbf{S}}_{D(m)} \end{pmatrix}, \quad \tilde{\mathbf{x}} = \begin{pmatrix} \tilde{\mathbf{I}}_0 \\ (\tilde{\mathbf{I}_0\varphi}) \end{pmatrix}, \quad \tilde{\mathbf{b}} = \begin{pmatrix} \tilde{\mathbf{I}}_{D(1)} \\ ... \\ \tilde{\mathbf{I}}_{D(m)} \end{pmatrix}. \tag{4.20}$$

Here we treat the element-wise product of the intensity image and the phase image $(\mathbf{I}_0\varphi)$ as an unknown image independent from the unknown intensity image $\mathbf{I}_0$. Using this representation we can write down the update rule Equation 4.14 for the gradient
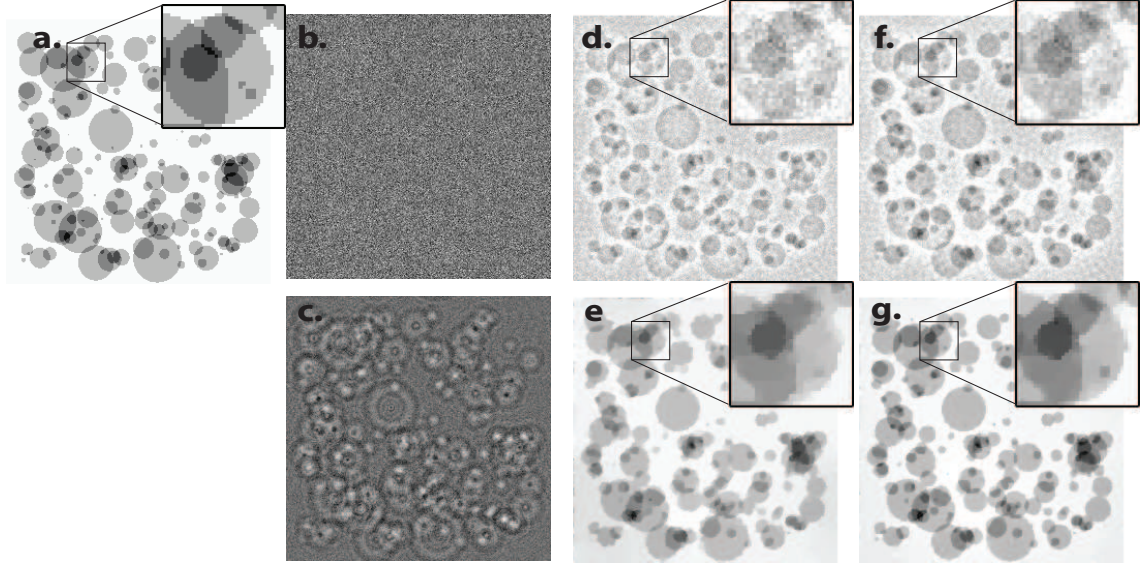
Figure 4.1: Phase reconstructions based on the simulated data of the 'flat' phantom for TV and L2 regularization with and without frequency weighting (see Sec. subsection 4.3.1 for simulation parameters). (a) Ground truth. (b) Intensity image at zero distance with Gaussian noise. (c) Propagated phase-contrast image at 1m with Gaussian noise. (d) L2-regularized solution, no frequency weighting. (e) TV-regularized solution, no frequency weighting. (f) L2-regularized solution, with frequency weighting. (g) TV-regularized solution with frequency weighting.

step as:

$$\tilde{\mathbf{I}}_{0,j}^{n} = \tilde{\mathbf{I}}_{0,j}^{n-1} - \frac{2\omega_j}{Lm} \sum_{i=1}^{m} \tilde{\mathbf{C}}_{D(i)}^{(j,j)} \left(\tilde{\mathbf{C}}_{D(i)}^{(j,j)} \tilde{\mathbf{I}}_{0,j}^{n-1} + 2\tilde{\mathbf{S}}_{D(i)}^{(j,j)} (\tilde{\mathbf{I}_0\varphi})_{j}^{n-1} - \tilde{\mathbf{I}}_{D(i)}^{j} \right)$$

$$(\tilde{\mathbf{I}_0\varphi})_{j}^{n} = (\tilde{\mathbf{I}_0\varphi})_{j}^{n-1} - \frac{4\omega_j}{Lm} \sum_{i=1}^{m} \tilde{\mathbf{S}}_{D(i)}^{(j,j)} \left(\tilde{\mathbf{C}}_{D(i)}^{(j,j)} \mathbf{I}_{0,j}^{n-1} + 2\tilde{\mathbf{S}}_{D(i)}^{(j,j)} (\tilde{\mathbf{I}_0\varphi})_{j}^{n-1} - \tilde{\mathbf{I}}_{D(i)}^{j} \right).$$

(4.21)

Phase-attenuation duality models. These models can be used when the specimen has a homogeneous composition or, in the limited range of X-ray energies, when the specimen is composed of light elements [52, 54]. In duality models the phase and attenuation images of a specimen are assumed to be proportional to each other, i.e. $\sigma = \frac{\varphi}{\mu}$, permitting to reduce the number of unknown variables. In this study we consider two duality models:

$$\tilde{I}_D(f) = 2\left(\sigma \sin(\alpha) - \cos(\alpha)\right) \tilde{\mu}(f), \tag{4.22}$$

which was derived from the CTF model [53] and :

$$\tilde{I}_D(f) = (\cos(\alpha) + (\alpha - \sigma)\sin(\alpha))\,\tilde{I}_0(f), \tag{4.23}$$

which was derived from the Mixed model [54]. Both models can be used to retrieve the projected attenuation image of the specimen based on a single phase contrast image $\tilde{I}_D(f)$ acquired at a suitable distance $D > 0$ as well as using a set of m phase-contrast images $\{\tilde{I}_{D(1)}, ..., \tilde{I}_{D(m)}\}$ recorded at different distances. The update rule for the gradient step based on Equation 4.22 is then simplified into:

$$\tilde{\mu}_j^n = \tilde{\mu}_j^{n-1} - \frac{4\omega_j}{Lm} \sum_{i=1}^{m} \tilde{\mathbf{B}}_i \left(2\tilde{\mathbf{B}}_i \tilde{\mu}_j^{n-1} - \tilde{\mathbf{I}}_{D(i)}^j \right), \tag{4.24}$$

where $\tilde{\mathbf{B}}_i = (\sigma \tilde{\mathbf{S}}_{D(i)}^{(j,j)} - \tilde{\mathbf{C}}_{D(i)}^{(j,j)})$. The update rule for the gradient step based on Equation 4.23 has the following form:

$$\tilde{\mathbf{I}}_{0,j}^n = \tilde{\mathbf{I}}_{0,j}^{n-1} - \frac{2\omega_j}{Lm} \sum_{i=1}^{m} \tilde{\mathbf{B}}_i \left(\tilde{\mathbf{B}}_i \tilde{\mathbf{I}}_{0,j}^{n-1} - \tilde{\mathbf{I}}_{D(i)}^j \right), \tag{4.25}$$

where $\tilde{\mathbf{B}}_i = (\tilde{\mathbf{C}}_{D(i)}^{(j,j)} + (\alpha - \sigma)\tilde{\mathbf{S}}_{D(i)}^{(j,j)})$.

4.3 Simulations

As indicated before, TV minimization permit an accurate solution for a class of inverse problems based on severely incomplete sets of observations. The underlying assumption of all TV minimization approaches is that the unknown signal must have a sparse gradient magnitude. In the field of image reconstruction such assumption is fulfilled when the reconstructed image is piecewise constant, i.e. the intensity only changes in a step-like manner.

4.3.1 Phantom image with sparse gradient magnitude

Our first demonstration of phase retrieval based on TV minimization uses a 'flat' piece-wise constant phantom. Here TV minimization is expected to yield high accuracy. However, in the following subsections we will abandon this restriction and use a 'spheres' phantom to demonstrate the performance of TV minimization in more
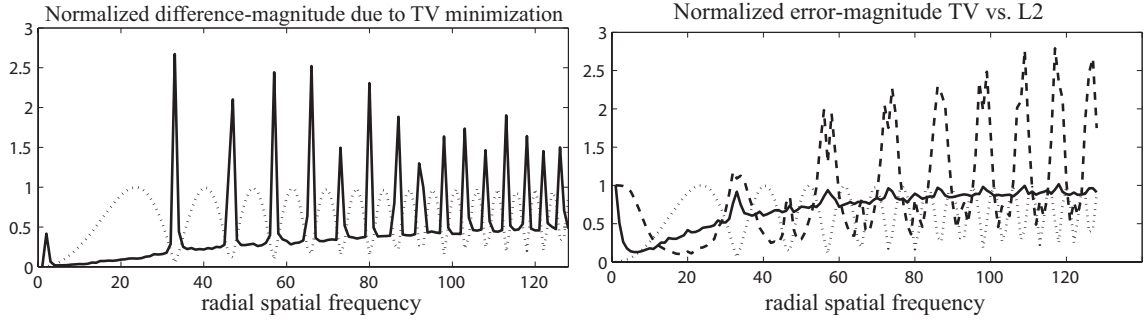
Figure 4.2: The radial frequency spectrum (angular averaged) of the reconstruction. Dotted line shows $|\tilde{\mathbf{A}}_{j,j}|$ on both graphs. *Left*: normalized difference between the solutions with and without TV-regularization, i.e. $(\varepsilon_{TV} = 0.02)$ vs. $(\varepsilon_{TV} = 0)$. *Right*: normalized error-magnitude of the TV-regularized solution (solid line) and the L2-regularized solution (dashed line). The graphs are normalized against the radial frequency spectrum of the ground truth image.

realistic cases.

Figure 4.1 shows the comparison between L2-regularized and TV-regularized phase retrieval for the CTF model. The ground truth projected attenuation and phase images (256×256 pixels) were computed for a randomly generated composition of overlapping polyethylene disks immersed in a layer of water with a total thickness $d = 0.1$ mm (Figure 4.1(a)). Subsequently phase-contrast images I_{D_1} and I_{D_2} are generated using Fresnel propagation for a monochromatic X-ray energy of $20KeV$ and a pixel size of 1 μm (Figure 4.1(b, c)). In the current simulation we used propagation distances {0 m, 1 m}. Gaussian noise with standard deviation of 0.02 was added to both images mimicking acquisition with poor SNR. The optimal regularization parameters ε_{L2} and ε_{TV} were chosen such that the overall Root Mean Square Error (RMSE) is minimal for the listed conditions (see subsection 4.3.3). In practice, they must be derived from an estimate of the SNR of the measured images. No stopping criteria was used in the gradient step of the TV minimization, instead all reconstructions were computed using 1000 iterations in order to guarantee convergence.

The resulting solutions are shown in Figure 4.1(d, e). The *frequency spectrum* (we will use this term for the angular average of the magnitude of 2D Fourier transform of the image) of the error magnitude of the solutions can be seen on Figure 4.2 (*right*). The frequency spectrum of the error was normalized against the frequency spectrum of the ground truth image. It is evident from this graph that when the optimal regularization weights are used, TV regularization is significantly more ac-

curate then L2 regularization at all frequencies where the direct phase retrieval problem is undetermined (for frequencies components with $|\tilde{\mathbf{A}}_{j,j}| \to 0$). Note that TV minimization can yield higher error within particular bands of frequencies to promote a sparse gradient. We have already pointed out in subsection 4.2.2 and Section subsection 4.2.3 that there are major differences in how TV minimization treats frequency components of the solution that correspond to $|\tilde{\mathbf{A}}_{j,j}| \to 0$. In order to confirm this, we compared the results of the TV method with $\varepsilon_{TV} = 0.02$ and $\varepsilon_{TV} = 0$ (no TV minimization) when applied to noise-free data. Figure 4.2(*left*) shows that the frequency spectrum of the normalized difference between the regularized and non-regularized solutions. It is evident that the regularization strength depends heavily on $|\tilde{\mathbf{A}}_{j,j}|$.

So far we used scalar regularization weights ε_{L2} and ε_{TV} in both regularization approaches. One can achieve a significantly improved accuracy by using a frequency dependent regularization weighting instead. In L2 regularization, the scalar ε_{L2} can be replaced by the frequency dependent factor $\varepsilon_{L2,j} \sim SNR^{-1}(f_j)$ (i.e. Wiener deconvolution). In our investigation we assumed the SNR of the reconstructed image to be proportional to its frequency spectrum. The latter can be estimated from a preliminary reconstruction based on a scalar regularization weight using either L2 or TV regularization. Such estimation is demonstrated in Figure 4.3(*left*). The estimate of the image SNR was introduced into TV minimization approach using the frequency weighting vector $\omega_j \sim SNR(f_j)$ in Equation 4.14. Resulting L2- and TV-regularized solutions are depicted in Figure 4.1(f) and Figure 4.1(g) respectively. It can be seen in Figure 4.3(*right*) that the error of TV-regularized solution is significantly lower than the error of L2-regularized solution in a wide frequency range.

4.3.2 Realistic phantom

In order to demonstrate the performance of the TV-minimization in realistic cases we tested L2-regularization and TV-minimization phase retrieval approaches for phantoms with a non-sparse gradient. Figure 4.4 shows reconstructions of the projected phase image of a composition of randomly sized and positioned polyethylene spheres immersed in water (the rest of simulation parameters match those from subsection 4.3.1). Reconstructed images are obtained using both L2- and TV-regularization based on the CTF model, the Mixed model as well as their phase-
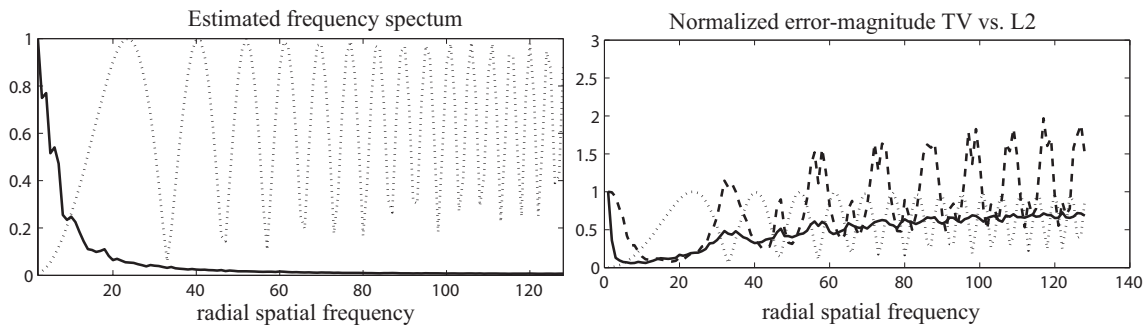
Figure 4.3: Radial frequency spectrum (angular averaged) of the retrieval results using the frequency dependent regularization weights (i.e. frequency weighting). Dotted line shows $|\tilde{\mathbf{A}}_{j,j}|$ on both graphs. *Left*: estimated frequency spectrum of the specimen (solid line). *Right*: normalized error-magnitude of the TV-regularized solution (solid line) and L2-regularized solution (dashed line) with frequency weighting.

attenuation duality modifications. In phase retrieval based on duality models we have used a single simulated phase-contrast image with propagation distance 1 m. The corresponding normalized frequency spectra of the error-magnitude are depicted in Figure 4.5. It is evident that the TV-regularized solutions yield lower error in comparison with the L2-regularized ones in a broad range of frequencies. It is also apparent that given the parameters used in the current simulation (low attenuation and moderate phase changes), reconstructions obtained with the CTF model and the Mixed model are virtually indistinguishable, while there is some discrepancy with the models that are based on phase-attenuation duality assumption.

4.3.3 Optimal regularization weights

The accuracy of both regularization methods considered in this paper strongly depend on the choice of the regularization weights ε_{L2} and ε_{TV}. In practice, these parameters are estimated from the measured data or chosen in some heuristic manner. In order to investigate how the choice of the regularization weight affects the accuracy of phase retrieval, we measured the total RMSE of the reconstructed phase images varying two parameters: standard deviation (STD) of the Gaussian noise and the regularization weight of the phase retrieval algorithm. The phase-contrast images were simulated using the polyethylene spheres phantom using the simulation parameters described in subsection 4.3.1 and subsection 4.3.2. Figure 4.6(*left*) shows the values of RMSE for phase retrieval based on the CTF model. Curves
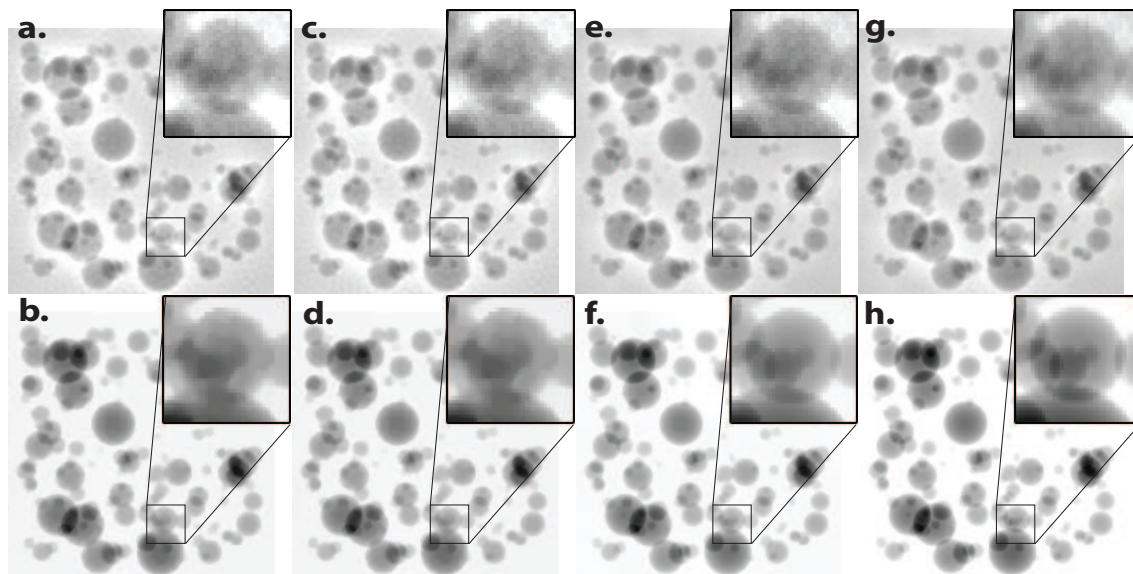
Figure 4.4: Reconstructions based on the simulated data of the 'spheres' phantom for different propagation models. All results are obtained using frequency weighting. Top row of images (a, c, e, g) show L2-regularized solutions. The bottom row of images (b, d, f, h) show TV-regularized solutions. Solutions (a, b) are based on the CTF model, (c, d) on the Mixed model, (e, f) on the dual-CTF model and (g, h) on the dual-Mixed model.

L2-1, L2-2, L2-3 and L2-4 represent the RMSE of the L2-regularized solutions with noise STD $= 0.01, 0.02, 0.05$ and 0.1 respectively. Curves TV-1, TV-2, TV-3 and TV-4 represent the RMSE of the TV-regularized solutions with corresponding noise STD. It can be seen that TV-regularization yields solutions with a 4-7 times lower total RMSE in comparison to those obtained with L2 regularization. It is also evident that estimation of the optimal regularization parameter is more important for TV-regularization then for L2 regularization as it affects the RMSE to a larger extent.

Along with various types of additive noise, non-linear effects that are not taken into account by the phase retrieval models can become an important source of errors. The fraction of signal to error due to non-linearity of the CTF model is, in a certain range of conditions, proportional to $|\sin(\alpha)|$[56]. That property allows to treat the non-linearity error as another form of noise. Figure 4.6(*right*) demonstrates the values of RMSE of the phase retrieval based on the CTF model applied to noise-free phase-contrast images simulated for phantoms of different thicknesses. Curves L2-1, L2-2, L2-3 and L2-4 show the RMSE of the L2-regularized phase retrieval for phantoms with a total thickness $= 0.1$ mm, 0.25 mm, 0.5 mm and 1 mm respectively.
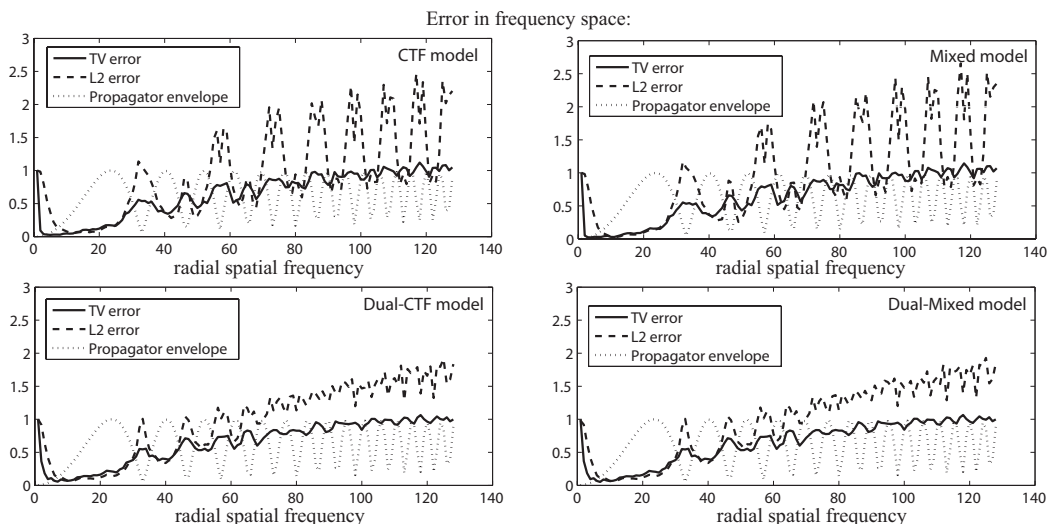
Figure 4.5: The radial frequency spectrum (angular averaged) of the reconstructions for different propagation models. Dotted line shows $|\tilde{\mathbf{A}}_{j,j}|$ on all graphs. Normalized error magnitude of the TV-regularized solution (solid line) and L2-regularized solution (dashed line).

Curves TV-1, TV-2, TV-3 and TV-4 represent the RMSE of the corresponding TV-regularized solutions. The thickness of the phantom has a dramatic effect on the accuracy of the phase retrieval based on the CTF model since it introduces larger variations in projected attenuation and phase images which leads to greater non-linearity of the observed phase-contrast image. It is evident that TV-regularized phase retrieval yields similar accuracy with the L2-regularized solution in the case of thin phantom. However the advantage of TV regularization becomes significant for thicker phantoms.

4.4 Experiment

To test the TV-regularized phase retrieval on experimental data we have used X-ray phasecontrast images of a test pattern designed to assess the resolution of the X-ray imaging system. The pattern consisted of 700 nm high lithographic gold structures on top of a Si substrate. Phase-contrast data was acquired at the beamline ID22NI of the European Synchrotron Radiation Facility (Grenoble, France). The incoming x-rays were focused using Kirkpatrick-Baez mirror system, which gave a point focus with sub 100 nm with and height (FWHM) [112]. The mean energy of the x-rays was 17.5 KeV ($\sim 1.5\%$ bandwidth) with 10^{12} photons/s in the focus. The focus was
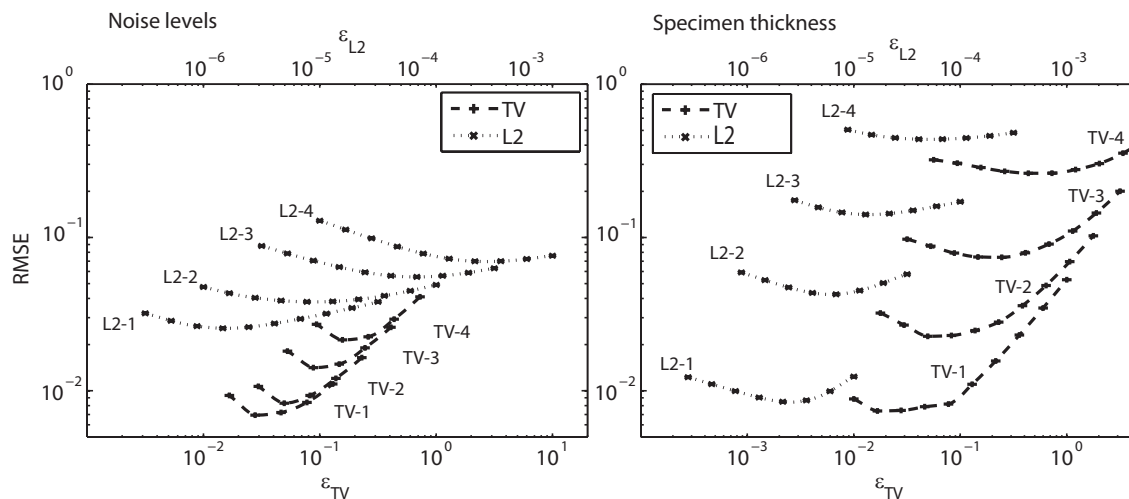
Figure 4.6: Influence of the regularization weight on samples with increasing noise levels and on samples of increasing thickness. RMSE of the solution is shown against the magnitude of regularization parameter for L2 regularization (crosses) against TV regularization (plus signs). *Left*: each curve shows errors for different noise levels, STD = 0.01, 0.02, 0.05, 0.1. *Right*: each curve shows errors for different specimen thickness, 0.1 mm, 0.2 mm, 0.5 mm, 1 mm.

used as a point source for projection microscopy [113] giving effective pixel size of 53 nm. Images were acquired at four propagation distances {27.4 mm, 28.3 mm, 31.8 mm, 40.3 mm}.

Figure 4.7 shows reconstructed phase images of the *lines and dots* pattern and so called *Siemens star* pattern. The L2-regularized solutions are shown in the top row, while the bottom row shows the TV-regularized solutions. Both phase-retrieval approaches were based on phase-attenuation duality CTF model. The reconstructions depicted in sub-figures (a, b, e and f) are based on phase-contrast images acquired at four different distances. The reconstructions from sub-figures (c, d, g and h) are based on a single phase-contrast image acquired at a propagation distance 27.4 mm.

It is evident that TV regularization permits a very high quality reconstruction of *lines and dots* pattern based only on a single phase-contrast image. The high frequency ripple-like artifacts are efficiently suppressed while the pattern is accurately reconstructed. That can be explained by the fact that the reconstructed image has a sparse gradient magnitude and that spatially localized structures such as dots and lines have a broad footprint in frequency space. The problem of phase retrieval based on a single phase-contrast image is ill-posed within a set of spatial frequencies that depends on the acquisition parameters. TV regularization allows to fill-in these gaps

in frequency space by applying the constraint of sparse gradient magnitude. Phase retrieval of the *Siemens star* pattern shows that the structures which are periodic in space are harder to reconstruct. Their footprint in frequency space is localized and might be completely irrecoverable from a single phase-contrast image with the given acquisition parameters.
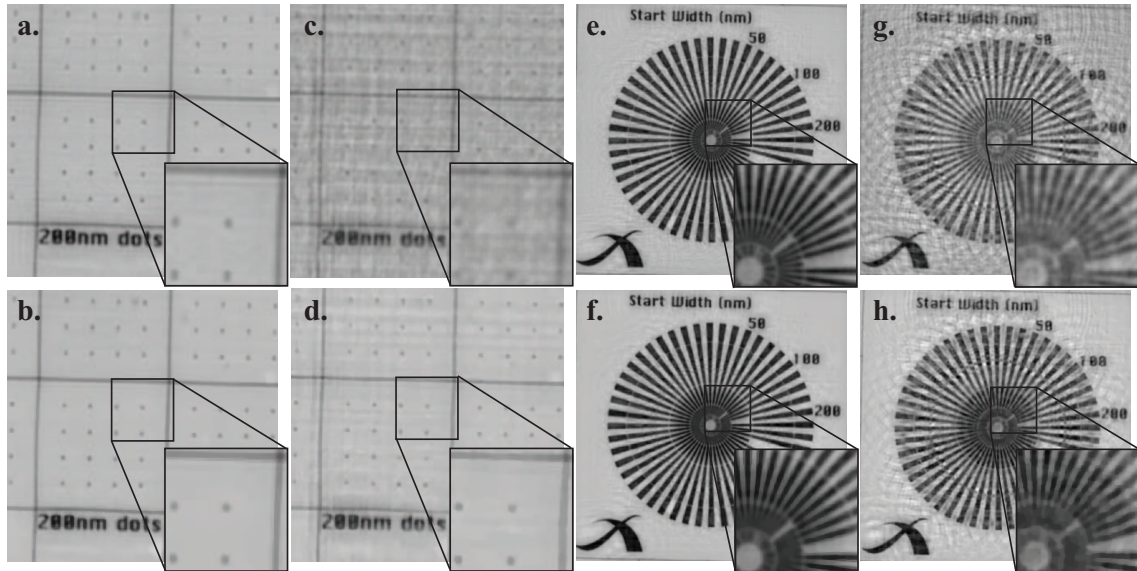

Figure 4.7: Phase retrieval from experimental data using the dual-CTF model. (a-d) Phase retrieval of a 'dots and lines' pattern. (e-h) Phase retrieval of a 'star' pattern. (a, e) L2-regularized solution based on 4 images recorded at different propagation distances. (b, f) TV-regularized solution based on 4 images recorded at different propagation distances. (c, g) L2-regularized solution based on a single recorded image. (d, h) TV-regularized solution based on a single recorded image.

4.5 Conclusion

Phase retrieval in propagation based X-ray PCI can be improved using iterative TV minimization algorithms. Reconstructions based on simulated and experimental data show that phase retrieval based on TV minimization can significantly outperform the current practice, a deconvolution approach with L2 regularization. TV minimization can be used with different linear phase retrieval models including the CTF model, the Mixed model and the phase-attenuation duality models. Although the method works best for specimen that adhere to the constraints, the method also improves the phase reconstruction for specimen that are not exactly sparse in their

gradient magnitude. TV minimization provides an effective regularization instrument for solving an underdetermined linear systems of equations. Analysis of the Fourier spectrum of the error of the reconstructed phase images clearly demonstrates that TV minimization allows partial recovery of the solution within the frequency bands that are undefined by the particular phase-contrast model or corrupted by noise. That feature of TV minimization allows effective suppression of the high frequency artifacts in single-distance phase retrieval based on phase-attenuation duality models and permits more accurate reconstruction of low spatial frequencies in multi-distance approaches.

TV minimization finds the solution in the form of a TV-regularized least-squares fit and it does not require the knowledge of the attenuation part of the specimen. A frequency dependent estimation of the signal-to-noise ratio can be used for each observed image, dramatically improving the accuracy of reconstruction. Simulations show that TV regularization can suppress errors that occur both due to additive noise and due to non-linearity of the phase propagation. Experimental data has shown that TV minimization can also significantly improve the accuracy of phase reconstruction of real specimen that comply with gradient sparsity condition and imaged under realistic circumstances. These results could allow to decrease the number of phase-contrast images that are needed for the accurate image reconstruction in some applications of X-ray PCI. This is particularly important for in situ experiments or to reduce radiation damage to the specimen.

5 Algebraic phase retrieval tomography

Abstract[1]

The reconstruction problem in in-line X-ray Phase-Contrast Tomography is usually approached by solving two independent linearized sub-problems: phase retrieval and tomographic reconstruction. Both problems are often ill-posed and require the use of regularization techniques that lead to artifacts in the reconstructed image. We present a novel reconstruction approach that solves two coupled linear problems algebraically. Our approach is based on the assumption that the frequency space of the tomogram can be divided into bands that are accurately recovered and bands that are undefined by the observations. This results in an underdetermined linear system of equations. We investigate how this system can be solved using three different algebraic reconstruction algorithms based on Total Variation minimization. These algorithms are compared using both simulated and experimental data. Our results demonstrate that in many cases the proposed algebraic algorithms yield a significantly improved accuracy over the conventional L2-regularized closed-form solution. This work demonstrates that algebraic algorithms may become an important tool in applications where the acquisition time and the delivered radiation dose must be minimized.

---

[1]This work is published in: A. Kostenko, K. J. Batenburg, A. King, S. E. Offerman and L. J. van Vliet, "Total variation minimization approach in in-line x-ray phase-contrast tomography," Optics Express, *in press* (2013).

5.1 Introduction

Quantitative X-ray Phase-Contrast Tomography (X-ray PCT) requires three-dimensional image reconstruction from a series of two-dimensional in-line phase-contrast images acquired under various angles. Within the linear approximation, the problem of image reconstruction in X-ray PCT is typically treated as two separate linear sub-problems which are solved sequentially [114]. Namely, the *phase retrieval* problem, where the projected refraction index (i.e. linear phase and attenuation) of the specimen is retrieved independently for each recorded phase-contrast image and the problem of *tomographic reconstruction*, where the three-dimensional distribution of the refraction index is computed from the collection of retrieved projections.

Most often linear phase retrieval of an individual tomographic projection is associated with inversion of an ill-posed linear system. In such cases regularization (e.q. L2 or L1 regularization) permits computation of an approximate inverse solution [97]. However, it will often cause artifacts that are subsequently propagated into the tomographic reconstruction of the object.

We believe that a more accurate reconstruction approach can be designed by combining phase retrieval and tomographic reconstruction into a single underdetermined linear problem. This assumption is based on the fact that tomographic projections of the object are in general not independent from each other. According to the so called Helgason-Ludwig consistency conditions [60], individual projections of the object must be interrelated leading to a certain degree of redundancy within the tomographic data. The theory of Compressed Sensing [65] suggests an even stronger correlation between the individual tomographic projections for objects that have a sparse representation in a certain domain. For sparse solutions, the projection data shows a low rate of innovation, which implies that a limited number of projections suffices for exact reconstruction [115]. These facts lead us to a conclusion that the accuracy of phase retrieval of a single tomographic projection can benefit from the redundancy contained in the complete tomographic dataset. Regularization techniques based on the assumption of sparsity were shown to improve the quality of image reconstruction in cases when the reconstructed image is not strictly sparse [108]. We will demonstrate how such redundancy can be exploited using an iterative algebraic reconstruction approach for in-line X-ray PCT.

5.2 Materials and methods

5.2.1 Single-distance phase retrieval

Let us consider a single-distance phase-retrieval model based on the Contrast Transfer Function (CTF) approach [53]. In this model the projected phase image of the specimen $\phi(s)$ is assumed to be proportional to the projected attenuation image $\mu(s)$. The proportionality ratio $\sigma = \phi/\mu$ can be calculated as the ratio between the real and imaginary parts of the refractive index of the specimen. This allows us to express the Fourier transform of the phase-contrast image $\tilde{I}(w)$ as the Fourier transform of the projected attenuation image $\tilde{\mu}(w)$ multiplied with the CTF that corresponds to the object-to-detector distance D and the X-ray wavelength λ:

$$\tilde{I}(w) = \delta(w) - \Big(2\cos(\pi\lambda Dw^2) - 2\sigma\sin(\pi\lambda Dw^2)\Big)\cdot\tilde{\mu}(w). \tag{5.1}$$

Here w stands for the spatial frequency and $\delta(w)$ denotes the delta function at the origin of spatial frequency coordinates. A parallel monochromatic X-ray beam with a uniform illumination and intensity $I_0 = 1$ was assumed for simplicity. This model is valid for chemically homogeneous or quasi-homogeneous objects (i.e. $\phi/\mu \approx const$) with weak attenuation and slow-varying phase or for objects that are composed from light elements in a limited range of X-ray energies [52, 54]. Obviously, it is impossible to recover the projected attenuation image $\tilde{\mu}(w)$ from the observed phase-contrast image $\tilde{I}(w)$ at frequencies w that correspond to the zero-crossings of the CTF (see Figure 5.1). Also, in the vicinity of each zero-crossing of the CTF the inverse problem based on Equation 5.1 will be ill-posed due to measurement noise in addition to systematic linearization errors. At these frequencies $\tilde{\mu}(w)$ has to be computed using additional constraints that favor a particular solution based on *a-priori* knowledge.

Let us assume that the vectors $\boldsymbol{\mu}$ and $\boldsymbol{I}$ are defined in the spatial domain on a uniform grid of k values that belong to $\mu(s)$ and $(I(s) - 1)$ respectively. A linear operator $\mathcal{F}$ will represent the uniform discrete Fourier transform. Element-wise multiplication with the CTF function is denoted by the linear operator $\mathcal{P}$. Then Equation 5.1 can be discretized in the following form:

$$\mathcal{F}\boldsymbol{I} = \mathcal{P}\mathcal{F}\boldsymbol{\mu}. \tag{5.2}$$

When the matrix notation is considered, $\mathcal{P}$ can be represented by a square $k \times k$ diagonal matrix:

$$\mathcal{P} = \text{diag}(P(w_1), P(w_2), ..., P(w_k)), \tag{5.3}$$

where $P(w) = 2\sigma \sin(\pi \lambda D w^2) - 2\cos(\pi \lambda D w^2)$. A more detailed explanation of the matrix notation is given in our paper on two-dimensional phase retrieval [97]. Now the approximate solution to Equation 5.1 can be found by solving the corresponding least squares problem:

$$\boldsymbol{\mu} = \arg\min_{\mu} \|\mathcal{P}\mathcal{F}\boldsymbol{\mu} - \mathcal{F}\boldsymbol{I}\|_2^2. \tag{5.4}$$

Here $\|...\|_2^2$ represents the L2 norm of the corresponding functional. To avoid amplification of errors by the terms that correspond to small $P(w)$, we will exclude these terms from the system of equations. To do so we assume that the image $\boldsymbol{\mu}$ is irrecoverable within the frequency bands $|w - w_0| < \epsilon$, where w_0 is the nearest zero-crossing of the CTF and ϵ is a small constant that depends on the signal-to-noise ratio. Now an additional linear operator can be introduced:

$$\mathcal{Z} = \text{diag}(Z(w_1), Z(w_2), ..., Z(w_k)). \tag{5.5}$$

Operator $\mathcal{Z}$ can be represented by a binary matrix and is applied to both sides of Equation 5.2, making sure that terms corresponding to the small $P(w)$ are set to zero:

$$\mathcal{Z}\mathcal{F}\boldsymbol{I} = \mathcal{Z}\mathcal{P}\mathcal{F}\boldsymbol{\mu}. \tag{5.6}$$

The system that we have obtained is underdetermined (it does not allow to determine $(\mathcal{F}\boldsymbol{\mu})$ for $|w - w_0| < \epsilon$) and does not have a unique solution unless additional constraints are added. Hofmann [56] proposed to use a simple constraint $(\mathcal{F}\boldsymbol{\mu}) = 0$ for $|w - w_0| < \epsilon$ in order to solve the phase-retrieval problem. However, we expect that applying sparsity constraints to the joint phase-contrast-tomographic reconstruction will yield a better accuracy. A frequency dependent ϵ can be defined when it is possible to estimate the power spectrum of the noise and the power spectrum of the reconstructed image modulated with the CTF *a-priori*. Otherwise a constant factor ϵ can be chosen, for instance, after evaluating the quality of the

direct reconstruction proposed in [56].

5.2.2 Tomography

In this subsection we will use coordinate s to describe the transverse coordinate an observed image of the object and w as its counterpart in the Fourier domain. A new coordinate θ will be introduced for the angle at which the image is recorded during the tomographic acquisition. Coordinates (x, y) will be used to describe a 2D tomographic image of the object (see Figure 5.1).

Consider a two-dimensional image $f(x, y)$ which is defined on $\mathbb{R}^2 \to \mathbb{C}$ as a square integrable function with bounded support. A linear projection of $f(x, y)$ in the direction θ will be defined along the coordinate s as:

$$p(\theta, s) = \int_{-\infty}^{\infty} f(t \sin \theta + s \cos \theta, -t \cos \theta + s \sin \theta) dt. \tag{5.7}$$

According to the *central slice theorem*, if a two-dimensional Fourier transform of the image $f(x, y)$ is computed

$$\tilde{f}(u, v) = \int_{-\infty}^{\infty} \int_{-\infty}^{\infty} f(x, y) \cdot e^{-2\pi i(xu + yv)} dx dy, \tag{5.8}$$

values of $\tilde{f}(u, v)$ that lie on a radial line passing through the center of coordinates under an angle θ (central slice) will correspond to the one-dimensional Fourier transform taken along the s coordinate of the projection $p(\theta, s)$:

$$\tilde{f}(w \cos \theta, w \sin \theta) = \int_{-\infty}^{\infty} p(\theta, s) \cdot e^{-2\pi i s w} ds. \tag{5.9}$$

The central slice theorem demonstrates an important relation between the Radon transform and the Fourier transform of the two-dimensional image $f(x, y)$. It follows from Equation 5.9 that the function $f(x, y)$ can be sampled in 2D Fourier space using 1D Fourier transforms of its own projections $p(\theta, s)$. This facilitates direct reconstruction based on the inverse Fourier transform of $\tilde{f}(u, v)$ which has to be computed using interpolation. Moreover, it was shown in [65] that by using appropriate additional constraints, a piece-wise constant object (i.e. an object that has sparse gradient magnitude) can be accurately reconstructed from a severely
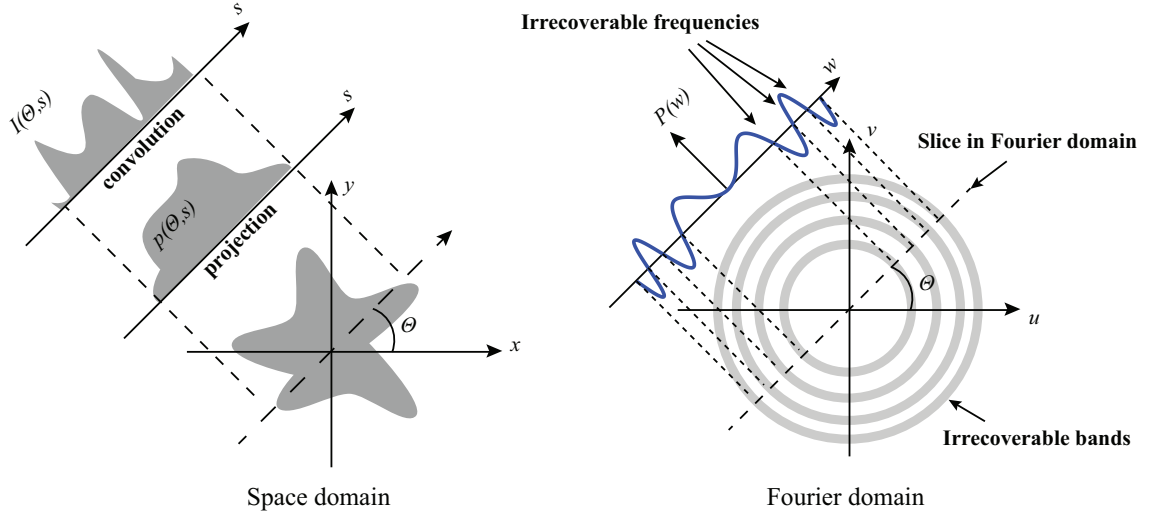
Figure 5.1: Central slice theorem for single-distance X-ray Phase Retrieval Tomography. Spatial domain representation: observations $I(\theta, s)$ can be modeled as the projection of the unknown image $f(x, y)$ followed by the convolution with a linear propagator. Fourier domain representation: Fourier transform of the observed image $\tilde{I}(\theta, w)$ can be modeled as the slice of the unknown image $\tilde{f}(w \cos\theta, w \sin\theta))$ multiplied with $P(w)$. The Fourier representation of the unknown image $f(u, v)$ is irrecoverable at the frequency bands corresponding to zero-crossings of $P(w)$.

undersampled Fourier representation $\tilde{f}(u, v)$, i.e. using very few projections. The latter has important consequences for regularization of the phase-retrieval problem described in the following subsection.

5.2.3 Phase-contrast tomography

By combining Equation 5.1 and Equation 5.9 we can rewrite the central slice theorem for what we call Phase Retrieval Tomography (PRT), i.e. phase retrieval combined with tomographic reconstruction:

$$\tilde{f}(w \cos\theta, w \sin\theta) = \frac{\tilde{I}(\theta, w) - \delta(w)}{2\sigma \sin(\pi\lambda D w^2) - 2\cos(\pi\lambda D w^2)}. \tag{5.10}$$

Here $\tilde{I}(\theta, w)$ is the one-dimensional Fourier transform of the phase-contrast sinogram. According to Equation 5.10, $\tilde{f}(u, v)$ is undetermined for frequencies that correspond to zero-crossings of the CTF. And since the accuracy of the linear approximation and the observations $\tilde{I}(\theta, w)$ is finite, $\tilde{f}(u, v)$ can only be computed outside of the circular bands that correspond to $|w - w_0| < \epsilon$ (Figure 5.1). Thus,

the described problem of the tomographic reconstruction based on single-distance phase-contrast data is underdetermined.

Let us introduce a discrete space-domain representation of the tomography problem. Assume that the vector $\boldsymbol{f}$ is composed from m samples of $f(x, y)$ defined on a Cartesian grid. Projections $p(\theta, s)$ are sampled on a regular grid of n elements stored in a vector $\boldsymbol{p}$. Using the Radon transform operator $\mathcal{R}$ we can write a discrete representation of Equation 5.7:

$$\boldsymbol{p} = \mathcal{R}\boldsymbol{f}. \tag{5.11}$$

Here $\mathcal{R}$ can be represented by an $n \times m$ matrix. This system can be solved using either an approximation of the $\mathcal{R}^{-1}$ (e.g. filtered back-projection) or in least-squares sense using one of the algebraic reconstruction algorithms (e.g. EM, ART, SIRT) [116].

For PRT, the tomography model represented by Equation 5.11 can be combined with the linear phase-contrast model of Equation 5.6 into a single linear inverse problem:

$$\mathcal{Z}\mathcal{F}\boldsymbol{I} = \mathcal{Z}\mathcal{P}\mathcal{F}\mathcal{R}\boldsymbol{f}. \tag{5.12}$$

Here, the linear operators $\mathcal{Z}$, $\mathcal{P}$ and $\mathcal{F}$ are applied to vectors of n elements that contain all projections generated by $\mathcal{R}\boldsymbol{f}$ instead of a single projection of k elements as it is in Equation 5.6. Their matrix representations can be easily constructed by stacking the corresponding "single projection" matrices into a block diagonal matrix of $n \times n$ elements.

5.2.4 Preconditioning

Before introducing algebraic methods suitable for solving Equation 5.12, we would like to introduce two other representations of the PCT problem that, under certain conditions, may be preferable due to faster convergence.

We will assume that for the frequencies $|w - w_0| > \epsilon$, Equation 5.1 can be accurately computed using direct inversion. Then Equation 5.12 can be rewritten as follows:

$$\mathcal{Z}\mathcal{F}\boldsymbol{\mu} = \mathcal{Z}\mathcal{F}\mathcal{R}\boldsymbol{f}, \tag{5.13}$$

where $\boldsymbol{\mu}$ is a vector representation of the projected attenuation of the object, which can be calculated from the phase-contrast sinogram $\boldsymbol{I}$ using direct phase retrieval. Algebraic methods based on Equation 5.13 are likely to converge faster than the ones based on Equation 5.12, since the inversion of the $\mathcal{P}$ operator is already solved during the phase retrieval step. However, unlike the approach, where the tomographic reconstruction is computed subsequently after phase retrieval, Equation 5.13 allows us to take into account that the information about the attenuation of the object is lost at spatial frequencies $|w - w_0| < \epsilon$. Such an approach can also be used when the number of tomographic projections is limited.

Yet another version of the linear system can be derived from the central slice theorem given by Equation 5.10. Now for the case that an accurate inverse Radon transform of the sinogram can be calculated. After changing from polar coordinates to Cartesian coordinates in Equation 5.10, we can write down the following discretized system:

$$\hat{\mathcal{F}}\mathcal{R}^{-1}\boldsymbol{I} = \hat{\mathcal{P}}\hat{\mathcal{F}}\boldsymbol{f}, \tag{5.14}$$

where $\mathcal{R}^{-1}$ is the approximated discrete inverse Radon transform (e.g. filtered back-projection), $\hat{\mathcal{F}}$ is the two-dimensional discrete Fourier transform and $\hat{\mathcal{P}}$ represents an elementwise multiplication with the discrete version of the two-dimensional CTF $= 2\sigma \sin\left(\pi\lambda D(u^2 + v^2)\right) - 2\cos\left(\pi\lambda D(u^2 + v^2)\right)$. Equation 5.14 permits application of algebraic algorithms with additional constraints to the phase retrieval problem while the problem of tomographic reconstruction is solved in a non-iterative manner. This approach can also be faster than calculation based on Equation 5.12, since it does not require recalculation of the back and forward Radon transform for each iteration.

5.2.5 Algebraic methods

An approximate solution of Equation 5.12 can be found using least-squares minimization:

$$\arg\min_{f} : \|\mathcal{A}\boldsymbol{f} - \tilde{\boldsymbol{I}}\|^2, \tag{5.15}$$
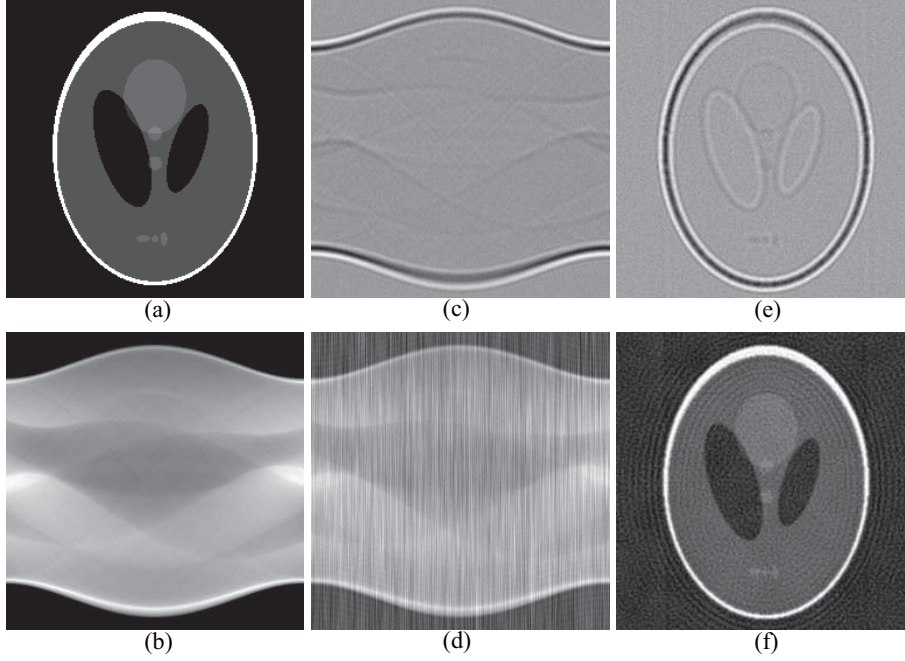
Figure 5.2: Simulated phase-contrast tomography of the Shepp-Logan phantom. (a) Ground truth; (b) projected attenuation; (c) observed phase-contrast sinogram; (d) sinogram after phase-retrieval; (e) 'direct' filtered-back projection; (f) filtered-back projection after phase retrieval.

where $\mathcal{A} = \mathcal{Z}\mathcal{P}\mathcal{F}\mathcal{R}$ and $\tilde{\boldsymbol{I}} = \mathcal{Z}\mathcal{F}\boldsymbol{I}$. Using gradient descent, $\boldsymbol{f}$ is computed according to the following iterative scheme:

$$\boldsymbol{f}_{j+1} = \boldsymbol{f}_j - 2\alpha\mathcal{A}^T(\mathcal{A}\boldsymbol{f}_j - \hat{\boldsymbol{I}}), \tag{5.16}$$

where j is the iteration number, $\mathcal{A}^T$ is the transpose of $\mathcal{A}$, so $\mathcal{A}^T = \mathcal{R}^T\mathcal{F}^T\mathcal{P}^T\mathcal{Z}^T$. The constant α represents the step size in the opposite gradient direction. In order to guarantee convergence, the constant α has to be sufficiently small and can either be calculated using an additional line-search step or from the eigenvalues of $(\mathcal{A}^T\mathcal{A})$ [117]. It is worth noting that the Fourier transform operator $\mathcal{F}$ is orthogonal, so $\mathcal{F}^T = \mathcal{F}^{-1}$; operators $\mathcal{Z}$ and $\mathcal{P}$ are represented by diagonal matrices, so $\mathcal{Z}^T = \mathcal{Z}$, $\mathcal{P}^T = \mathcal{P}$, and $\mathcal{R}^T$ represents the unfiltered back-projection operator.

We have mentioned previously that in conventional tomography a piecewise constant image $\boldsymbol{f}$ can often be computed accurately from severely underdetermined tomographic system using methods with additional constraints, such as TV minimization. In the TV minimization approach an additional term is added to the

objective function:

$$\arg\min_{f} : \|\mathcal{A}\boldsymbol{f} - \hat{\boldsymbol{I}}\|^2 + \lambda_{TV}\|\boldsymbol{f}\|_{TV}, \tag{5.17}$$

where $\|\boldsymbol{f}\|_{TV} = \sum \sqrt{(\nabla_h\boldsymbol{f})^2 + (\nabla_v\boldsymbol{f})^2}$, ∇_h and ∇_v are the horizontal and vertical finite difference operators and λ_{TV} denotes the weight of the regularization term.

Depending on the magnitude of λ_{TV} the solution will be promoted either towards greater conformity with the observed data or towards greater sparsity of the gradient magnitude. Equation 5.17 represents a non-smooth convex minimization problem which can be solved using one of the iterative TV minimization methods [61, 63]. In the current investigation we will demonstrate results obtained using so called FISTA-based TV minimization which is described in detail in [109]. The same algorithm was applied by us to several different phase-retrieval problems in [97]. Further on we call the solutions based on minimization of Equation 5.12 - *full algebraic reconstruction*, the ones based on Equation 5.13 - *algebraic tomographic reconstruction* and Equation 5.14 - *algebraic phase retrieval*.

5.3 Simulations

In order to compare the accuracy of tomographic reconstructions based on the proposed reconstruction approaches, we simulated phase-contrast tomographic data using Fresnel propagation. A discretized Shepp-Logan phantom (256 x 256 pixels) was used as a ground truth image to generate the density image $f(x, y)$ (Figure 5.2(a)). The wave function of the object $T(\theta, s)$ was computed for each tomographic angle θ using the following expression:

$$T(\theta, s) = \exp\left(-\frac{2\pi}{\lambda} \cdot (\beta + i\delta) \cdot \mathcal{R}f(x, y)\right), \tag{5.18}$$

were δ denotes the decrement of the complex refractive index, β stands for the attenuation index and $f(x, y)$ denotes a dimensionless normalized attenuation of the digital phantom. Subsequently, the intensity images were generated using the following expression:

$$I(\theta, s) = \mathcal{F}^{-1}\left(OTF \cdot \mathcal{F}|\mathcal{F}^{-1}(P_\lambda \cdot \mathcal{F}T(\theta, s))|^2\right) + noise, \tag{5.19}$$

where the Fresnel propagator is represented by $P_\lambda = e^{i\pi\lambda D w^2}$ and the Optical Transfer Function (OTF) of the imaging system is modeled by a Gaussian function $OTF = e^{-\frac{w^2 a^2}{2}}$ with standard deviation a (Figure 5.2(c)). Figure 5.2(e) shows the result of direct application of filtered-back projection to the "raw" phase-contrast images. The result of the sequential reconstruction is shown on Figure 5.2(d) and Figure 5.2(f). The retrieved phase images (Figure 5.2(d)) suffers from typical artifacts – low frequency noise and fringes around large variations of intensity. These artifacts correspond to spatial frequencies at which the CTF has low amplitude and the reconstruction errors are high. They are propagated into the subsequent tomographic reconstruction (Figure 5.2(f)).

All images were generated for monochromatic homogeneous illumination with a wavelength $\lambda = 0.31$Å (energy 40 KeV), propagation length $D = 1$ m and a pixel size of 1 μm. Noise was added to the sinogram after modeling the complete imaging chain. Since the intensity is varying only moderately across the sinogram, an additive Gaussian noise term was assumed to be a good model. Parameters used in various simulations are shown in Table 5.1.

Table 5.1: Simulation parameter sets

Simulation name:	Projection number (per 180° scan)	$\delta, \times 10^{-8}$	$\beta, \times 10^{-10}$	OTF a, μm	Noise STD
weak phase	360	0.5	0.5	0	0
few projections	**72**	0.5	0.5	0	0
blur	360	0.5	0.5	**3**	0
noise	360	0.5	0.5	0	**2e-3**
strong phase	360	**5**	**5**	0	0
realistic	180	5	5	1	1e-2

Simulated data was treated by five different reconstruction techniques: *sequential approach* (phase retrieval followed by the filtered back-projection), *unconstrained algebraic reconstruction* based on (Equation 5.12) and three algorithms based on TV minimization: *full algebraic reconstruction* - (Equation 5.12), *algebraic tomographic reconstruction* - (Equation 5.13), *algebraic phase retrieval* - (Equation 5.14). A known Gaussian OTF was included in all algebraic reconstruction models in order to achieve a sharper reconstruction. Reconstructions were performed on a 512 x 512 pixels grid in order to avoid boundary effects. The same stopping condition was

used for all algebraic methods:

$$\frac{\|\boldsymbol{f}_{j+1} - \boldsymbol{f}_j\|^2}{\|\boldsymbol{f}_j\|^2} < 10^{-5}. \tag{5.20}$$

The weight of the regularization term λ_{TV} had to be adjusted depending on the underlying linear system and the variance of the simulated data. Automated methods for determining the regularization parameters produce a wide spread of results depending on the method [118]. In this work the regularization parameters were selected empirically so, for a given combination of the linear model and the simulation conditions, a solution with a small RMSE would be obtained. For full algebraic reconstruction λ_{TV} varied in the range from 10^{-7} (for the "blur" simulation) to 10^{-5} (for the "strong phase" and "realistic" simulations). For algebraic tomographic reconstruction λ_{TV} was in the range from 10^{-10} to 10^{-8}. And for algebraic phase retrieval we used λ_{TV} ranging from 10^{-4} to 10^{-2}. The constant parameter ϵ was set to 10^4 m^{-1} for simulations with small errors ("weak phase", "few projections" and "blur") and 10^5 m^{-1} for simulations with large errors ("strong phase", "noise" and "realistic"). Figure 5.3 illustrates the error magnitude associated to the resulting reconstructions. The corresponding Root Mean Square Error (RMSE) can be found in Table 5.2.

Table 5.2: RMSE for six different simulations (rows) and five reconstruction algorithms (columns).

| Resonstruction:			TV minimization		
Simulation:	sequential recon.	algrebraic unconstr. recon.	algebraic full recon.	algebraic tomography	algebraic phase retr.
weak phase	0.043	0.031	0.003	0.021	0.043
few projections	0.113	0.113	0.010	0.027	**0.109**
blur	0.076	0.072	0.051	**0.082**	0.063
noise	0.112	0.084	0.043	0.040	0.047
strong phase	0.057	0.070	0.029	0.045	0.046
realistic	0.072	0.085	0.048	0.050	0.061
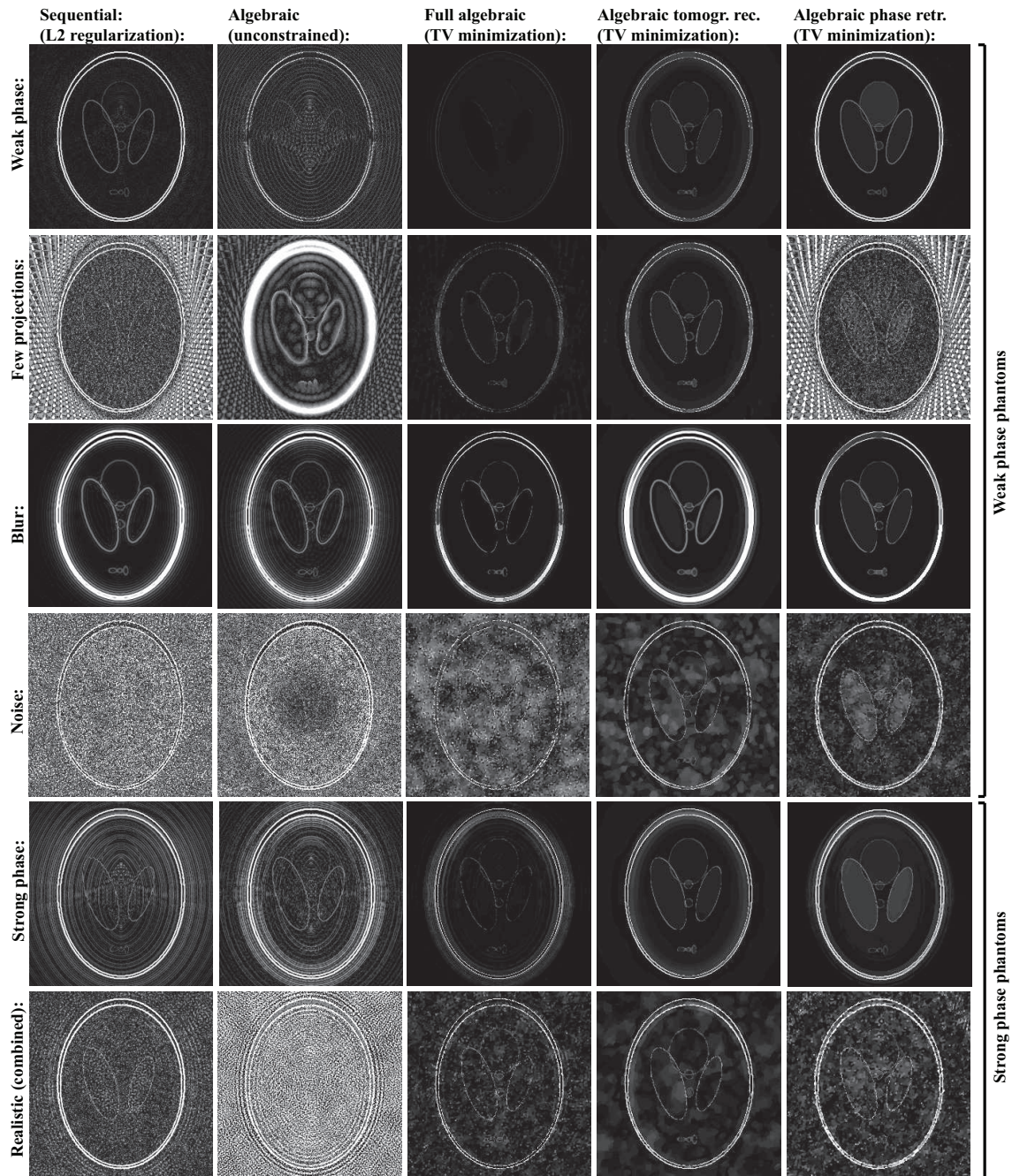
Figure 5.3: Reconstructions of the simulated data (error magnitude). Columns correspond to the reconstruction methods: sequential, unconstrained algebraic, full algebraic, algebraic tomographic reconstruction and algebraic phase retrieval. Rows correspond to the different simulations: weak phase, few projections, blur, strong phase, noise, realistic.

5.4 Experiments

In this section we are presenting some preliminary results of the *full algebraic reconstruction* and the *algebraic phase retrieval* methods applied to an experimental X-ray PCT dataset. The data was collected at the beamline ID11 of the European Synchrotron Radiation Facility (Grenoble, France). The tomographic scan was acquired in-situ for spherical polycrystalline copper (Makin Metal Powders (UK) Ltd., diameter 50 μm) during sintering at 1050°C. The specimen was placed in a quartz capillary with a 500 μm internal diameter. During the experiment gas shielding (argon: 98% and hydrogen: 2%) was applied. The scan was performed in a continuous 180° mode with 650 projections. Phase-contrast images were acquired using an X-ray beam with a mean energy E = 40 KeV ($\Delta E/E = 10^{-3}$), a source to object distance of 96 m and a propagation distance of 25 cm. The size of each image was 512 x 256 pixels with a pixel size of $1.4 \times 1.4 \mu m^2$.

We compared the standard sequential reconstruction employing L2-regularization with the proposed algebraic methods based on TV-minimization. Figure 5.4 shows the results obtained using three different reconstruction techniques: sequential approach, full algebraic reconstruction, and algebraic phase retrieval. All reconstruction techniques were applied to the complete dataset of 650 projections and a subset of only 65 projections. The red line on Figure 5.4 shows the position of the attenuation profiles that are depicted in Figure 5.5. In the sequential approach L2-regularization was used during the phase-retrieval, while the algebraic phase retrieval and the full algebraic reconstruction were performed using a three-dimensional FISTA-based TV minimization with non-negativity constraint. A Gaussian OTF was added to the CTF model in order to account for blurring with FWHM of 4.95 μm. We varied the number of iterations depending on the rough estimate of the convergence speed of a particular algorithm. In full algebraic reconstruction we used 2000 iterations. In algebraic phase retrieval based on 650 tomographic projections 300 iterations were used. Two times more iterations were used in both approaches when applied to 65 tomographic projections.
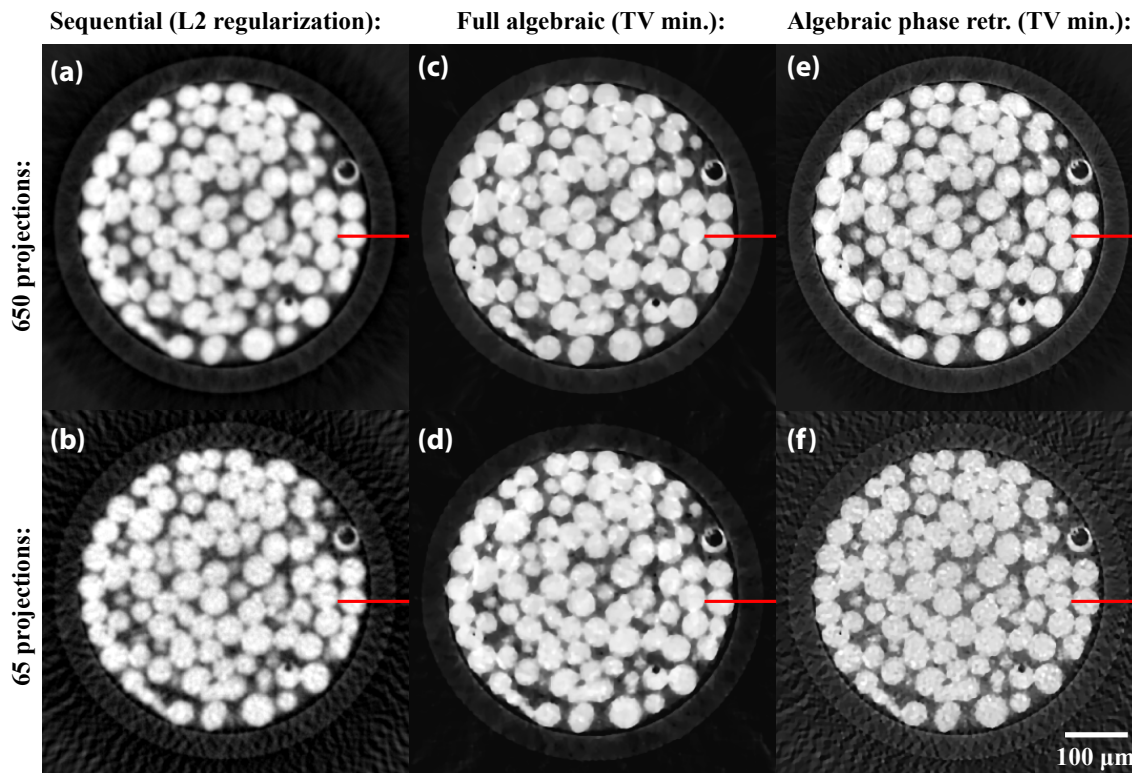
Sequential (L2 regularization): **Full algebraic (TV min.):** **Algebraic phase retr. (TV min.):**

Figure 5.4: X-ray PCT reconstruction of the glass capillary filled with copper spheres (slice from the middle of the volume). Reconstructions based on 650 projections: (a) - sequential approach based on L2-regularized phase retrieval, (c) - full algebraic reconstruction, (e) - algebraic phase retrieval. Reconstructions based on 65 projections: (b) - sequential approach, (d) - full algebraic reconstruction, (f) - algebraic phase retrieval. Red line shows position of the profiles depicted on the next figure.

5.5 Conclusion

The results of reconstructions for the simulated data (Figure 5.3) demonstrate that a TV minimization approach can yield a nearly flawless tomographic reconstruction based on a single distance X-ray PCT data (full algebraic reconstruction applied to the weak phase case). In most of the demonstrated examples the full algebraic reconstruction approach outperforms the other two approaches: the algebraic tomographic reconstruction and the algebraic phase retrieval.

However, there are certain cases where the technique will not work so well. The algebraic tomographic reconstruction method clearly fails in the case with strong blur applied to the simulated data. That is an expected outcome since the blur is not included in the linear system that is solved algebraically. The algebraic

phase retrieval method is failing in the case that the dataset contained only a few projections. It is also expected since the back-projection sub-problem is not solved by the algebraic algorithm but calculated once using filtered back-projection. However, given the advantages of the full algebraic reconstruction, it also suffers from certain disadvantages - it is the most computation-intensive of the methods proposed in this article. It also is likely to converge slower than the other two in terms of the number of iterations.
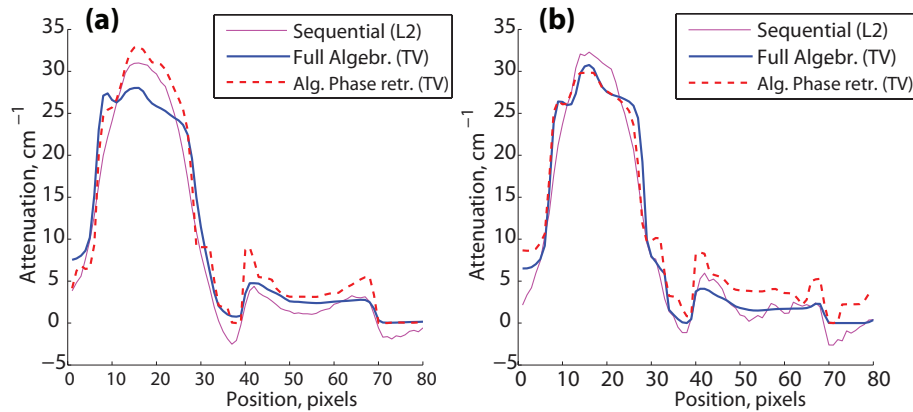

Figure 5.5: Attenuation profiles of the copper sphere and the quartz wall for different reconstruction algorithms. (a) Reconstruction based on 650 projections; (b) reconstruction based on 65 projections.

All reconstructions in this paper were applied to the data (recorded as well as simulated) of objects that comply with the assumption of sparsity, i.e. objects with a piece-wise constant attenuation. Other studies show that TV minimization can improve the accuracy of the reconstruction of images that are not strictly sparse [108]. Further investigation should be carried out in order to test the applicability of the Phase Retrieval Tomography based on TV minimization to non-sparse objects, such as those encountered in soft-tissue imaging.

In the current study we investigated a simple case of tomographic reconstruction for parallel beam geometry combined with a single-distance CTF phase-retrieval model. This combination represents a linear inversion problem, so algebraic reconstruction algorithms can be applied to solve it with minimal adjustments. However, there are a large number of variations to the proposed technique that can be considered during further investigation. A generalized description of the central slice theorem for fan-beam or cone-beam geometries [119, 120] should allow extension of the current approach to these geometries. Some of the phase retrieval models other than the

CTF model can be easily incorporated into an algebraic reconstruction similar to the two-dimensional phase retrieval in [97]. Specifically, the problem of tomographic reconstruction based on a multi-distance CTF model [47] remains linear, whereas incorporation of the so called mixed phase retrieval [50] will require solving a non-linear problem.

The experimental data was recorded during an in-situ sintering experiment during which acquisition at shorter propagation distance or in attenuation-contrast mode was not possible. Taking into account that the specimen yields strong attenuation and rapid phase variations, this imaging regime leads to significant artifacts when linear phase retrieval or no phase retrieval is used for tomographic reconstruction. However, it seems that the use of TV minimization with a non-negativity constraint leads to a solution with visibly higher contrast and sharper boundaries. A further development of algebraic techniques may facilitate more accurate tomographic reconstructions based on experimental data acquired under similar (suboptimal) conditions.

Another important result is the full algebraic reconstruction based on fewer projections. It can be seen, that this method allows to reduce the artifacts significantly in reconstruction based on a limited number of projections. Both results can justify the high computational cost of the proposed algebraic algorithms in applications where the acquisition time and the radiation dose are highly restricted.

6 In-situ imaging of a solid-state phase transformation with x-ray Phase Contrast Tomography

Abstract[1]

The theory of diffusional solid-sate phase transformations plays a crucial role in understanding the evolution of the microstructure during processing of metals, which influences the properties of metallic alloys. Using propagation-based x-ray Phase-Contrast Tomography (PCT) we have obtained the first series of three-dimensional reconstructions of the evolution of the morphology of individual interfaces between ferrite and austenite grains during the ferrite-to-austenite phase transformation in steel. The tomographic data was acquired within a time span of approximately 150 minutes and with a time resolution of approximately 9 minutes per dataset and a spatial resolution of 1 μm^3. During this time span, the temperature of the specimen was increased from 800°C to 900°C. The ferrite-to-austenite phase transformation took place between 860°C and 890°C. While state-of-the-art phase-field simulations only predict the formation of curved interfaces between ferrite and austenite, the experiments reveal the presence of large planar interfaces, some of which are immobile during most of the phase transformation. This phenomenon is thought to be related to special crystallographic orientation relationships between the parent and product grains.

---

[1]This work is currently in preparation for publication in a journal: A. Kostenko, R. Huizenga, A. King, W. Ludwig, L. J. van Vliet and S. E. Offerman, "In-situ investigation of the evolution of the 3D-morphology of moving interfaces between individual grains of ferrite and austenite".

6.1 Introduction

Modern society is fully dependent on the affordable design and production of materials for high-tech industries such as aerospace, power production, electronics, transport, consumer goods and many others. Considering the increasing levels of consumption in the developing countries, the growing human population, and the diminishing availability of high-grade ores, the development of affordable metallic alloys with advanced properties becomes especially important. The key to the affordable production of metals is in controlling the evolution of the microstructure during the processing of metals.

Diffusional solid-sate phase transformations take place during the production processes of important metals, e.g. steel, titanium and magnesium-lithium alloys. During these phase transformations, grains of the product phase nucleate and grow within the parent phase. The kinetics of these processes have been studied for more than 60 years, which resulted in a large number of different theoretical models [121]. However, experimental validation of these theories has been limited until today, laboratory experiments only provided information on the average growth rate of the product grains [121]. The advent of third-generation synchrotron facilities opened the opportunity to study the growth kinetics of individual grains during diffusional solid-state phase transformations by observing the evolution of the volume of individual grains [46]. However, direct experimental observations of the 3D-morphology of moving interfaces between phases during diffusional solid-state phase transformations have not been reported in the literature up to now. The experimental investigation that comes closest to studying the evolution of the 3D-morphology of individual interfaces is the study by Schmidt et al. [122] during interrupted recrystallization in aluminum. This study was non-destructive in nature, but the measurements were made ex-situ due to the long acquisition times that are currently inherent to three-dimensional x-ray diffraction microscopy.

The goal of the current investigation is to study the evolution of the 3D-morphology of individual interfaces between the product and parent phases during a diffusional solid-state phase transformation in metals. We focused on visualizing the motion of the interfaces between austenite (gamma-iron) and ferrite (alpha-iron) grains during ferrite-to-austenite phase transformation in steel. Such an investigation requires a non-destructive imaging technique capable of acquiring real-time observations and a computational approach to obtain a 4D reconstruction of the process (xyzt).

The density difference between austenite and ferrite is too small to be detected by conventional x-ray attenuation-contrast tomography. A 3D-reconstruction of the microstructure at the level of individual grains can be measured by three-dimensional x-ray diffraction (3DXRD). However, this technique requires very long acquisition times (typically 10 hours) and is currently limited in spatial resolution (typically 5 micrometers). In order to detect very small density differences between two materials, propagation-based PCT has been successfully used to study microstructures in metals [45]. Previously, we obtained a three-dimensional reconstruction of large cementite structures within a volume of ferrite in steel using propagation-based x-ray PCT [97]. The typical time needed for acquisition of the tomographic PCT dataset at the materials science beamline ID11 of the European Synchrotron Radiation Facility (ESRF) in Grenoble (France) was on the order of 30 minutes [97]. In the current work we managed to reduce the acquisition time to approximately 9 minutes. This opens the opportunity to study the evolution of the 3D-morphology of individual interfaces between ferrite and austenite grains during the ferrite-to-austenite phase transformation during slow heating by means of PCT.

6.2 Materials and methods

6.2.1 Material and experimental setup

We studied hypoeutectoid steel with the following chemical composition (in wt%): 0.099 C, 0.98 Mn, 0.10 Nb, and the balance is Fe. Figure 6.1 shows the optical microscopy image of the ferrite grains in the material of the specimen before it was used in the experiment. The temperature range during which the austenite and ferrite phases for this composition co-exist, is calculated to be between A1 = 832°C and A3 = 869°C assuming ortho-equilibrium conditions and using the computational thermodynamics Thermo-Calc Software (Stockholm, Sweden). From dilatometry measurements and studies based on 3DXRD data [123], it is evident that during the phase transformation, 80% of ferrite is transformed into austenite within a short temperature range between 865°C and 870°C (heating rate of 2°C/min).

To avoid oxidation at high temperatures, the steel samples were placed into quartz tubes with an outer diameter of Ø3 mm and a wall thickness of 0.5 mm (see Figure 6.2). The tubes had a thicker (Ø6 mm) part, so they could be connected to
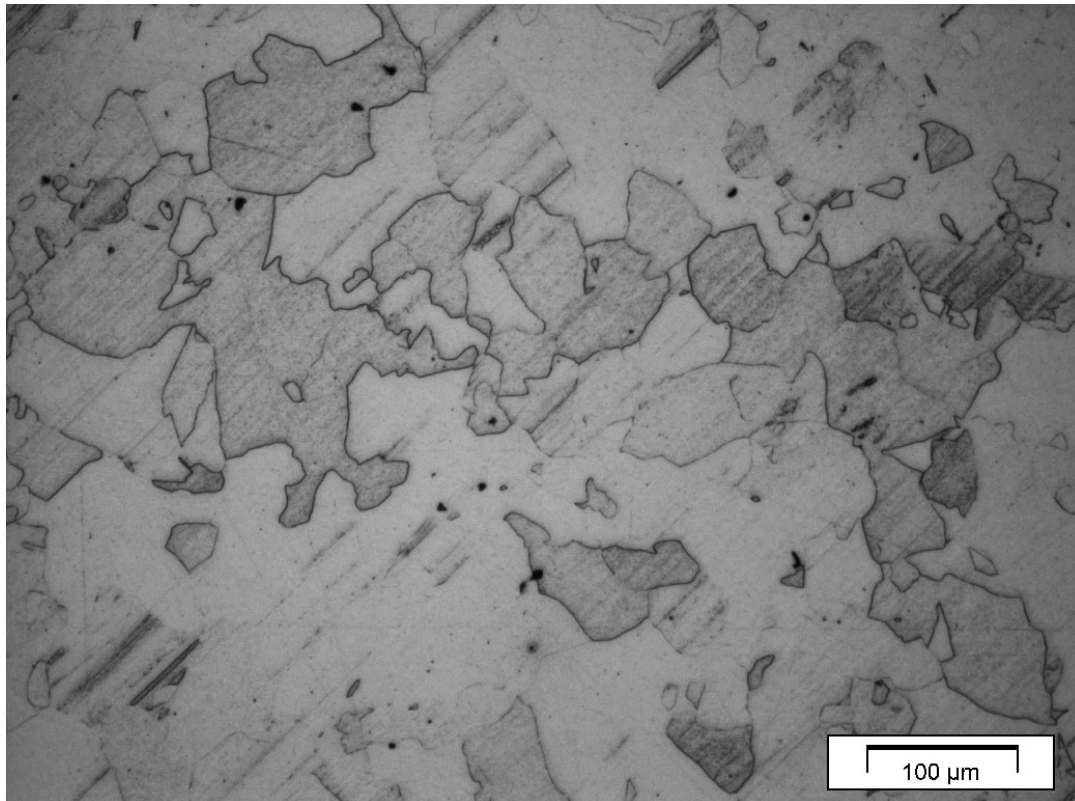
Figure 6.1: An optical microscope image of the ferrite grains within the investigated material.

a vacuum pump. The tubes were purged several times by applying vacuum of 10^{-4} mbar followed by letting helium in at 0.2 bar. After purging, the quartz tubes were filled with 0.2 bar helium and sealed by melting the thicker section of the tube. Helium was introduced under low pressure at the room temperature to make sure that the pressure inside the tube will not significantly exceed the atmospheric pressure when heat is applied.

In order to perform a series of in-situ experiments with working temperatures in the range from 700°C to 900°C we designed a miniature furnace that can be easily installed or removed without touching the sample (see Figure 6.2). This furnace permits a very flexible experimental geometry with object-to-detector distances down to about 10 mm (or less in case the furnace is removed). The furnace was made from an alumina tube with an Ø8 mm outer diameter and a 1 mm wall thickness. A nickel coil with a wire diameter of Ø0.2 mm was winded around the outer surface of the tube and isolated by using high temperature cement. Two round windows were drilled in the wall of the tube to avoid attenuation of both the incoming x-ray
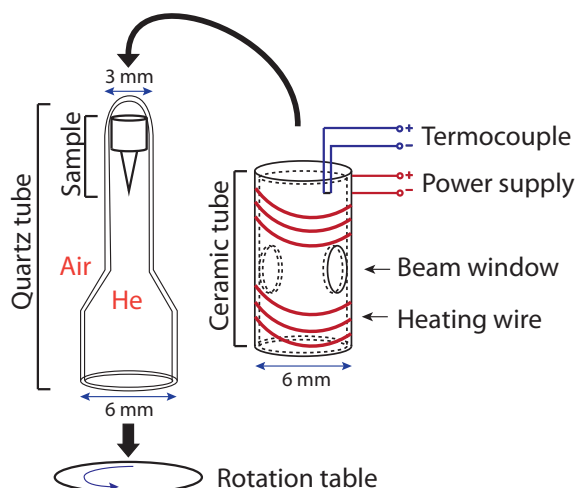
Figure 6.2: Sample mounting and the mini-furnace. The sample is mounted inside the top section of a sealed quartz tube. The tube is filled with helium to prevent oxidation of the sample at high temperatures. During the experiment the top section of the quartz tube is inserted into an open design mini-furnace.

beam and the Bragg diffraction from the specimen up to 2Θ-angle of 45°.

A thermocouple was attached to the top end of the alumina tube. The furnace was mounted on a motorized translation stage, so it could be moved up and down along the sample's rotation axis in a controlled fashion. The temperature inside the alumina tube was controlled using a Eurotherm (Invensys Eurotherm, The Netherlands) connected to the thermocouple in the top of the tube. In order to reach 900°C, a power of about 90 W was needed.

The samples were manufactured in a needle-shaped fashion (~ Ø0.1-0.5 mm and 2 mm long) in order to permit a 360° tomographic acquisition using a relatively low-energy x-ray beam. The mean x-ray energy was set to 34.6 KeV, a higher energy would yield a weaker phase-contrast effect. The base of the needle has a diameter of 1.9 mm, which was glued to the top of a thin section of the quartz tube using high temperature cement. In this way, the thicker part of the quartz tube could be mounted to the rotation stage and the sample could be suspended in the top part of the tube, see Figure 6.2. In this setup, flat-field images can easily be acquired during PCT by either removing the quartz tube with the sample completely out of the field of view or moving it up inside the furnace, so the x-ray beam can pass through the empty part of the quartz tube (the latter approach was used in the current experiment).

The geometry of the PCT acquisition setup is depicted in Figure 6.3, as constructed at the materials science beamline ID11 of the European Synchrotron Radiation Facility (ESRF) in Grenoble, France. To perform a time-dependent in-situ experiment, one needs to achieve the highest possible flux to limit the time needed for the PCT
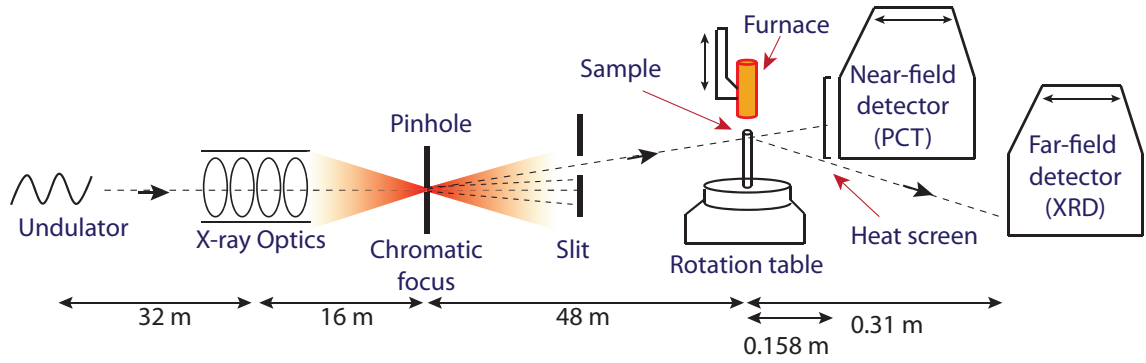
Figure 6.3: Acquisition geometry. Pinhole monochromator yields a "pink beam" with high brightness. One of the two detectors can be used at a time: the high-resolution near-field detector for PCT, the medium-resolution far-field detector for XRD acquisition.

acquisition performed at each stage of the phase transformation. In order to do so we used a pinhole monochromator instead of the conventionally used crystal or multilayer monochromator. A transfocator (compound refractive lens) was used to focus x-rays with an energy of 34.6 KeV at the pinhole that was placed in the optical hutch of the beamline. As the transfocator optics are chromatic, a broad band pass ("pink beam") monochromator can be constructed using a pinhole as shown in Figure 6.3. A slit that is placed after the pinhole is needed to block the central, unfiltered part of the beam. The bandwidth of this system was measured to be 0.5 KeV (FWHM) or $\Delta E/E = 1.4 \cdot 10^{-2}$, yielding two orders of magnitude higher flux in comparison with the Laue-Laue crystal monochromator. This allowed us to limit the exposure time to 0.2 sec per image. However, the full acquisition time was ~0.7 sec per image (including the CCD readout time) or 5 minutes and 53 seconds for 360° tomographic acquisition. An additional 2 minutes and 45 seconds were spent on the acquisition of dark- and flat-field images between the subsequent scans.

Figure 6.3 shows that the sample was placed at approximately 96 m from a 57×10 μm (H×V) undulator x-ray source and 48 m from the focal spot of the transfocator. A thin film scintillator, optically coupled to the FreLoN 4M CCD detector, was placed at a distance of 158 mm from the sample. Optical coupling with 25x magnification resulted in an effective pixel size of 0.96 μm. Each tomographic acquisition consisted of 500 projections that were acquired with uniform spacing in 360° angular range. The detector area of 640 x 470 pixels was illuminated by the x-ray beam resulting in a reconstructed volume of the sample of approximately 600 μm in height and 300 μm in diameter.

A FreLoN-based taper-coupled large area detector was placed at 310 mm behind the sample to collect the X-ray Diffraction (XRD) signal which was used to calibrate the exact temperature of the sample. During calibration, the phase transformation temperature was determined by comparing the XRD signal with 3DXRD results presented in [123]. Based on this comparison we found that the sample temperature T_s at the position of the x-ray beam is 110° higher than the temperature of the furnace wall T_f measured by the thermocouple.

During the in-situ PCT acquisition the sample was heated from $T_s = 810°C$ to $T_s = 860°C$ at a rate of 10°C/min and from $T_s = 860°C$ to $T_s = 900°C$ at a rate of 0.278°C/min. Each tomographic scan (including acquisition of flat-field images at the beginning and at the end of the scan) took 8 min and 38 seconds. During each tomographic scan that took place above $T_s = 860°C$, the temperature increased by 2.4°C.
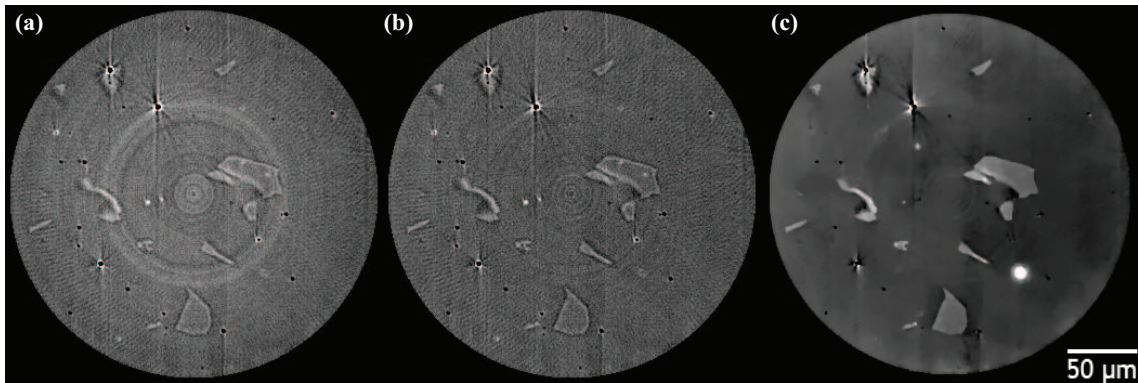
6.2.2 Image reconstruction

Figure 6.4: Processing of the phase-contrast data. (a) - FBP applied to the raw phase-contrast sinogram; (b) – FBP after correction of ringing artifacts; (c) – the reconstruction based on algebraic phase retrieval.

The phase-contrast tomographic data acquired during the experiment was pre-processed using the standard dark-field and flat-field correction [105]. Fast variations of the x-ray beam intensity were corrected in each individual phase-contrast image by subtracting the average intensity of the pixels that lay outside of the specimen. In propagation-based x-ray PCT each observed image can be interpreted as a sum of attenuation-contrast and phase-contrast effects. In conventional attenuation-contrast imaging the observed image $I(x, y)$ is formed according to the Beer-Lambert

law:

$$I(x,y) = I_0 e^{-2\mu(x,y)},$$

where I_0 denotes the intensity of the incoming x-ray beam (uniform intensity) and $\mu(x,y)$ stands for the projected attenuation of the specimen. After computing the projected attenuation $\mu(x,y)$ for each tomographic orientation, a tomographic reconstruction of object's three-dimensional attenuation index can be calculated. However, changes in the attenuation index, might be too small to detect the structures that correspond to small variations in density or chemical composition of the specimen. Such structures can often be detected using phase-contrast imaging. To a first approximation, the images observed using propagation-based phase-contrast imaging are proportional to the Laplacian (second derivative) of the specimen's projected electron density [49]. One of the most simple approximations of the phase-contrast image is given by [52] for homogeneous objects:

$$I(x,y) = I_0 (1 - a\lambda R \nabla^2) e^{-2\mu(x,y)},$$

where a is a constant that characterizes the magnitude of the phase-contrast effect for the given material and x-ray energy, λ denotes the wavelength of x-ray beam, R is the object-to-detector distance in a parallel beam geometry, and ∇^2 is the Laplacian operator. Unfortunately, all phase retrieval techniques for homogeneous objects [52, 53, 54] rely on approximations (such as limited or slowly varying attenuation) which break down around the steel-air boundary. That leads to artifacts in phase retrieved images localized at the outer boundary of the specimen and in the vicinity of the gas pores present in the bulk.

Experimental data acquired using propagation-based PCT is sometimes processed in the same way as attenuation-contrast tomography - by direct application of filtered back-projection (FBP). A horizontal slice of the specimen reconstructed using this approach is shown in Figure 6.4(a,b). However, to obtain a correct representation of the specimen's attenuation (and hence density), tomographic reconstruction must be combined with phase retrieval. To compute tomographic reconstructions of the specimens attenuation (Figure 6.4(c)) we used the *algebraic phase retrieval* approach that we reported previously in [106]. We used a 3D analysis software package Amira (VSG, FEI Company) to perform segmentation of the reconstructed attenuation volume. The segmented data was used to produce a three-dimensional rendering of
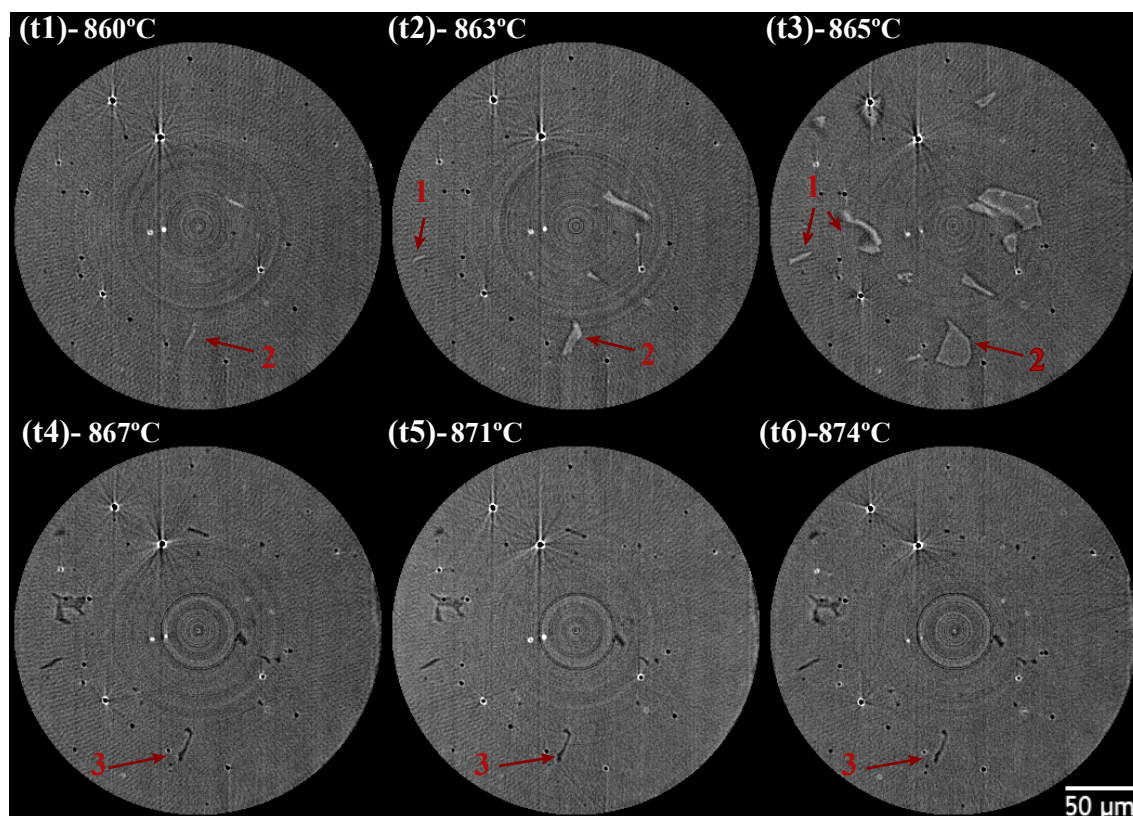
the austenite structure (Figure 6.6).

Figure 6.5: Time-lapse PCT (no phase retrieval) of the ferrite-austenite phase transformation. Growth of the austenite grains in the bulk of ferrite is visible at the time points t1, t2 and t3. At the time points t4, t5 and t6 only small amounts of ferrite that remains after the phase transformation can be seen. Grains marked as (1) form an interconnected network at t3 (see in 3D on (Figure 6.8)). A single austenite grain (2) demonstrates an immobile interface (see in 3D on (Figure 6.7)) which can also be observed at time points after t3 due to a small amount of ferrite remaining next to it (3).

6.3 Results and discussion

Figure 6.5 shows FBP reconstructions of a single horizontal slice through the object from the data recorded in-situ during the heat treatment. Time points $t1$-$t6$ correspond to the average specimen temperaure in the range from $T_s = 860°C$ (time point $t1$) to $T_s = 874°C$ (time point $t6$). Due to the phase-contrast effect, interfaces between the austenite grains and the surrounding ferrite can be clearly seen on the

first three subfigures (Figure 6.5($t1$, $t2$, $t3$)). They correspond to the first 28 minutes and 32 seconds of heat treatment during which the average temperature increased by 7.2°C. The last three subfigures (Figure 6.5 ($t4$, $t5$, $t6$)) show that the specimen contains very small amounts of ferrite that remains after the phase transformation. The smallest traces of ferrite can still be observed in reconstructions that correspond to an average sample temperature of 889°C or approximately 100 minutes from the start of the phase transformation.

Although the temperature of the furnace followed the programmed value, it showed fast oscillations with a standard deviation of ~ 1.5°C. In addition to that, during each flat-field acquisition, the sample had to be vertically moved by 2 mm inside the furnace, which resulted in an increase of the sample temperature due to the thermal gradient within the furnace. We estimate that the temperature of the sample could increase 10°C between the subsequent tomographic acquisitions. Reconstructions computed using only half of each tomographic dataset (in 180° angular range) confirm that during each acquisition, the amount of austenite increases only by a very small fraction, while the subsequent acquisitions show that the fraction of the austenite increases by an order of magnitude. Most likely, the majority of the ferrite was rapidly converted to austenite during flat-field acquisition after $t3$ ($T_s = 865$°C). The subsequent time point $t4$, acquired at an average temperature $T_s = 867$°C, shows that the sample consists mainly of austenite.

Figure 6.6 shows a three-dimensional rendering of the austenite grains in the beginning of the phase transformation and the remaining ferrite at the end of the phase transformation. Growing austenite grains are shown in green (Figure 6.6($t1$, $t2$, $t3$)). The austenite grains painted in blue and red colors are visualized separately in Figure 6.7 and Figure 6.8. Interfaces shown in purple color correspond to the ferrite that remains at the end of the phase transformation (Figure 6.6($t4$)). The austenite volume fraction can be calculated from the segmented data and correspond to 0.01%, 0.12%, 3.9% and 99.6% (Figure 6.6($t1$, $t2$, $t3$)).
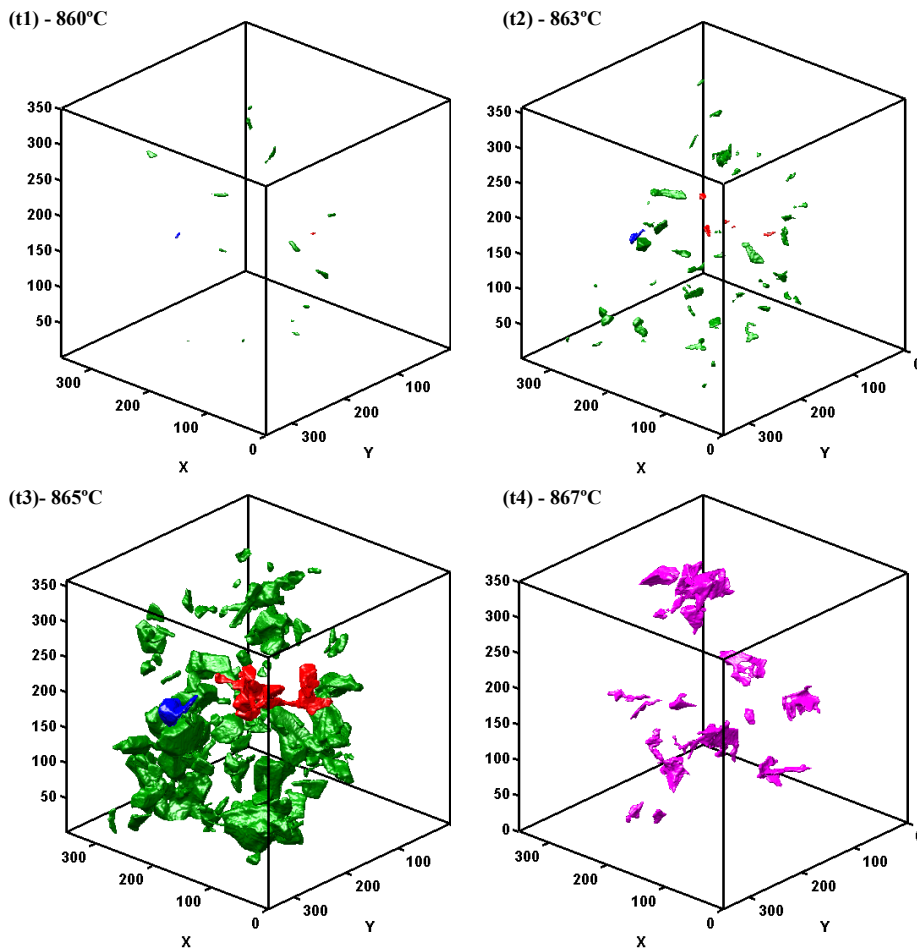
Figure 6.6: 3D rendering of the ferrite-austenite interfaces during the heat treatment. Austenite grains are shown in green ($t1$)-($t3$); ferrite remaining after phase transformation is shown in purple ($t4$). A grain displayed in blue demonstrates an immobile interface (shown in Figure 6.7). Several austenite grains that form an interconnected cluster at $t3$ are shown in red (shown in Figure 6.8).

Comparison of the tomographic reconstructions, that correspond to the time points from $t1$ to $t4$, allows to make some unique observations related to the kinetic properties of the austenite grain growth. The state-of-the-art 3D phase-field simulations [124] only predict the formation of curved interfaces between ferrite and austenite. However, it appears from the time point $t3$ that most of the surface of the growing austenite grains is represented by either large relatively planar interfaces with sharp edges or more irregular surfaces that usually comprise several smaller flat areas (Figure 6.6). Comparing the positions of the interfaces of the austenite grains at the time points $t1 - t3$ and the positions of the remaining ferrite at $t4$ we can

conclude that there is a significant number of interfaces that remain immobile during the phase transformation. We estimated that about one third of the total number of grains (or interconnected clusters of grains) at $t3$ show the presence of at least one immobile interface. Toal area of the immobile inerfaces that can be directly detected from the available data at $t3$ amounts to approximately 5%. Obviously only a fraction of the immobile interfaces can be directly detected by comparing only a few time points which decribe rapidly changing grains. We expect that when the detected immobile interface belongs to a larger planar surface, the whole planar surface should be assumed immobile. In that case, we can estimate the surface of immobile interfaces to be about 15-20% of the total surface of the grains at $t3$.
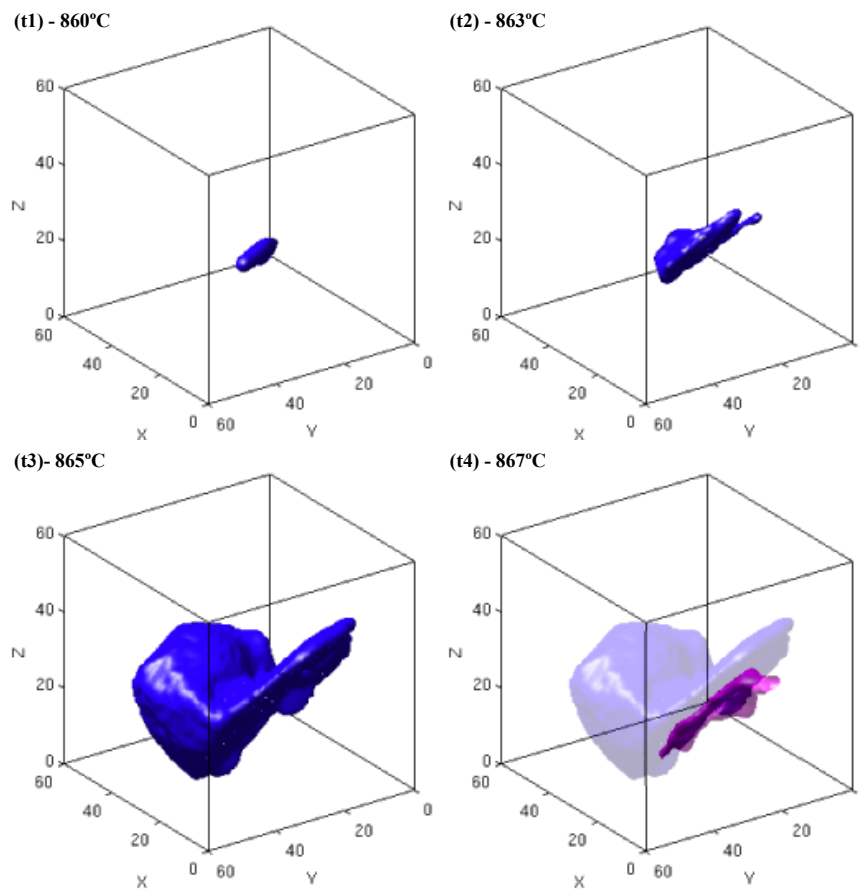

Figure 6.7: Demonstration of an immobile interface during the growth of an austenite grain (a)-(c). (d) – ferrite grain structure that remains adjacent to the immobile interface at the end of the phase transformation.

An example of an immobile interface is visualized in 3D in Figure 6.7 and can be seen in crossection in Figure 6.5 (it is marked with a red arrow with a label '2'). It is

evident that when the temperature increases, the austenite grain grows only on one side of the planar interface (Figure 6.7 (*t*1, *t*2, *t*3)), while a small amount of ferrite remains on the other of the interface when the transformation is almost complete (Figure 6.7(*t*4)).

A formation of a large cluster of interconnected austenite grains is shown in Figure 6.8. The same grains are marked with a red arrow and a label '1' in Figure 6.5. This cluster of austenite grains also demonstrates a large number of planar interfaces. Moreover, Figure 6.8 suggests that individual austenite grains grow along particular preferred directions which results in larger interconnected clusters than one would expect after assuming isotropic growth. We believe that both effects, the presence of the preferred growth directions and the planar interfaces, can be explained by the two following mechanisms. Firstly, the growth of the austenite along ferrite/ferrite grain boundaries might be faster due to higher diffusion rates in the vicinity of the grain boundary. Secondly, the growth of the austenite grain can be affected by specific crystallographic orientation relations between the austenite and the surrounding ferrite. According to Gottstein and Shvindlerman [125] planar interfaces in single-phase materials are likely to be less mobile due to crystallographic orientation relations between neighboring austenitic and ferritic grains.
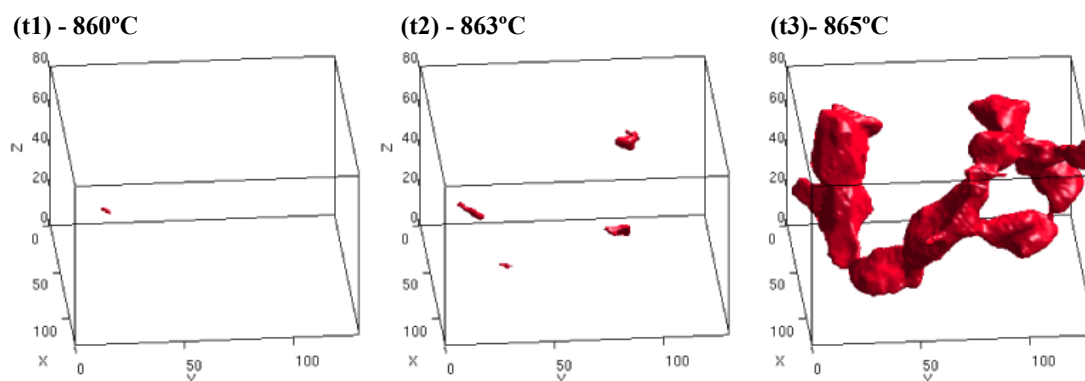

Figure 6.8: Demonstration of austenite grain growth and cluster formation (shown on Figure 6.6 in red).

6.4 Conclusions

We have presented the first 4D reconstruction of the evolution of the three-dimensional morphology of individual interfaces between ferrite and austenite grains during the

ferrite-to-austenite phase transformation in steel. Propagation-based x-ray PCT was used to acquire the data needed for the full three-dimensional reconstruction of the cylindrical specimen of approximately 600 μm height and 300 μm in diameter with a spatial resolution of approximately 1 μm^3 and a temporal resolution of around 9 minutes. The experiment was conducted in-situ, while the sample was heated from 860°C to 900°C at a rate of 0.278°C/min.

From the point when the first grains of austenite can be detected, till the moment when ferrite becomes undetectable, the temperature changed almost as much as 50°C. However, the majority of ferrite is transformed into austenite when the average temperature of the sample changes within approximately 5°C range. Although the temperature may have been changing by as much as 10°C for a short time between the consecutive tomographic acquisitions. Based on the experimental data, we made several observations of features that are not predicted by state-of-the-art phase-field simulation models. Reconstructions show the presence of a large number of planar interfaces, some of which remain immobile during the phase transformation. We hypothesize that this feature of the interface morphology and kinetics is related to the particular crystallographic orientation relationships between the ferrite and austenite grains.

6.5 Recommendations

The results shown in this paper demonstrate how propagation-based x-ray PCT can be used for in-situ imaging of the ferrite-austenite interfaces during the phase transformation. A compact heating system allows to use a high resolution detector at a very short distance from the sample if needed. The spatial resolution achievable at the ID11 beamline is sufficient for the detection of the product phase grains at early stages of growth (either austenite or ferrite of ~ 3 μm in size). However, the temporal resolution remains relatively low. We believe that due to the relatively simple geometry of the grain interfaces, their position can be determined with submicron accuracy, provided that they would not move during the acquisition. However, due to the motion of the interfaces, the accuracy of their determination will strongly depend on the acquisition time.

In order to decrease the acquisition time and hence improve the temporal resolution of the imaging system, several changes can be implemented. By using the FreLon 2K

camera it is possible to reduce the readout time to 50 ms per frame (500 ms in our experiment). Also, the exposure time (current value is 200 ms) can be significantly reduced by improving the optical coupling between the scintillator and the FreLoN 4M CCD. The flat-field and dark-field images can be acquired less often, as long as it is possible to estimate the changes in the flat-field using intensity values from the parts of the CCD that are not attenuated by the specimen. By implementing these improvements it could be possible to reduce the acquisition time to 1-2 minutes per tomographic scan.

Apart from adjusting the hardware, there are several other ways to overcome the limited temporal resolution. Firstly, a specimen with different composition can be used to slow down the phase transformation time or to stabilize the phase transformation for the duration of the acquisition. Secondly, it should be possible to change the acquisition protocol to a faster one with less tomographic projections per dataset. Algebraic reconstruction algorithms of the type that was proposed by us in [126] may allow to reduce the amount of experimental data needed for accurate reconstruction dramatically.

The experimental setup presented in this paper can be significantly improved in order to achieve better temperature control and robustness of the heating system. Using conductor or semiconductor ceramics (e.g. SiC, ZrO_2 etc.) it should be possible to construct an extremely compact heating furnace with an outer diameter on the order of 5 mm and a working temperature above 1000°C. Reducing the size of the furnace will require smaller samples. This can be achieved by using samples with a thick Ni coating which can prevent oxidation of the steel specimen in air for few hours during the heat treatment [127]. Ni-coated samples will also allow an easy attachment of the thermocouples directly to the sample which could provide very robust control over the temperature. In addition, we recommend not to move the specimen inside the furnace to avoid unnecessary temperature fluctuations.

Conclusions

The main goal of this research is to develop a combination of tomographic reconstruction algorithms and experimental data-acquisition methods for propagation-based Phase-Contrast Tomography that would allow to carry out state-of-the-art investigations in the soft and hard condensed matter with improved spatial and temporal resolutions. The experimental work that was carried out in the field of materials science, demonstrated that propagation-based PCT provides a valuable tool for non-destructive imaging of microstructural changes that occur in metals during various production processes.

Novel X-ray sources: characterizing the MIRRORCLE-6X. Our first investigation, presented in Chapter 2, was aimed at the characterization of a novel X-ray source based on the miniature synchrotron technology MIRRORCLE-6X. The main motivation of this work was to test the suitability of this X-ray source for the development of a laboratory propagation-based X-ray PCI system. During this project we measured the phase-contrast enhancement of the imaging system based on the MIRRORCLE-6X under various conditions. Certain properties of the system, such as the X-ray spectrum of the source and the quantum efficiency of the detector, could not be measured during the experiment and were calculated theoretically. Depending on the particular geometry of the propagation-based PCI system, the observed contrast enhancement due to the phase-contrast effect, in comparison with the measured attenuation-contrast, was in the range from 100 to 200% . The predicted value for contrast-enhancement based on the effective source size, was estimated to be of several hundreds percent for the given experimental conditions. From the analysis of the experimentally observed data and the results of the simulations, we concluded that a major fraction of the radiation produced by the MIRRORCLE-6X was generated by the components (glue and carbon wire) needed for mounting of the X-ray target. This meant that an effective source size smaller than 40 microns was not achievable in the MIRRORCLE-6X at the time of the experiment, which

significantly reduced the spatial coherence of the X-ray source and hence the observed phase-contrast effect. Improvements on the design of the mounig of the target and on the focusing of the electron beam may lead to a significant increase in the brilliance of the X-ray source and its suitability for PCI.

Cementite morphology   The aim of the research described in Chapter 3 is to validate the technique of propagation-based PCT for the study of the three-dimensional mophology of cementite structures in steel using the golden standard of optical microscopy in combinations with serial sectioning. Formation of cementite takes place during various production processes and has a profound influence on the mechanical properties of steel. We used propagation-based PCT and a high-carbon steel specimen that contains large ($\gg 10\mu m$) cementite particles. We were able to obtain the first reconstruction of the three-dimensional morphology of the cementite grains using a non-destructive imaging technique. In this work we compared several different phase retrieval techniques and came to the conclusion that the linear phase retrieval model proposed by Wu [54] for homogeneous objects was the most convenient one: the specimen under investigation was nearly homogeneous (the phase to attenuation ratio close to constant), which allowed us to reduce the number of phase-contrast images required for the reconstruction. Using this technique we obtained a tomographic reconstruction of the cementite grains with a spatial resolution of approximately 1.5 μm within a large volume of steel ($600 \times 400 \times 250~\mu m^3$). This reconstruction was combined with data acquired in an X-ray Diffraction-Contrast Tomography (DCT) experiment. X-ray DCT requires long acquisition times and yields relatively low resolution ($\sim 10\mu m$), but allows to obtain highly relevant complimentary information about the orientation of the atomic lattice of the ferrite grains that surround the cementite. The results of both techniques were verified by optical serial sectioning of the same specimen. Development of a non-destructive imaging technique, sensitive enough to detect cementite microstructure, is needed in order to experimentally observe the nucleation and growth of the cementite. Kinetics of this process has not been studied in an in-situ experiment up to now. In Chapter 3 we have suggested a number of improvements to the experimental approach that would allow to study the formation and the evolution of cementite in-situ.

Algebraic phase retrieval   The experimental work described in Chapter 3 inspired us to investigate whether the image reconstruction techniques, that are used in the

field of X-ray PCI and X-ray PCT, can be improved. We distinguished improvements in terms of the accuracy of reconstruction and minimizing the amount of experimental data needed for reconstruction. State-of-the-art methods did not allow to obtain an accurate (quantitative) tomographic reconstruction of the specimen based on tomographic data acquired in x-ray phase-contrast mode. Instead, qualitative reconstructions were often computed by applying a standard tomographic reconstruction (i.e. filtered back-projection) to unprocessed phase-contrast data. Often, experimental conditions that yield a lower phase-contrast effect were used in order to reduce the artifacts that occur due to the fact that most of the phase retrieval models were intrinsically ill-posed. In Chapter 4 we propose a novel algebraic algorithm for phase retrieval. This algorithm is based on Total Variation (TV) minimization and can incorporate various phase retrieval models, such as TIE, CTF, Mixed TIE-CTF [51] or their variations based on the assumption of phase-attenuation duality [52, 53, 54] . Unlike the standard phase retrieval approach, which relies on L2 regularization, the algebraic phase retrieval based on TV minimization is capable to recover the frequency bands of the solution that are either undefined by the linear phase retrieval model or severely corrupted by noise. TV minimization is based on the assumption that the reconstructed image has a sparse gradient magnitude (i.e. it is piece-wise constant) and performs better when this condition is satisfied. However, the simulations showed that this method also improves the accuracy of phase retrieval when the retrieved phase image is not strictly piece-wise constant. It can also be seen that both the measurement errors (i.e. noise) and the systematic errors related to non-linearity of the phase-contrast effect, can be effectively suppressed using algebraic phase retrieval based on TV minimization. Results of reconstructions applied to experimental data confirm that algebraic phase retrieval can significantly outperform the standard phase retrival based on L2 regularization. In particular, these results demonstrate that, as long as the reconstructed image complies with the assumption of sparsity, the number of phase-contrast images acquired at different propagation distances to obtain artifact-free phase retrieval, can be decreased.

Algebraic Phase Tomography The main goal of the work described in Chapter 4 was to explore the applicability of algebraic reconstruction to phase retrieval. The results of this investigation encouraged us to continue this work and to develop an algebraic reconstruction algorithm for tomographic reconstruction based on phase contrast data. The algebraic approach allows to combine phase retrieval and to-

mographic reconstruction into a single linear inverse problem. We have assumed that by solving the problem of phase retrieval and tomographic reconstruction simultaneously, a more accurate solution can be achieved.Chapter 5 describs three variations of the algebraic reconstruction algorithm based on the TV minimization approach developed for X-ray PCT: the *full algebraic reconstruction*, the *algebraic tomographic reconstruction* and the *algebraic phase retrieval*. These algorithms are compared with each other and with the standard sequential approach based on filtered back-projection. The results show that under certain conditions, errors that normally originate from artifacts related to phase retrieval can be virtually eliminated. Naturally, the accuracy of reconstruction depends on how much the experimental conditions comply with the assumptions underlying the reconstruction algorithm. For instance, *algebraic tomographic reconstruction* yields poor accuracy for resolution limited data and *algebraic phase retrieval* fails for datasets with a small number of tomographic projections. In most of the reconstructions presented in Chapter 5, the *full algebraic reconstruction* approach outperforms both the other algebraic reconstruction techniques and the sequential reconstruction. Among all of the proposed reconstruction techniques, the *full algebraic reconstruction* is the most computationally intensive, requiring a large number of iterations to converge and more computations during each iteration. We believe that this work demonstrates the high potential of algebraic algorithms in applications where the experimental conditions restrict the number of tomographic projections or the number of phase-contrast images acquired per projection. It may also be the best choice when experimental conditions do not permit measurements with high signal-to-noise ratio.

In-situ study of austenite   The work that was started during our investigation of the cementite morphology (see Chapter 2), was continued with the *in-situ* experiments dedicated to imaging the microstructural changes that take place in steel during a solid-state phase transformation (see Chapter 6). Using X-ray PCT, we obtained the first reconstructions of the three-dimensional morphology of the grains of the product phase (austenite) growing in the parent phase (ferrite) during the ferrite-to-austenite phase transformation. A miniature furnace that was designed for this experiment which allowed to perform a full 360° tomographic acquisition with a minimal sample-to-detector distance of $\sim 10mm$ while the sample is heated up to a maximum temperature of $900°C$.

The X-ray PCT data was acquired while the temperature of the sample was slowly

increased from $860°C$ to $900°C$. This way we obtained a series of tomographic reconstructions of the austenite grains during the phase transformation. The tomographic data was obtained for a cylindrical specimen with a height of approximately 600 μm and the diameter of 300 μm. The spatial resolution of the data was approximately $1 \mu m^3$, while the temporal resolution was approximately 9 minutes. To obtain tomographic reconstruction of the austenite structure we applied the *algebraic phase retrieval* algorithm proposed in Chapter 5. Reconstructions of the austenite structure demonstrate a large number of planar interfaces between ferrite and austenite. Some of these interfaces remain immobile during the phase transformation. We have concluded that this property of the grain growth should be related to the specific orientation relationships between the lattices of ferrite and austenite. This hypothesis has to be investigated in future studies using information about the lattice orientations obtained using X-ray DCT or three-dimensional X-ray diffraction (3DXRD).

Recommendations

Advancement in algorithms for phase retrieval and tomogramic reconstruction should lead to a better accuracy of the tomographic reconstructions that can be obtained from the experimental data and easier and faster data acquisition protocols. One of the algebraic algorithms developed by us for tomographic reconstructions was applied to improve the quality of the reconstructed data in the experimental study dedicated to observations of the austenite grain growth during the phase transformation. We believe that a similar algebraic algorithm could be used in order to reconstruct the structure of the austentenite grains from a significantly smaller number of tomographic projections. This would allow to increase the time resolution of in-situ X-ray PCT proportionally to the reduction in the number of projections. In order to achieve this, an algebraic reconstruction algorithm should be developed for strongly attenuating specimens. We expect that this would require solving a non-linear inverse problem. However, the linear approach that is described in Chapter 4 and Chapter 5 provides insights to finding the solution for such a non-linear minimization problem.

The algebraic reconstruction techniques described in Chapter 5 yield very high accuracy for specimens that are composed of light elements. It is therefore most

valuable for studies dedicated to biological specimens. In cases when the structure of a typical specimen is sufficiently sparse, the *full algebraic reconstruction* approach permits a significant reduction of the number of tomographic projections and hence the dose delivered to the specimen. A large number of different versions of this method can be easily derived in order to allow the use of different phase-contrast models (for instance multi-distance CTF or TIE) or to permit reconstructions in different acquisition geometries (for instance fan or cone beam).

Concerning further development of experimental techniques for materials science investigations, there are a large number of improvements that can be made in order to expand the capabilities of the experimental approach described in Chapter 3 and Chapter 6. A significant increase in spatial resolution of the PCI system is absolutely crucial for studying the formation and evolution of cementite. Observing the early stages of cementite formation, when the typical size of a cementite particle stays in the range between tens and hundreds on nanometers, would be more valuable for materials science than the observations made at the later stages of cementite growth. Currently, the spatial resolution of < 200 nm can be achieved in magnified holotomography (i.e. propagation-based PCT) experiments at the ID22 (Micro-Fluorescence, Imaging and Diffraction) beamline of ESRF [128]. However, imaging at such a resolution may require small sample size (< 100 μm) and the grinding technique that was used to manufacture samples in the current project might not be suitable. Instead, an electrochemical etching could be used in order to manufacture specimens smaller than 100 μm. It should be also taken into account that the object-to-detector distance suitable for imaging with sub-micron resolution at low energies might significantly limit the maximum furnace size for the in-situ experiment.

Chapter 6 contains a detailed description of the improvements that are required to further improve in-situ investigations of the austenite grain growth. We stated there, that through the optimization of the experimental conditions at the ID11 beamline of ESRF, it is possible to perform a time-resolved tomographic acquisition of the austenite-ferrite phase transformation with a time resolution of about 1 to 2 minutes. Perhaps another order of magnitude improvement in time resolution is possible, given that the number of projections required for the accurate reconstruction can be reduced after implementing an algebraic reconstruction algorithm suitable for strongly attenuating specimens. An experimental approach based on X-ray PCT performed with high spatial and temporal resolution can find applications in a large variety of studies of processes related to solid-state phase transformations in metals.

Bibliography

[1] W. Coene, G. Janssen, M. Op de Beeck, and D. Van Dyck. "Phase retrieval through focus variation for ultra-resolution in field-emission transmission electron microscopy," Phys. Rev. Lett., **69,** 3743–3746 (1992).

[2] U. Bonse, and M. Hart, "An X-Ray Interferometer," Appl. Phys. Lett. **6** 155–156 (1965).

[3] F. Cosmi, A. Bernasconi, and N. Sodini, "Phase contrast micro-tomography and morphological analysis of a short carbon fibre reinforced polyamide," Compos. Sci. Technol. **71,** 23–30 (2011).

[4] O. Coindreau, C. Mulat, C. Germain, J. Lachaud, and G.L. Vignoles, "Benefits of X-ray CMT for the Modeling of C/C Composites," Adv. Eng. Mat. **13,** 178–185 (2011).

[5] M. Herbig, A. King, P. Reischig, H. Proudhon, E. M. Lauridsen, J. Marrow, J.-Y. Buffiere, W. Ludwig, "3-D growth of a short fatigue crack within a polycrystalline microstructure studied using combined diffraction and phase-contrast X-ray tomography," Acta Mater. **59,** 590–601 (2011).

[6] T.S. Argunova, M.Y. Gutkin, J.H. Je, E. N. Mokhov, S.S. Nagalyuk, and Y. Hwu, "SR phase-contrast imaging to address the evolution of defects during SiC growth," Phys. Status Solid. A Appl. Mat. **208,** 819–824 (2011).

[7] J. Xu., A. W. Stevenson, D. Gao, M. Tykocinski, D. Lawrence, S. W. Wilkins, G. M. Clark, E. Saunders, and R. S. Cowan, "The role of radiographic phase-contrast imaging in the development of intracochlear electrode arrays," Otology and Neurotology, **22,** 862–868 (2001).

[8] A. Momose, T. Takeda, and Y. Itai, "Blood vessels: Depiction at phase-contrast x-ray imaging without contrast agents in the mouse and rat – Feasibility study," Radiology **217,** 593–596 (2000).

[9] M. J. Kitchen, R. A. Lewis, N. Yagi, K. Uesugi, D. Paganin, S. B. Hooper, G. Adams, S. Jureczek, J. Singh, C. R. Christensen, A. P. Hufton, C. J. Hall, K. C. Cheung, and K. M. Pavlov, "Phase contrast X-ray imaging of mice and rabbit lungs: a comparative study," Br. J. Radiol., **78,** 1018-1027(2005).

[10] J. W. Kim, H. S. Seo, Y. Hwu, J. H. Je, A. Kim, C. W. Oh, S. Y. Suh, S. W. Rha, C. G. Park, and D. J. Oh, "In vivo real-time vessel imaging and ex vivo 3d reconstruction of atherosclerotic plaque in apolipoprotein e-knockout mice using synchrotron radiation microscopy," Int. J. Cardiology, **114** 166–171, (2007).

[11] J. Mollenhauer, M. E. Aurich, Z. Zhong, C. Muehleman, A. A. Cole, M. Hasnah, O. Oltulu, K. E. Kuettner, A. Margulis, and L. D. Chapman, "Diffraction-enhanced x-ray imaging of articular cartilage," Osteoarthritis and Cartilage, **10,** 163–171, (2002).

[12] X. Zhang, X.S. Liu, X.R. Yang, S.L. Chen, P.P. Zhu, and Q.X. Yuan. "Mouse blood vessel imaging by in-line X-ray phase-contrast imaging," Phys. Med. Bio., **53,** 5735–5743, (2008).

[13] P. Coan, F. Gruener, C. Glaser, T. Schneider, A. Bravin, M. Reiser, and D. Habs, "Phase contrast medical imaging with compact X-ray sources at the Munich-Centre for Advance Photonics," Nuclear Instruments and Methods in Physics Research A **608**, S44–S46 (2009).

[14] E.C. Ismail, W. Kaabara, D. Garritya, O. Gundogdua, O. Bunkb, F. Pfeifferb, M.J. Farquharsond, and D.A. Bradley, "X-ray phase contrast imaging of the bone-cartilage interface," Applied Radiation and Isotopes **68**, 767–771 (2010).

[15] Tao Q., Li D., Zhang L., Luo S., "Using X-ray In-Line Phase-Contrast Imaging for the Investigation of Nude Mouse Hepatic Tumors," PLoS ONE **7**, e39936, (2012).

[16] P. Weiss, L. Obadia, D. Magne, X. Bourges, C. Rau, T. Weitkamp, I. Khairoun, J.M. Bouler, D. Chappard, O. Gauthier, and G. Daculsi, "Synchrotron X-ray microtomography (on a micron scale) provides three dimensional imaging representation of bone ingrowth in calcium phosphate biomaterials," Biomaterials **24,,** 4591 (2003).

[17] A. A. Appel, J. C. Larson, S. Somo, Z. Zhong, P. P. Spicer, F. K. Kasper, A. B. Garson, A. M. Zysk, A. G. Mikos, M. A. Anastasio, and E. M. Brey, "Imaging

of Poly(α-hydroxy-ester) Scaffolds with X-ray Phase-Contrast Microcomputed Tomography," Tissue Eng. Part C, **18,** (2012).

[18] M.J. Berger, J.H. Hubbell, S.M. Seltzer, J. Chang, J.S. Coursey, R. Sukumar, and D.S. Zucker, "Xcom: Photon cross sections database," NIST Standard Reference Database, **8**, 87–3597 (1998).

[19] E. Hecht, *Optics (4th Edition).* Addison Wesley, 4 edition, 2001.

[20] B. L. Henke, E. M. Gullikson, and J. C. Davis. "X-ray interactions: Photoabsorption, scattering, transmission, and reflection at e = 50-30,000 ev, z = 1-92," Atomic Data and Nuclear Data Tables, **54,** 181 – 342, (1993).

[21] J. Als-Nielsen, D. McMorrow, *Elements of Modern X-ray Physics*, John Wiley and Sons Ltd, 2001.

[22] A. Momose, T. Takeda, Y. Itai, A. Yoneyama, and K. Hirano. "Phase-contrast tomographic imaging using an x-ray interferometer," J. of Synchrotron Rad., **5,** 309–314 (1998).

[23] D. Chapman, W. Thomlinson, R. E. Johnston, D. Washburn, E. Pisano, N. Gmür, Z. Zhong, R. Menk, F. Arfelli, and D. Sayers. "Diffraction enhanced X-ray imaging," Phys. in Medic. and Biol., **42,** 2015–2025, (1997).

[24] C. David, B. Nöhammer, H. H. Solak, and E. Ziegler, "Differential X-ray phase contrast imaging using a shearing interferometer. *Applied Physics Letters*, **21** 3287–3289, (2002).

[25] Alessandro Olivo and Robert Speller. "A coded-aperture technique allowing X-ray phase contrast imaging with conventional sources," Applied Phys. Lett., 91, (2007).

[26] A. Snigirev, I. Snigireva, V. Kohn, S. Kuznetsov, and I. Schelokov, "On the possibilities of X-ray phase contrast microimaging by coherent highenergy synchrotron radiation," Rev. Sci. Instr., **66,** 5486, (1995).

[27] A. Momose, T. Takeda, A. Yoneyama, I. Koyama, Y. Itai, "Wide-area phase-contrast X-ray imaging using large X-ray interferometers," Nucl. Instr. and Methods in Phys. Research Sec. A: Accelerators, Spectrometers, Detectors and Associated Equipment, 467–468, (2001).

[28] M. N. Wernick, O. Wirjadi, D. Chapman, Z. Zhong, N. P. Galatsanos, Y. Yang, J. G. Brankov, O. Oltulu, "Multiple-image radiography," Phys. Medic. and Biol. **48** 3875–3895 (2003).

[29] E. Pagot, P. Cloetens, S. Fiedler, A. Bravin, P. Coan, J. Baruchel, J. Härtwig, W. Thomlinson, "A method to extract quantitative information in analyzer-based x-ray phase contrast imaging," Appl. Phys. Lett. **82** 3421–3423, (2001).

[30] T. Weitkamp, A. Diaz, and C. David, "X-ray phase imaging with a grating interferometer," Opt. Expr., **13**, 6296–6304 (2005).

[31] M. Bech, O. Bunk, T. Donath, R. Feidenhans'l, C. David, F. Pfeiffer, "Quantitative x-ray dark-field computed tomography," Phys. in Med. and Biol. **55,** 5529–5539 (2010).

[32] F. Pfeiffer, T. Weitkamp, O. Bunk, and C. David, "Phase retrieval and differential phase-contrast imaging with low-brilliance x-ray sources," Nature Physics, **2,** 258, (2006).

[33] K. Ignatyev, P. R. T. Munro, D. Chana, R. D. Speller, and A. Olivo "Coded apertures allow high-energy x-ray phase contrast imaging with laboratory sources," J. Appl. Phys. **110**, 014906 (2011).

[34] P. Munro, L. Rigon, K. Ignatyev, F. Lopez, D. Dreossi, R. Speller, and A. Olivo, "A quantitative, non-interferometric X-ray phase contrast imaging technique," Opt. Express 21, 647-661 (2013).

[35] A. V. Bronnikov, "Theory of quantitative phase-contrast computed tomography," J. Opt. Soc. Am. **19,** 472–480 (2002).

[36] Bech M, Jensen T.H, Feidenhans'l R, Bunk O, David C and Pfeiffer F. "Soft-Tissue Phase-Contrast Tomography with X-Ray Tube Sources," Physics in Medicine and Biology **54**, 2747–2753 (2009).

[37] P Bartl, F Bayer, J Durst, W Haas, T Michel, A Ritter, T Weber and G Anton, "Grating-based high energy X-ray interferometry with the Medipix-detector in simulation and measurement," JINST **5**, P10008 (2010).

[38] "Novel Microfocus X-ray Sources for High-Pressure Crystallography", `http://www.incoatec.de/fileadmin/downloads/Poster/IDO-P22-010A-xs.pdf`.

[39] O. Hemberg, "Liquid-metal-jet anode electron-impact x-ray source," Applied Physics Lett., **83** 1483–1485 (2003).

[40] M. Bech, O. Bunk, C. David, R. Ruth, R. Loewen, J. Rifkin, R. Feidenhansl, and F. Pfeiffer, "Hard x-ray phase-contrast imaging with the compact light source based on inverse compton x-rays," J. Synchr. Rad., **16**, 43–47, (2008).

[41] D. Hasegawa, H. Yamada, Andrey I. Kleev, Norio Toyosugi, Taichi Hayashi, Takanori Yamada, Isao Tohyama, and Young-Deok Ro, "The portable synchrotron MIRRORCLE-6X," AIP **716**, 116–119, (2004).

[42] D. Hasegawa, H. Yamada, A.I. Kleev, N. Toyosugi, T. Hayashi, I. Tohyama, and Y. D. Ro, "The tabletop synchrotron Mirrorcle-6X," Proc. 14th Sympo. Accelerator Science and Technology, (2003).

[43] Michael D. Uchic, "Serial Sectioning Methods for Generating 3D Characterization Data of Grain- and Precipitate-Scale Microstructures," Comput. Methods for Microstructure-Property Relationships, 31–52 (2011.)

[44] T. Maitland and S. Sitzman, "Electron Backscatter Diffraction (EBSD) Technique and Materials Characterization Examples," Scanning Microsc. for Nanotech., 41–75 (2007).

[45] W. Ludwig, P. Reischig, A. King, M. Herbig, E. M. Lauridsen, G. Johnson, T. J. Marrow, and J. Y. Buffère, "Three-dimensional grain mapping by x-ray diffraction contrast tomography and the use of Friedel pairs in diffraction data analysis," Rev. Sci. Instrum. **80**, 033905 (2009).

[46] S. Offerman, N. v. Dijk, J. Sietsma, S. Grigull, E. Lauridsen, L. Margulies, H. Poulsen, M. Rekveldt, and S. v. d. Zwaag, "Grain nucleation and growth during phase transformations," Science, **298**, 1003–1005 (2002).

[47] P. Cloetens, W. Ludwig, J. Baruchel, D. V. Dyck, J. V. Landuyt, J. P. Guigay and M. Schlenker, "Holotomography:quantitative phase tomography with micrometer resolution using hard synchrotron radiation x-rays," Appl. Phys. Lett., **75**, 2912–2914 (1999).

[48] K. A. Nugent, T. E. Gureyev, D. F. Cookson, D. Paganin, and Z. Barnea, "Quantitative Phase Imaging Using Hard X Rays," Nature **77,** 2961–2964 (1996).

[49] X. Wu, H. Liu, "A general theoretical formalism for X-ray phase contrast imaging," J. of X-ray Sci. and Techn. **11**, 33–42 (2003).

[50] J.-P. Guigay, M. Langer, R. Boistel, and P. Cloetens, "A mixed contrast transfer and transport of intensity approach for phase retrieval in the Fresnel region," Opt. Lett. **32**, 1617–1619 (2007).

[51] M. Langer, F. Peyrin, P. Cloetens and J.-P. Guigay , "Quantitative comparison

of direct phase retrieval algorithms in in-line phase tomography," Med. Phys. **35**, 4556 (2008).

[52] D. Paganin, S. Mayo, T. Gureyev, P. Miller, and S. Wilkins, "Simultaneous phase and amplitude extraction from a single defocused image of a homogeneous object," J. Microsc., **206**, 33 – 40 (2002).

[53] L.D. Turner, B.B. Dhal, J.P. Hayes et al., "X-ray phase imaging: Demonstration of extended conditions with homogeneous objects," Opt. Expr. **12,** 2960–2965 (2004).

[54] X. Wu, A. Yan, "Phase retrieval from one single phase contrast X-ray image," Opt. Expr. **17,** 11187 (2009).

[55] M. Langer, P. Cloetens, and F. Peyrin, "Fourier-wavelet regularization of phase retrieval in X-ray in-line phase tomography," JOSA A **26**, 1876-1881 (2009).

[56] Hofmann, R.; Moosmann, J.; Baumbach, T., "Criticality in single-distance phase retrieval," Opt. Expr. **19,** 25881–25890 (2011).

[57] Huaiqun Guan and Richard Gordon, "Computed tomography using algebraic reconstruction techniques (ARTs) with different projection access schemes: a comparison study under practical situations," 1996 Phys. Med. Biol. **41** 1727.

[58] L.I. Rudin, S. Osher, E. Fatemi, "Nonlinear total variation based noise removal algorithms," Physica D, **60**, 259–268 (1992).

[59] "Iterative algorithms for deblurring and deconvolution with constraints," Inv. Probl., **14** 1455–1467 (1998).

[60] F. Natterer, *The Mathematics of Computerized Tomography* (New York: Wiley, 1986).

[61] A. Chambolle, "An algorithm for total variation minimization and applications," J. Math. Imaging Vision **20**, 89-97 (2004).

[62] Emil Y. Sidky, Mark A. Anastasio, and Xiaochuan Pan, "Image reconstruction exploiting object sparsity in boundary-enhanced X-ray phase-contrast tomography," Opt. Expr. **18,** 10404 (2010).

[63] J. Dahl, P. C. Hansen, S. H. Jensen, and T. L. Jensen, "Algorithms and Software for Total Variation Image Reconstruction via First-Order Methods, Numerical Algorithms," **53**, 67-92 (2010).

[64] A. W. M. van Eekeren, K. Schutte and L. J. van Vliet, "Multiframe Super-Resolution Reconstruction of Small Moving Objects," IEEE Trans. Im. Proc. **19**, 2901-2912 (2010).

[65] E. Candes, J. Romberg, and T. Tao, "Robust uncertainty principles: Exact signal reconstruction from highly incomplete frequency information," IEEE Trans. Inform. Theory, **52,** 489–509 (2006).

[66] J. van Heekeren, A. Kostenko, T. Hanashima, H. Yamada, S. Stallinga, S. E. Offerman and L. J. van Vliet, "Characterization of an x-ray phase contrast imaging system based on the miniature synchrotron MIRRORCLE-6X," Medical Physics **38,** 5136–5145 (2011).

[67] F. Zernike, "Phase-contrast, a new method for microscopic observation of transparent objects," Physica, **9**, 686–698, 974–986, (1942).

[68] S. W. Wilkins, T. E. Gureyev, D. Gao, A. Pogany, and A. W. Stevenson, "Phase-contrast imaging using polychromatic hard X-rays," Nature, **384** 335–338 (1996).

[69] E. D. Pisano, R. E. Johnston, D. Chapman, et al., "Human breast cancer specimens: Diffraction-enhanced Imaging with histologic Correlation-improved conspicuity of lesion detail compared with digital radiog- raphy," Radiology **214**, 895–901 (2000).

[70] F. Arfelli, V. Bonvicini, A. Bravin, et al. , "Mammography with synchrotron radiation: Phase-detection techniques," Radiology **215**, 286–293 (2000).

[71] R. A. Lewis, "Medical phase contrast X-ray imaging: current status and future prospects," Phys. in Med. and Biol., **49**, 3573–3583 (2004).

[72] J. Li, Z. Zhong, D. Connor, J. Mollenhauer, and C. Muehleman, "Phase-sensitive x-ray imaging of synovial joints," Osteoarthritis and Cartilage, **17**, 1193–1196, (2009).

[73] A. Momose, T. Takeda, and Y. Itai, "Blood vessels: Depiction at phase-contrast x-ray imaging without contrast agents in the mouse and rat–feasibility study," Radiology, **217**, 593, (2000).

[74] P. Cloetens, R. Barrett, J. Baruchel, J.-P. Guigay, and M. Schlenker, "Phase objects in synchrotron radiation hard x-ray imaging," J. of Phys. D: Applied Physics, **29**, 133–146, (1996).

[75] T. Tuohimaa, M. Otendal, and H. M. Hertz, "Phase-contrast X-ray imaging with a liquid-metal-jet-anode microfocus source," Applied Physics Letters, **91** (2007).

[76] R. Kincaid, A. Krol, S. Fourmaux, J.C. Kieffer, C. Serbanescu, M. Servol, L. Vogelsang, S. Wilkins, A. Stevenson, Y. Nesterets, E. Lipson, H. Ye, A. Pogany, "Development of ultrafast laser-based X-ray in-vivo phase-contrast micro-ct beamline for biomedical applications at advanced laser light source (alls)," Proc. Soc. Photo Opt. Instrum. Eng., **7078**, 707818.1–707818.12, (2008).

[77] H. Yamada. "Novel x-ray source based on a tabletop synchrotron and its unique features," Nucl. Instr. and Meth. in Phys. Research B, **199**, 509–516, (2003).

[78] H. Toru, Y. Hironari, S. Makoto, H. Daisuke, M. Masaki, O. Yasuhito, T. Jyunya, H. Takayasu, N. Norihisa, and T. Masashi, "Refraction contrast 11×-magnified x-ray imaging of large objects by mirrorcle-type table-top synchrotron," J. of Synchr. Rad., **13**, 397–402 (2006).

[79] H. Yamada, T. Hirai, M. Morita, T. Hanashima, M. Sasaki, D. Hasegawa, T. Hayashi, T. Yamada, , and H. Saisho, "Portable synchrotron hard x-ray source mirrorcle-6x for x-ray imaging," Proc. 8th Int. Conf. X-ray Microscopy, IPAP Conf. Series 7, 130–132 (2005).

[80] U. Shmueli and A. J. Cochran Wilson, "International tables for crystallography,"Springer, **3**, 637–639 (2004).

[81] M. Thoms, S. Bauchau, D. Hausermann, M. Kunz, T. Le Bihan, and M. Mezouar, "An improved x-ray detector for use at synchrotrons," Nucl. Instr. and Meth. in Phys. Research A, **413**, 175–184 (1998).

[82] P. Witt, "Detective quantum efficiency of storage phosphors for soft X-rays," Pure Applied Optics, **2**, 61–70 (1993).

[83] M. Thoms, "The quantum efficiency of with image radiographic imaging plates," Nucl. Instr. and Meth. in Physics Research A, **378**, 598–611 (1996).

[84] J. C. Dainty and R. Shaw, "Image science: principles, analysis and evaluation of photographic-type imaging processes," London: Academic Press (1974).

[85] M. Vulovic, B. Rieger, L.J. van Vliet, A.J. Koster, and R.B.G. Ravelli, "A toolkit for the characterization of ccd cameras for transmission electron micrsocopy," Acta Crystallographica Section D: Biological Crystallography, **D66**, 97–109, (2010).

[86] E. F. Donnelly, K. G. Lewis, K. M. Wolske, D. R. Pickens, and R. R. Price, "Characterization of the phase-contrast radiography edge-enhancement effect in a cabinet X-ray system," Physical in Medicine and Biology, **51**, 21–30 (2006).

[87] X. Z. Wu and H. Liu., "Clarification of aspects in in-line phase-sensitive X-ray imaging," Medical Physics, **34**, 737–743, (2007).

[88] X. Wu and H. Liu. "An experimental method of determining relative phase-contrast factor for x-ray imaging systems," Med. Phys., **31**, 997–1002, (2004).

[89] J.W. Goodman, "Introduction to Fourier optics," Roberts & Company Publishers, (2005).

[90] D.M. Paganin, "Coherent X-Ray Optics," Oxford University Press, USA (2006).

[91] S. Agostinelli, J. Allison, K. Amako, J. Apostolakis, H. Araujo, P. Arce, M. Asai, D. Axen, S. Banerjee, G. Barrand, et al, "Geant4: a simulation toolkit," Nuclear Inst. and Methods in Physics Research and A, **506**, 250–303 (2003).

[92] J. Beutel, H. L. Kundel, R. L. Van Metter, M. Sonka, M. Fitzpatrick, Y. Kim, and S. C. Horii, "Handbook of Medical Imaging: Display and PACS," Handbook of Medical Imaging, SPIE Press, **3**, (2000).

[93] J. H. Hubbell and S. M. Seltzer, "Nistir 5632, tables of x-ray mass attenuation coefficients and mass energy-absorption coefficients," Technical report, National Institute of Standards and Technology.

[94] B. Golosio, P. Delogu, I. Zanette, P. Oliva, A. Stefanini, G. Stegel, and M. Carpinelli, "Visibility of tumor- like details in inline phase contrast mammography using quasimonochromatic X-ray sources," Nuclear Instruments and Methods in Physics Research A 608, S66–S69 (2009).

[95] N. Wiener, "The Extrapolation, Interpolation and Smoothing of Stationary Time Series," New York, Wiley (1949).

[96] Y. I. Nesterets and S. W. Wilkins, "A flexible configuration for a high-energy phase-contrast imaging beamline involving in-line focusing crystal optics," Radiation Physics and Chemistry, **75**, 1981–1985 (2006).

[97] A. Kostenko, H. Sharmaa, E.G. Dere, A. King, W. Ludwig, W. van Oel, S. Stallinga, L.J. van Vliet, S. E. Offerman, "Three-dimensional morphology of cementite in steel studied by x-ray phase-contrast tomography," Scr. Mat., **67**, 261–264 (2012).

[98] H.K.D. Bhadeshia, "Steels for Bearings," Prog. Mater. Sci., **57**, 268–435 (2012).

[99] Yuan-Tsung Wang, Yoshitaka Adachi, Kiyomi Nakajima and, Yoshimasa Sugimoto, "Quantitative three-dimensional characterization of pearlite spheroidization," Acta Materialia **58**, 4849–4858 (2010).

[100] N.V. Luzginova, L. Zhao, J. Sietsma, "The Cementite Spheroidization Process in High-Carbon Steels with Different Chromium Contents," J. **513**, A39A (2008).

[101] C.-Y Hung, G Spanos, R.O Rosenberg, M.V Kral, "Three-dimensional observations of proeutectoid cementite precipitates at short isothermal transformation times," J. **50**, 3781–3788 (2002).

[102] M.V. Kral, G. Spanos, "Three-dimensional analysis of proeutectoid cementite precipitates," J. **47**, 711-724 (1999).

[103] M.V. Kral, M.A. Mangan, G. Spanos, R.O. Rosenberg, "Three-dimensional analysis of microstructures ," Mater. Char. **45**, 17–23 (2000).

[104] T.E. Gureyev, Y.I. Nesteretsa, D.M. Paganin, A. Pogany, S.W. Wilkins, "Linear algorithms for phase retrieval in the Fresnel region. 2. Partially coherent illumination," Opt. Commun. **259**, 569–580 (2006).

[105] A. Kostenko, H. Sharma, E.G. Dere, A. King, W. Ludwig, W. van Oel, S.E. Offerman, S. Stallinga, and L.J. van Vliet , "In-line x-ray phase-contrast tomography and diffraction-contrast tomography study of the ferrite-cementite microstructure in steel ," AIP Conf. Proc. **63**, 1437 (2012).

[106] A. Kostenko, K. Batenburg, A. King, S. Offerman and L. J. van Vliet, "Phase retrieval in in-line x-ray phase contrast imaging based on total variation minimization," Opt. Expr., **21,** 710–723 (2013).

[107] T.E. Gureyev, T.J. Davis, A. Pogany, S.C. Mayo, and S.W. Wilkins, "Optical phase retrieval by use of first Born-and Rytov-type approximations," Appl. Opt., **43,** 2418–2430 (2004).

[108] X. Bresson and T. F. Chan, "Fast dual minimization of the vectorial total variation norm and applications to color image processing," Inverse Problems and Imaging, **2,** 455–484 (2008)

[109] A. Beck, M. Teboulle, "A Fast Iterative Shrinkage-Thresholding Algorithm for Linear Inverse Problems," SIAM Journal on Imaging Sciences **2**, 183-202 (2009).

[110] A. Beck, M. Teboulle, "Fast Gradient-Based Algorithms for Constrained Total Variation Image Denoising and Deblurring Problems," IEEE Transactions on Image Processing, **18**, 2419–2434 (2009).

[111] T.Q. Pham, L.J. van Vliet, K. Schutte, "Robust Super-Resolution by minimizing a Gaussian-weighted L2 error norm," J. Phys.: Conf. **124**, 012037 (2008).

[112] R. Barrett, R. Baker, P. Cloetens, Y. Dabin, C. Morawe, H. Suhonen, R. Tucoulou, A. Vivo, and L. Zhang. "Dynamically-figured mirror system for high-energy nanofocusing at the ESRF," Proc. SPIE **12**, 813904 (2011).

[113] R. Mokso, P. Cloetens, E. Maire, W. Ludwig, and J.-Y. Buffire, "Nanoscale zoom tomography with hard x-rays using Kirkpatrick-Baez optics," Appl. Phys. Lett. **90**, 144104 (2007).

[114] Chen, R.C.; Rigon, L.; Longo, R., "Quantitative 3D refractive index decrement reconstruction using single-distance phase-contrast tomography data," J. Phys. D Appl. Phys. **44**, 9 (2011).

[115] M. Vetterli, P. Marziliano, and T. Blu, "Sampling signals with finite rate of innovation," IEEE Trans. Signal Proc.**50**, 1417–1428 (2003).

[116] A. C. Kak, and M. Slaney, *Principles of computerized tomographic imaging* (IEEE Press, 1988).

[117] L. Armijo, "Minimization of functions having Lipschitz continuous first partial derivatives," Pacific J. of Math. **16**, 1–3 (1966).

[118] G. M. P. van Kemplen, and L. J. van Vliet, "The influence of the regularization parameter and the first estimate on the performance of Tikhonov regularized non-linear image restoration algorithms," J. of Microscopy **198**, 63–75 (2000).

[119] S.-R. Zhao, and H. Halling, "A new Fourier method for fan beam reconstruction," IEEE Nucl. Sci. Symp. Med. and Imaging Conf. **2**, 1287–1291 (1995).

[120] G.-H. Chen, S. Leng, and C. A. Mistretta, "A novel extension of the parallel-beam projection-slice theorem to divergent fan-beam and cone-beam projections," Med. Phys. **32**, 654–665 (2005).

[121] G. R. Purdy, J. Agren, A. Borgenstam, Y. Brechet, M. Enomoto, T. Furuhara, E. Gamsjager, M. Goune, M. Hillert, C. Hutchinson, M. Militzer, and H. Zurob, "ALEMI: A ten year history of discussions of alloying-element interactions with migrating interfaces," Met. Mater. Trans. A, **42A**, 3703–3718 (2011).

[122] S. Schmidt, S. F. Nielsen, C. Gundlach, L. Margulies, X. Huang, and D. J. Jensen, "Watching the Growth of Bulk Grains During Recrystallization of Deformed Metals," Science, **305**, 229–232 (2004).

[123] H. Sharma, *In-situ characterization of grain nucleation and coarsening in metallic microstructures using synchrotron radiation* , PhD Thesis (2012).

[124] M. Militzer, M.G. Mecozzi, J. Sietsma, and S. van der Zwaag, "Three-dimensional phase field modelling of the austenite-to-ferrite transformation," Acta Mater. , **54**, 3961–3972 (2006).

[125] G. Gottstein, and L.S. Shvindlerman, *Grain boundary migration in metals*, CRC Press (2010).

[126] A. Kostenko, K. Batenburg, A. King, S. Offerman and L. J. van Vliet, "Total variation minimization approach in propagation-based x-ray phase-contrast tomography," Opt. Expr., *in press* (2013).

[127] D.B. Lee, J.H Ko, and S.C Kwon, "High temperature oxidation of Ni-W coatings electroplated on steel," Mater. Sci. Eng.: A, **360**, 73–78 (2004).

[128] G. Requena, P. Cloetens, W. Altendorfer, C. Poletti, D. Tolnai, F. Warchomicka and H. P. Degischer, Scripta Materialia **61**, 760–763 (2009).

Summary

Phase-Contrast Tomography (PCT) is becoming an important technique for non-destructive, in-situ characterization of soft and hard condensed matter. This thesis sheds light on our progress in developing novel tomographic reconstruction algorithms in combination with in-situ experimental approaches that employ propagation-based PCT. These developments are aimed to improve the spatial and temporal resolutions of *in-situ* studies of the soft and hard condensed matter.

The mechanical properties of materials such as steel are, to a large extent, defined by its microstructure. Propagation-based PCT (i.e. holotomography) can be used to visualize the microstructures associated with small variations in density or composition in the bulk of the specimen. This imaging technique has the advantage of being non-destructive and allows to carry out *in-situ*, time-resolved observations of miscrostructural changes during dynamic processes such as solid-state phase transformations. Sufficient spatial and temporal resolution can be achieved only when an extremely bright x-ray source is used. In order to test whether a novel table-top x-ray source, the MIRRORCLE-6X, can be used for implementation of a propagation-based PCT system, we have carried out a series of experiments. The characteristics of a propagation-based PCI system that employs the MIRRORCLE-6X were analyzed and reported in [66].

In our further research we have focused on the experiments that could be performed at the European Synchrotron Radiation Facility (ESRF) in Grenoble, France. We reported on the investigation of the cementite microstructure in carbon steel [97]. In this work we present the reconstruction of the three-dimensional morphology of cementite grains in the bulk of steel using a non-destructive imaging technique – x-ray Phase-Contrast Tomography (PCT). Complementary information about the crystalline structure of the ferrite grains surrounding the cementite is obtained using x-ray Diffraction-Contrast Tomography (DCT) [105]. The work was continued by a time-resolved x-ray PCT investigation of the austenite grain growth during the

ferrite-to-austenite phase transformation in low-carbon steel. Experimental data allows to visualize the evolution of the three-dimensional morphology of the austenite-ferrite interfaces with a spatial resolution on the order of 1 μm and a time resolution of less than 9 minutes. The *in-situ* measurements show that the theory for grain growth during diffusional solid-state phase transformations needs to be extended in order to describe the drastically lower mobility that we observed for flat interfaces compared to curved interfaces. We observe that some flat interfaces are completely immobile, which is not predicted by the state-of-the-art theories and showed - for the first time - that new computational model for grain growth are needed.

Quantitative image reconstruction based on PCT data requires solving two inverse problems: phase retrieval and tomographic reconstruction. In most cases, the problem of phase retrieval is ill-posed and requires that some type of a prior knowledge about the reconstructed image (i.e. particular regularization method) is used. We present a novel algebraic approach suitable for phase retrieval using various linear models (published in [106]). In this approach Total Variation (TV) minimization is used for regularization of the linearized inverse problem by promoting the solution with a sparse gradient magnitude (i.e. piece-wise constant solution). In that case *prior* knowledge about the reconstructed image may allow to (partially) recover the unknown spatial frequencies that are undefined by the experimental data. The problem of tomographic reconstruction based on PCT data can be solved using a similar approach. We conclude our investigation of the image reconstruction algorithms by introducing several algebraic approaches suitable for tomographic reconstruction based on PCT data (published in [126]). In these approaches TV minimization is used to find a regularized solution to an underdetermined linear system based on a linearized representation of the PCT. When the density of the reconstructed object is piece-wise constant (or close to it) a virtually artifact-free solution can be computed for the tomographic problem. The proposed approach can also be used to radically improve the accuracy of the tomographic reconstruction based on incomplete data (e.g. small number of projections) or data with low signal to noise ratio.